AN ABSTRACT OF THE DISSERTATION OF

Fei Teng for the degree of Doctor of Philosophy in Materials Science presented on December 7, 2018.

Title: Investigation of Thermal Degradation in Structural Alloys for Nuclear Power Systems.

Abstract approved:

_____

Julie D. Tucker

The thermal degradation of structural materials is considered to be a key factor for evaluating the lifetime of current nuclear power plants. Ni-based and Fe-based alloys, such as 690, 625, 304, and 316, are widely used in nuclear industry as structural components due to the extraordinary corrosion resistance and mechanical properties in radioactive environment. In this research, the thermal degradation of Ni-Cr model alloys and additively manufactured AISI 316L stainless steel were investigated by microstructural characterization including X-ray diffraction, transmission electron microscopy, and micro-mechanical testing including nanoindentation and in situ micro compression testing. Results show a significant change in deformation behavior due to either thermally-induced precipitation or dual-phase structures. Precipitation and dual-phase structure induced-twinning deformation occurs in both isothermally aged Ni-Cr model alloys and printed 316L stainless steel instead of slipping.

Investigation of Thermal Degradation in Structural Alloys for Nuclear Power Systems

by
Fei Teng

A DISSERTATION

submitted to

Oregon State University

in partial fulfillment of
the requirements for the
degree of

Doctor of Philosophy

Presented December 7, 2018
Commencement June 2019

Doctor of Philosophy dissertation of Fei Teng presented on December 7, 2018.

APPROVED:

Major Professor, representing Materials Science

Head of the School of Mechanical, Industrial, and Manufacturing Engineering

Dean of the Graduate School

I understand that my dissertation will become part of the permanent collection of Oregon State University libraries. My signature below authorizes release of my dissertation to any reader upon request.

Fei Teng, Author

ACKNOWLEDGEMENTS

As the first graduate student mentored by Dr. Julie Tucker, I firstly would like to express sincere appreciation to my Ph.D. advisor Dr. Julie Tucker for guiding me from a fresh graduate student to a Ph.D. The great support on my career life extension from Dr. Tucker opens my vision and extends my network in the nuclear field. I failed lots of times on research exploring during Ph.D., but the author will always find the right way to go as the encouragement from Dr. Tucker was always by my side. I still remembers what Dr. Tucker taught me in the first group meeting of the author's research life: positive emotion is always much more powerful than negative emotion. Encouraging is more useful than pushing. The author will keep this in mind and pass the spirit to more people.

Then I wants to acknowledge Dr. Cheng Sun, who gave me the chance to know more and learn more in Idaho National Laboratory. His wisdom and patience lead me to higher steps on TEM skill and scientific thought. I would like to thank Dr. Peter Hosemann and Mr. Hi Vo in UC Berkeley as well. It is impossible for me to reach such a level on micro-mechanical properties without the mentoring of Dr. Peter Hosemann and the help of Mr. Hi Vo on in situ micro compression testing and the scientific analysis on data analysis.

I also wishes to thank colleagues in Nuclear Material and Metallurgy group at the Oregon State University. The friendly working and studying environment that the whole group obtains strongly support on my research.

Finally, I would give sincere appreciation to my parents, Kai Teng and Fengmei Liu. Your firm support and endless love make me pass through all difficulty in the five

years. I am not able to stand here as a Ph.D. without your encouragement. Your words were on my side every school day and took me through every lonely library night in those years. I love you forever and I will always be with you, mom and dad.

CONTRIBUTION OF AUTHORS

In Chapter 2: Effect of Stoichiometry on the Evolution of Long Range Ordering in Ni_xCr Alloys, Dr. David Sprouster and Dr. Lynne Ecker performed the synchrotron X-ray diffraction experiment and corresponding data analysis. Dr. David Sprouster also assisted in the writing of experimental detail section. Dr. Jia-Hong Ke assisted in paper reviewing and data interpretation of the manuscript. In Chapter 3: Investigation of Hardening Effect of Ni_2Cr Long Range Ordering Domain as Function of Grain Orientation by In Situ Micropillar Compression Testing, Mr. Hi Vo assisted in micro compression testing and Dr. Peter Hosemann assisted on the research and data analysis. In Chapter 4: Investigation of Role of Heterogenous Substructure on the Failure Behavior of Additive Manufactured 316L Stainless Steel by in Situ Micro Compression Testing, Dr. Robert C. O'Brien assisted on sample fabrication of AM316L. Dr. Michael D. McMurtrey performed part of the EDS and X-ray CT characterization of AM316L. Mr. Ching-Heng Shiau assisted in the electro-polishing of the specimen. Chapter 4 of this research is under the mentoring of Dr. Cheng Sun.

TABLE OF CONTENTS

Page

TABLE OF CONTENTS (Continued)

Page

TABLE OF CONTENTS (Continued)

Page

TABLE OF CONTENTS (Continued)

Page

LIST OF FIGURES

Figure Page

LIST OF FIGURES (Continued)

Figure Page

LIST OF FIGURES (Continued)

Figure Page

LIST OF FIGURES (Continued)

Figure Page

LIST OF TABLES

To my parents

滕凯　刘凤梅

1 Chapter 1: General Introduction

Nuclear power has been utilized worldwide over the past 40 years as a reliable source of economical and clean electrical energy [1]. Nuclear utilities produced 2477 TWh of electricity in 2016 [2]. As reported by the World Nuclear Association World Nuclear Performance Report 2018 [3], 11% of the world's electricity is provided by nuclear energy from 450 power reactors, about 60 more reactors are under construction, and an additional 150-160 are planned to be built. As shown in the World Energy Outlook 2017, 66% of global greenhouse gas emission was generated from the burning of fossil fuels in 2015 [4]. Nuclear energy has been considered an important resource for controlling greenhouse gases and the corresponding climate change due to its very low carbon emission [5]. Types of power reactors generally include: light water reactors (LWR), pressurized water reactors (PWR) and boiling water reactors (BWR), gas-cooled reactors, heavy-water reactors, and liquid-metal-cooled reactor [6]. Light water reactors are the predominant reactor type that is used world-wide, which includes PWR and BWR [7]. PWR are the most common power generation reactor used in United States among all types [8]. The designed lifetime of nuclear power plants is often 40 years and the average age of currently operating reactors is greater than 20 years. The United States is implementing plant license extensions for an additional 20 years beyond the original license, which is 40 years in the USA [9]. Research on materials degradation is one of the most important topics in nuclear plant license extension due to the cost and difficulty associated with replacing core components and peripheral systems.

The materials degradation challenges in current LWR can be grouped into three materials categories: fuel system, reactor pressure vessels (RPV), and structural materials [10]. Research on the fuel system focuses on the degradation from normal operation status to high burn-up situations. For RPV, the two primary issues are radiation-induced embrittlement and stress corrosion cracking (SCC) [10]. For structural materials, irradiation/thermal induced embrittlement is also a significant concern in LWR as the temperature range of the coolant is usually between 275 and 325 °C [11]. For example, proton irradiated 316L stainless steel and Ni-based alloy 690 have been observed to have significant intergranular cracking compared to unirradiated materials [12]. Over the long service life of reactor structural materials, thermally activated diffusion can cause significant degradation. This diffusion is further enhanced by the presence of irradiation induced damage [13]. The work in this thesis is focused on degradation mechanisms in structural alloys in face-centered cubic system, including both Fe-based stainless steels (e.g. 316, 316L, 304) and Ni-based alloys (e.g. 690, 625).

To address the role of thermal and irradiation induced degradation on mechanical properties, micro-scale mechanical testing was developed on nuclear materials. Micro-scale testing is an emerging technique to study degradation in materials for nuclear systems [14]. Micro-scale testing offers several advantages in terms of lowering dose to researchers when characterizing irradiated samples and increasing the number of samples in reactor exposures. Additionally, conventional engineering scale mechanical tests are usually limited by sample dimension and research purpose. For example, ion-beam irradiation has been widely used in the research of irradiation damage. However,

the penetration of ion-beam irradiated sample is usually very shallow and insufficient for full scale mechanical testing [15]. Another example where micro-mechanical has advantages over conventional scale testing is the research on effect of single crystal properties in polycrystalline alloys. The conventional test method is to induce deformation by engineering scale mechanical testing and perform microstructure characterization from the specimen that comes near broken area [16]. The relationship between stress and grain orientation is usually addressed by post analysis. With conventional mechanical testing, it is also difficult to measure the effect of load orientation on grains on deformation behavior [17]. To fill this gap in micromechanical testing, nanoindentation has been developed and widely utilized in the research of nuclear materials [14, 18] and properties of single crystals [19]. Nanoindentation is able to perform mechanical testing from several hundred nanometers [18] to several microns [20].

In this work, investigations on Ni-based alloys and newly developed austenitic additive-manufactured AISI 316L (AM316L) stainless steel were performed by both microstructure characterization and mechanical testing. Both alloys are FCC-based systems and widely used in core components of LWR. In this dissertation, three objectives are addressed: 1) Discover the role of stoichiometry on the thermal degradation of Ni-Cr model alloys. Specifically, the evolution of long range ordering (LRO) and hardening as a function of stoichiometry is addressed. 2) Discover the role of LRO domain on the deformation mode under different loading orientation in single grain in Ni-Cr binary model alloys in [001] grain orientation. 3) Characterize the microstructure and deformation behavior in AM316L alloy. For AM316L, systematic

microstructural characterization and in situ micro compression testing were performed to explore the effect of additive manufacture.

The rest of this document is organized as follows: Chapter 2 is a manuscript addressing objective one, titled “Effect of stoichiometry on the evolution of long range ordering in NixCr Alloys”. The chapter 2 manuscript will be submitted to Acta Materialia. Chapter 3 is the manuscript addressing objective two, titled “Investigation of the hardening effect of Ni_2Cr LRO domain as function of grain orientation by in situ micropillar compression testing”. The chapter 3 manuscript will be submitted to Nature Materials. Chapter 4 is a manuscript on the role of dual-phase structure on the mechanical properties of additive manufactured 316L stainless steel. This manuscript addresses objective 3 and will be submitted to Materials & Design.

2 Chapter 2: Effect of stoichiometry on the evolution of thermally annealed long-range ordering in Ni_xCr alloys

Fei Teng [a], David J. Sprouster [b], George A. Young [a,c], Jia-Hong Ke [a], and Julie D. Tucker [a, *]

[a] Materials Science Program, Mechanical Industrial Manufacturing Engineering Department, Oregon State University, Corvallis, OR, 97331, USA.

[b] Nuclear Science and Technology Department, Brookhaven National Laboratory, Upton, NY 11973-5000, USA.

[c] Dominion Engineering Inc, Schenectady, NY.

2.1 Abstract

Ni-based alloys, such as alloys 690, 625, and 625+, are widely used in the nuclear industry as structural components, because of their extraordinary corrosion and stress corrosion cracking resistance that results from their high fracture toughness and high Cr content. However, a disorder-order phase transformation near 33at.% Cr, is known to decrease ductility and fracture toughness. In this study, the ordering transformation is investigated in Ni-Cr binary model alloys with varying composition to determine the range of susceptibility for ordered phase formation. Model alloys with different stoichiometries (Ni/Cr = 1.8, 2.0, 2.2, 2.4) were isothermally aged up to 10,000 h at three temperatures (373ºC, 418ºC, and 475ºC) and characterized by transmission electron microscopy (TEM), microhardness, and synchrotron-based X-ray diffraction (XRD). TEM results show the evolution of $MoPt_2$-type ordered precipitates between 3000 h and 10,000 h with corresponding size of ~10 nm to 20 nm. Microhardness

testing results shows that off-stoichiometry (Ni/Cr ≠ 2.0) alloys exhibit a smaller change with ordering compared to the stoichiometric (Ni/Cr = 2.0) alloy at all temperatures. XRD quantifies ordering induced lattice contraction in the matrix structure and the particle size of ordered precipitation. No BCC Cr was detected by XRD or TEM during characterization in the range of 29.83 to 35.66 at% Cr after 10,000 h of aging.

2.2 Introduction

High Cr, Ni-based alloys are widely used in various industrial fields, including nuclear, aerospace, environmental engineering. For Ni-Cr based systems, 600 series alloys with ~20 – 30 wt% Cr (e.g. 690, 625, and 625+) have been widely used in key components of light water reactors, due to the outstanding mechanical and chemical properties relative to Fe-based alloys [21]. The high yield strength, fracture toughness, corrosion resistance, and phase stability during ageing make Ni-based alloys strong candidate materials for nuclear power plant components, such as reactor pressure vessel heads, core structural internals and steam generator tubing. The 700 series superalloys with ~15 – 20 wt.% Cr (e.g. X-750, 718 and 725) are widely used in rotor blades and wheels of gas turbines system, due to the corrosion, oxidation resistance, and high strength under high temperature environment [22]. Hastelloy C22 with 22 wt.% Cr has been widely used under extreme corrosive environment such as groundwater systems due to the excellent resistance to corrosion and stress corrosion [23]. In Ni-Cr system, precipitates of long-range ordering (LRO) in Ni-based superalloys are generally recognized as the major strengthening phases for high-temperature applications [24]. Previous thermodynamics studies reveal that an ordering transformation in Ni-Cr

binary system occurs in a relative low temperature region (300-590°C) around the Ni_2Cr stoichiometry [25-29]. The formation of the Ni_2Cr ordered phase was demonstrated to have detrimental impacts on mechanical properties and compromise the lifespan of structural components [30]. Previous research reveals that the degradation effect of ordering on Ni-based alloys has significant effects on the mechanical properties. These changes include: increasing hardness in Hastelloy C-22HS by Ni_2(Mo,Cr) ordered phase formation [31, 32], reducing fracture toughness [33], changing the fracture mode in Ni-Cr and Ni-Cr-X model alloys by Ni_2Cr [34], inducing internal stress in Nimonic 80A by Ni_2Cr [35], and increasing the susceptibility to hydrogen embrittlement in superalloy C-276 by Ni_2(Mo, Cr) formation after long term ageing [36]. General effects of the LRO transformation include a decreases in lattice parameter [29, 37, 38] and change in slip mode [29]. Due to the significant degeneration caused by LRO, studies on the kinetics of the ordering transformation have also been performed [39, 40]. In this paper, we have studied the ordering transformation in Ni-Cr binary model alloys with varying composition to better understand the range of the Ni_2Cr ordered domain on the phase diagram and to evaluate its influence on mechanical properties.

The Ni_2Cr ordered phase has been identified as $MoPt_2$-type precipitates with Immm symmetry [34, 41-44]. Figure 2-1 shows the $MoPt_2$ ordering superlattice structure in the Ni-Cr system. Under the reference lattice of face-centered cubic (FCC) structure, ordered Ni_2Cr phase is of body-centered orthorhombic (BCO) structure and fully coherent with FCC matrix. During the ordering transformation of Ni-Cr system, atoms reorganize from random solid solution into regular patterns [45]. The ordered

phase will nucleate and grow when the composition falls within the ordered phase region or in a two-phase region (e.g., bcc Cr + Ni_2Cr) [27-29, 46, 47].

The kinetics and thermodynamics of ordering transformations are heavily dependent on stoichiometry and temperature. The ordered phase has a Ni/Cr ratio of 2, however, the width of the ordered domain is poorly defined due to the challenge of collecting low temperature phase equilibrium data. Commercial alloys, such as 690, 625 and 625+, are possibly located in the ordering phase transformation field of the Ni-Cr phase diagram (30-35 at.% Cr range) as reported by Marucco et al. [28] and Xiong et al. [26, 28, 29]. Table 1 provides the composition of some commercial alloys that may be at risk of ordering in service at low temperatures [41]. For Ni-Cr binary alloys, Young et al. and Karmazin et al. reported the optimal rate of ordering is ~475°C [41, 48]. Fe additions will lower the critical temperature of the ordered phase and the peak ordering rate, making it harder to accelerate testing in Ni-Cr-Fe ternary system at 475°C [41, 49, 50]. In the Ni-Cr-Mo ternary system, Mo additions raise the ordering critical temperature [51] as reported by Arya et al. and stabilize the ordered phase according to Karmazin et al. [52]. In commercial alloys, Delabrouille et al. reported ordering in Inconel 690 after a 70,000 h heat treatment at 420°C via the evolution of microhardness and TEM characterization [25]. Irradiation was also found to enhance the ordering rate significantly for both model alloys and commercial alloys. Frely et al. reported ordering kinetics in Ni-Cr-Fe model alloys can be enhanced in orders of magnitude by 2.5 MeV electron irradiation [49, 50]. In the research of Song et al., twelve commercial alloys (including C22, 690, 625, 625+, 725, etc.) were found to produce the Ni_2Cr LRO via

TEM dark field imaging when irradiated using 2 MeV proton at 360°C with 2.5 dpa damage level [53].

Table 1. Chemical composition of Ni, Cr, Fe of some commercial alloys (at %).

Alloy	Ni	Cr	Fe	Ni/Cr
690	> 60.0	31.7-34.8	7.7-11.0	1.65-1.90
625	> 60.0	26.2-29.0	< 6.0	2.23-2.57
625+	70-74.0	25.2-29.0	<11.0	2.37-2.94
C22	66.5	29.5	3.7	2.25

Due to the lower critical temperatures in Fe containing commercial alloys, binary Ni-Cr alloys are usually used to clarify the behavior and influence of ordering. In previous research on binary Ni-Cr alloys, the hardening effect can be observed by measuring microhardness. A linear relationship between Vickers microhardness and yield strength was reported by Young et al. in Ni-33 at.% Cr binary alloy, which was isothermally heat treated at 475°C for up to 10,000 h [34]. The effect of ordering transformation on crack growth of Ni_2Cr binary alloy has been explored in previous research of Pao et al., which indicates that fatigue crack growth rate decrease and crack growth thresholds increase with the extent of ordering [54]. Ordered precipitates can be qualitatively characterized by both indirect methods, such as microhardness [46, 55, 56], and direct methods, such as atom probe tomography (APT) [57, 58], TEM [41, 59], and X-ray diffraction (XRD) [55]. However, a systematic quantitative study on the evolution of LRO has not been performed due to the difficulty on quantifying the ordered phase fraction and the relationship with mechanical properties even with advanced characterization techniques such as TEM and APT. There is little

experimental data in this region (29-36 at.% Cr, T = 373°C-475°C) to confirm the extent of the ordered phase at different temperatures and different stoichiometry from previous research. The role of stoichiometry in Ni_2Cr and Ni_3Cr binary alloys and Ni-Cr-Fe ternary alloys (30-67 at.% Ni, 17-32 at.% Cr, and 1-51 at%. Fe) has been studied by Marucco between 450 and 600°C [28, 47]. Her results reveal that the degree of ordering in ternary alloys relies on the Cr concentration, and the kinetics is reduced when the Ni/Cr ratio departs from Ni/Cr = 2. Similar results are also observed in Ni-Cr binary alloys between 550 to 1000°C [48]. However, both researchers do not cover the most common service temperature in the piping system of light water reactor (300 to 400°C). The purpose of this work is to explore the relationship between extent of ordering, temperature, and stoichiometry in Ni-Cr binary system at low temperature range to contribute the lifetime prediction modeling in Ni-based commercial alloys used in applications requiring a long service life in future.

In this study, four compositions of Ni-Cr alloys (30-36 at.% Cr) were aged at three temperatures (373°C, 418°C, 475°C) for up to 10,000 h. TEM characterization was performed to reveal the evolution of Ni_2Cr ordered precipitation in the microstructure. Then Berkovich microhardness was used to measure the ordered phase induced increasing on microhardness as function of temperature and stoichiometry. Finally, XRD was used to characterize the evolution of ordered precipitates and matrix including phase fraction, lattice parameter, size of ordered phase, and internal strain.

2.3 Experimental Methods

2.3.1 Fabrication of model alloys

The Ni-Cr binary model alloys were fabricated by small batch (~300g) arc-melting, then hot-rolled into plates, and homogenized in a furnace for 24 h at 1093°C. After homogenization, all samples are water-quenched to room temperature. Samples were made in stoichiometry ratios of Ni/Cr (at.%) of 1.8, 2.0, 2.2, and 2.4, which follows the unknown region of the Ni-Cr phase diagram under 500°C from previous research [26]. Compositional analysis was performed by a third-party test laboratory. The analytical method is based on CAP-017N (ICP-AES) and ASTM 1019-11 (Comb./IGF). The actual composition results are shown in Table 2. The rolled plates were cut into 10×10×5 mm^3 specimens by electrical discharge machining, which minimizes heat generation and the corresponding interpretation on microstructure during cutting. Next, specimens were isothermal heat-treated at three temperatures (373, 418 and 475°C) for up to 10,000 h. Each furnace has three thermocouples that measure the temperature around samples and the whole ageing system is monitored by the program written in LabView combined with National Instrument cDAQ-9171 chassis and NI-9214 temperature input module. All thermal couples are calibrated by Fluke 9142 Field Metrology Wells. The reference temperature is measured from 5610 Fluke Temperature Probes. All samples are cooled by water quenching to room temperature after aging. The heat treatment matrix is shown in Table 3.

Table 2. Composition of binary model Ni-Cr Alloys (at%). Values of Ni/Cr are used in following to clarify stoichiometry.

Element	Ratio 1.8	Ratio 2.0	Ratio 2.2	Ratio 2.4
C	0.05	0.05	0.05	0.05
Cr	35.66	33.24	31.10	29.83
Fe	<0.01	<0.01	<0.01	<0.01
P	<0.01	<0.01	<0.01	<0.01
S	<0.002	<0.002	<0.002	<0.001
Ni	64.27	66.69	68.83	70.10
Ni/Cr	1.80	2.01	2.21	2.35

Table 3. Heat treatment matrix of model Ni-Cr alloys. One sample from each stoichiometry is included in each time/temperature group.

Time (h) **Temperature (°C)**	**500**	**1000**	**3000**	**5000**	**10,000**
373	4	4	4	4	4
418	4	4	4	4	4
475	4	4	4	4	4

2.3.2 TEM

After aging, specimens to be characterized by TEM were first sectioned by low speed diamond saw into ~1 mm thick slices. The slices were then ground to thin foil with the thickness less than 120 μm with 1200 grit SiC sandpaper finished surface on both sides. The foils were punched into 3 mm diameter disks and jet electro-polished in 20% $HClO_4$ – 80% CH_3OH at -40°C and 15V using a Struers Tenupol 5 with a Julabo FP50 closed-cycle refrigeration system.

TEM characterization was performed by using the FEI Tecnai TF30-FEG transmission electron microscope located in Center for Advanced Energy Studies

(CAES) at 300 kV voltage. To best reveal the size of precipitation, [112] zone axis was selected for dark field imaging.

2.3.3 Microhardness

For microhardness tests, the bulk specimens (in dimension of 10×10×5 mm^3) were polished using SiC papers from 240 to 800 grit followed by 0.05 μm colloidal alumina polishing to create flat surfaces. Microhardness measurements were performed by using MicroMaterials NanoTest Vantage nanoindenter with a Berkovich diamond tip and a load of 500 mN. The load was chosen to balance degradation of indenter tip, sensitivity for vibration from environment during testing, resistance on effect of grain orientation, effect of grain boundary on indentation, and the accuracy level of the result. A larger load causes faster tip damage, which changes the dynamic area function that is used to calculate microhardness. A smaller load requires lower environmental vibration. Additionally, grain orientation and presence of grain boundaries will have negative effect for increasing the uncertainty of measuring microhardness. Considering these effects on standard deviation of measurement, microhardness measurements using a grid of (4×5) were performed twice (totally 40 indents) on the sample surface with 600 μm between indentations in each direction. Considering the effect of grain orientation and grain boundary on data variance, all 40 data points are ranked from low to high and the lowest 10 and highest 10 points will be removed from data set. Only the remained middle 20 data points will be analyzed to perform result.

2.3.4 Synchrotron X-ray diffraction (XRD)

XRD measurements were performed using the high-energy X-rays available the X-ray Powder Diffraction beamline of the National Synchrotron Light Source-II (NSLS-II) [60, 61]. All measurements were performed in transmission mode with an amorphous Silicon-based flat panel detector (Perken-Elmer) mounted orthogonal to and centered on the beam path. The sample-to-detector distances and tilts of the detector relative to the beam were refined using a LaB_6 powder standard (NIST standard reference material 660c). The wavelength of the incident X-rays was 0.2370 Å (52.3149 keV). The sample-to-detector distance was calculated to be 1351.94 mm. Samples were continuously rotated during acquisition to improve the powder averaging. Multiple patterns were collected to avoid saturation of the detector. Typical count times were 0.5-1 sec (depending on the sample). All raw two-dimensional patterns were background corrected by subtracting the dark current image and any air scattering. Noticeable artefact regions of the detector (like the beam stop, dead pixels) were masked. The corrected and masked two-dimensional detector images were then radially integrated to obtain the one-dimensional powder diffraction patterns. The background subtracted XRD patterns were Rietveld refined with the TOPAS software package (BRUKER). The peak profiles were modeled by a modified pseudo-Voigt function. The instrument contribution to the broadening of the measured profiles was quantified by fitting a LaB_6 NIST powder standard, with known crystalline-domain size and negligible strain contribution. The Gaussian and Lorentzian-based broadening parameters were subsequently fixed during the analysis of the alloys under investigation.

Table 4 shows the test matrix for XRD characterization. To best reveal the evolution of ordered phase, Ni/Cr = 2.0 samples aged at 475℃ were chosen to perform the test. Ni/Cr = 2.0 samples aged at 373℃ and 418℃ for 10,000 h were also tested for exploring the role of temperature in ordering transition. Moreover, Ni/Cr = 1.8, 2.2, and 2.4 samples were chosen to reveal the evolution of ordering as a function of stoichiometry.

Table 4. Test matrix for XRD. Tested stoichiometry is shown in each table cell.

Time (h) **Temperature (°C)**	**500**	**1000**	**3000**	**5000**	**10,000**
373					2.0
418					2.0
475	2.0	2.0	2.0	2.0	1.8, 2.0. 2.2, 2.4

2.4 Results

2.4.1 Transmission electron microscopy

Figure 2-2 shows the evolution of $MoPt_2$-type ordered precipitates with time snapshots of 3000 h, 5000 h, and 10,000 h ageing at 475℃ in [112] zone axis. In dark field mode, both $\frac{1}{3}$ [220] and $\frac{1}{3}$ $[13\bar{1}]$ spots were captured for Figure 2-2(a). The $\frac{2}{3}$ [311] and $\frac{2}{3}$ [220] spots were selected for Figure 2-2(b) and 2(c).

The diffraction patterns indicate the existence of the ordered phase after isothermal ageing and the corresponding dark field images reveal the distribution of Ni_2Cr-ordered precipitates in samples. TEM dark field images generally reveal the evolution of ordering transition in quality as ageing going. After 3000 h ageing (Figure

2-2(a)), small ordered precipitates can be observed, and some precipitates start growing into an early stage superlattice structure with a size ~10 nm. As ageing continues, ordered precipitates with larger coherent particle size (p-size) of ~13 nm can be observed after 5,000 h isothermal heat treatment and the superlattice structure is more obvious (Figure 2-2(b)). P-size keeps growing at ~20 nm as ageing time comes to 10,000 h (Figure 2-2(c)). The superlattice structure of thermal induced Ni_2Cr ordered structure can be observed in some area clearly. Figure 2-2 shows the boundary between precipitates is getting clearer with increasing aging time. No clear precipitate can be observed in Figure 2-2(a) (3000 h). Dark area between precipitates start showing in Figure 2-2(b) (5,000 h) and clear precipitates can be images clearly in Figure 2-2(c) (10,000h). However, it is difficult to calculate ordered phase fraction from TEM darkfield images because of the low contrast between matrix and ordered precipitates. More precise, robust, and larger volume characterization method, such as synchrotron XRD, is needed to determine precise ordered phase fractions.

2.4.2 Microhardness

The average change in Berkovich microhardness, which is the difference of microhardness before and after isothermal ageing, from 500 to 10,000 h isothermal heat treatment as function of stoichiometry at three temperatures are shown in Figure 2-3. The result shows that the relationship of embrittlement at three temperatures is generally 475℃ > 418℃ > 373℃ during the whole ageing time. Embrittlement can be defined as difference of Berkovich microhardness at current ageing time (GPa) and the microhardness of same sample at as-received condition (GPa).

In first 500 and 1,000 h ageing (Figure 2-3(a) and Figure 2-3(b)), the change in microhardness as a function of temperature is 475°C > 418°C > 373°C. The change on microhardness as a function of stoichiometry at 475°C is 2.0 ≈ 2.2 > 1.8 ≈ 2.4. The role of stoichiometry at 418°C and 373°C on embrittlement is not obvious; the four stoichiometries reveal similar microhardness changes at both temperatures. When the ageing time extends after 3,000 h (Figure 2-3(c)), role of stoichiometry starts showing out more obviously at 475°C. The relationship of embrittlement as a function of stoichiometry is 2.0 > 2.2 ≈ 1.8 > 2.4 at 475°C. The relationship keeps stable at 418°C compared to the relationship before 1,000 h. For the embrittlement at 373°C, the 2.2 sample is of slightly larger embrittlement than other compositions. Compared to the embrittlement before 1,000 h, no obvious change in the relationship of embrittlement can be observed at 373°C. However, the degree of embrittlement, which is between 0.3 and 0.75 GPa, is much larger than that of 500 h and 1,000 h, which is between 0 and 0.25 GPa. When the ageing time equals to 10,000 h (Figure 2-3(d)), the relationship of embrittlement at all temperatures is close to 2.0 > 2.2 ≈ 1.8 > 2.4. Compared to the tendency at 3,000 h (Figure 2-3(c)), the embrittlement at 475°C is similar. For 418°C, the embrittlement increases to 1 GPa at all stoichiometry, which is larger than 5,000 h. For 373°C, the change of microhardness is of obvious increasing compared to that of 5,000 h.

The size of nanoindentation is ~20 μm, which is smaller than the grain size (~150 μm). The size difference may cause the measurement of microhardness is heavily dependent on grain properties, such as grain orientation and grain boundary effect. The uncertainty revealed in the hardness measurements, indicates microhardness needs to

be combined with another more reliable technique to clarity the evolution of ordering as a function of temperature and stoichiometry.

2.4.3 Synchrotron X-ray Diffraction

Considering the challenge of measuring ordered phase fraction by TEM and grain properties influenced microhardness, XRD is the ideal technique to precisely quantify the evolution of ordered precipitation. Also, previous research from Gwalani et al. [55] shows the efficiency of XRD on identifying ordered precipitation.

The XRD patterns are shown in Figure 2-4 (phases are included for reference), confirming the formation of the Ni_2Cr ordered phase. All samples show the cubic FCC Ni-Cr matrix (higher peaks indicated by the blue tick marks). All samples, with the exception of the "as received" sample, show peaks from the orthorhombic phase Ni_2Cr (red tick marks). The peaks from the Ni_2Cr phase vary in height and width between samples due to varying concentration and coherent particle size (p-size). There does not appear to be any diffraction peaks for BCC Cr in the current samples. In Figure 2-4(a), compared to as-received 2.0 sample, both 2.0-475-5000 and 2.0-475-10,000 samples show Ni_2Cr diffraction and the corresponding intensity increases with ageing time, as confirmed by quantitative analysis (Table 5). Figure 2-4(b) reveals diffraction patterns that confirm the formation of the Ni_2Cr ordered phase in all four stoichiometries. Figure 2-4(c) shows the diffraction pattern from samples with different ageing temperatures (373℃, 418℃, and 475℃). Significant peak broadening can be observed in the Ni_2Cr precipitates at lower temperatures, indicative of small precipitate. The lattice parameters (and volume of unit cell) also appear to be temperature dependent and increase with increasing temperature.

The structural results from the Rietveld fitting are shown in Table 5 and Figure 2-5 for the phase fraction, lattice parameter (for both matrix and precipitates), size of ordered precipitation (p-size) and strain (number to the right is the error bar from the refinements). The blue (dash line) plot of Figure 2-5 shows the evolution of p-size as a function of ageing time for Ni/Cr = 2.0 samples aged at 475℃. The p-size increases rapidly in the beginning period of heat treatment then starts slowing down after 1,000 h. A similar but reversed trend can be observed on the change of lattice parameters in same sample as shown in the green (dots line) plot in Figure 2-5. Lattice of the matrix contracts rapidly in the beginning 1,000 h from 3.567 Å, and then plateaus around 3.558 Å. The pink (dash-dot line) plot in Figure 2-5 shows the evolution of ordered phase fraction. Different from the tendency of other parameters, ordered phase goes to ~ 6% rapidly (at 500 h) and keeps going down till 5000 h. Ordered phase fraction keeps stable at ~5% after 5000 h. The black (solid line) plot shows the evolution of microhardness on the same samples for comparison. Figure 2-6 shows change of strain on Ni/Cr = 2.0 jet-polished samples from 3000 h to 10,000 h. A significant jump on strain can be observed between 5000 h and 10,000 h. Figure 2-7 shows the evolution of strain, p-size, and change in microhardness as a function of stoichiometry. Ni/Cr = 2.0 and 2.4 samples have the largest and smallest values on all parameters correspondingly, which means the farther distance from 2.0, the smaller p-size/strain/change in microhardness can be observed in the sample. Ni/Cr = 1.8 sample is of slightly larger size on precipitates than Ni/Cr = 2.2.

Table 5. Summary and comparison of Rietveld refinements.

sample	phase	a (Å)	±	b (Å)	±	c (Å)	±	Phase Fraction (%)	±	p-size (nm)	±	strain	±

2.0 As received	Fm-3m	3.56720	0.00005									0.28	0.01
2.0-500hr-475°C	Fm-3m	3.56031	0.00013									0.23	0.02
	Immm	2.50639	0.00696	7.52024	0.02264	3.59554	0.00638	6.0	0.2	9	0.5		
2.0-1,000hr-475°C	Fm-3m	3.55875	0.00010									0.39	0.01
	Immm	2.50923	0.00253	7.50987	0.00845	3.59472	0.00258	5.8	0.2	12.9	1.0		
2.0-3,000hr-475°C	Fm-3m	3.55860	0.00016									0.24	0.02
	Immm	2.50747	0.01200	7.53310	0.03940	3.56688	0.01598	5.6	0.69	12.4	2.0		
2.0-5,000hr-475°C	Fm-3m	3.55853	0.00009									0.23	0.01
	Immm	2.50323	0.00834	7.50819	0.02548	3.60427	0.00721	4.7	0.2	15.0	2.0		
2.0-10,000hr-475°C	Fm-3m	3.55790	0.00010									0.54	0.01
	Immm	2.50816	0.00311	7.50204	0.00940	3.59506	0.00239	4.9	0.2	19.0	1.1		
1.8-10,000hr-475°C	Fm-3m	3.56387	0.0001									0.5	0.011
	Immm	2.51294	0.00213	7.5324	0.00659	3.5855	0.0023874	6	0.3	15	2		
2.2-10,000hr-475°C	Fm-3m	3.55598	0.00013									0.47	0.01
	Immm	2.50852	0.00240	7.51625	0.00910	3.58372	0.00250	12.1	0.5	12.7	1.0		
2.4-10,000hr-475°C	Fm-3m	3.55570	0.00012									0.39	0.01
	Immm	2.51187	0.00480	7.57838	0.01850	3.57230	0.00540	6.8	0.5	8.0			
2.0-10,000hr-373°C	Fm-3m	3.56158	0.00010									0.24	0.01
	Immm	2.48545	0.01000	7.52002	0.03100	3.63926	0.00800	6.6	0.2	4.0			
2.0-10,000hr-418°C	Fm-3m	3.55954	0.00009									0.29	0.01
	Immm	2.50636	0.00637	7.52694	0.02159	3.59439	0.00592	9.5	0.3	6.7	1.0		

2.5 Discussion

2.5.1 Evolution of ordered precipitation in isothermal aged Ni-Cr binary system

XRD and TEM results reveal the evolution of ordered precipitation among Ni/Cr = 2.0 samples. Ni/Cr = 2.0 samples are used here to qualify and quantify the evolution of thermal ageing induced ordering and to confirm the reliability of microhardness result in all samples as the microhardness starts showing saturation behavior. Figure 2-5 shows the comparison between the evolution of p-size, lattice parameter, ordered phase fraction, and microhardness as function of time. For 2.0 sample aged at 475°C, XRD result shows that the evolution of the lattice parameter of matrix, size of ordered

particle, and microhardness reach saturation after 1,000 h ageing. The tendency agrees with each other between the parameters except ordered phase fraction. The XRD measured p-size fulfills the result of TEM characterization (Figure 2-2), which indicates the significant increasing from 5000 h to 10,000 h (Figure 2-5).

Compared to the most recent TEM characterization from Miao et al. [53] on irradiated commercial alloys, the size of precipitates are an distinctly different. The difference on phase fraction and p-size is larger compared to the samples with high Mo content in the research of Verma et al. [56] due to the ordering rate enhancement of Mo in Ni-Cr system. Previous researchers have shown that the addition of Mo, Nb, and W is able to stabilize ordered precipitates at high temperatures [52, 62, 63]. In comparison with previous TEM characterization of Ni-Cr binary alloys, similar observation can be observed from the select area electron diffraction (SAED) pattern and dark field images [41, 55]. In previous research of Ni-Cr model alloys, only small precipitates are considered to be LRO precipitate in dark field mode. By condensing the electron beam in dark field mode, the dark field image with uneven intensity reveals both small precipitates and surrounding grey region (Figure 2-2(a)). The grey area, which contains both small precipitates with weak intensity and some matrix material, can be removed by adjusting image contrast and brightness. The superlattice structure from LRO Ni_2Cr precipitates is visible after 3,000 h of ageing in Figure 2-2(a). As ageing continues, the ordered precipitates start unifying into superlattice structures (Figure 2-2(b)). In Figure 2-2(b) and 2(c), the p-sizes are ~10 nm and ~10 – 20 nm, which is in rough agreement with the measurement of p-size by XRD (15 ± 2 nm and 19 ± 1.1 nm correspondingly). Therefore, the evolution of LRO precipitation can be clearly observed and described as

two stages based on the result of TEM characterization: the forming of nuclei and the growing of nuclei, which is shown in Figure 2-2.

Ordered Ni_2Cr nuclei are formed at the early stage under the driving of diffusion. As thermal ageing continues, the surrounding area of nuclei starts ordering and the texture of ordered superlattice texture starts to be visible. In previous work by Marucco et al. [29], the change of lattice parameter is considered to be a direct effect of LRO. Combined with the lattice contraction from XRD (Figure 2-4(a)), all samples characterized by TEM, which are 2.0-475℃-3,000 h, 2.0-475℃-5,000 h, and 2.0-475℃-10,000 h, are in the ordering saturation region. Lattice parameter of matrix is getting stable at 3.558 Å from original 3.567 Å (Figure 2-4(c)), which is 0.25% lattice contraction and reported to be the lattice constant value of saturation of ordering in Ni-Cr binary system by Marucco et al. [29, 46]. The lattice parameter result of XRD is very close to result from Gwalani et al. [55].

P-size increases with ageing time and no saturation can be observed during the evolution, but only slower increasing tendency can be observed from XRD result (Figure 2-5). The tendency indicates p-size is of a significant growth between 5000 h and 10,000 h while the ordering induced lattice contraction effect, ordered phase fraction and microhardness is stabilizing in Figure 2-5. To reveal the other effect of p-size, strain was calculated from XRD in 3000 h, 5000 h, and 10,000 h jet polished TEM disk to minimize the effect of external induced strain in the result of calculation (Figure 2-6). Result shows the big jump of strain from 5000 h to 10,000 h, which indicates that the internal strain may be induced by growing p-size instead of change of ordered phase fraction or lattice contraction.

2.5.2 Effect of phase fraction and p-size on hardening

For Ni/Cr = 2.0 samples at 475℃, the similarity between p-size, lattice parameter, and microhardness (Figure 2-5) indicate the strong relationship between size of ordered particle, ordering induced lattice contraction and the corresponding hardening effect. The evolution of ordered phase fraction in Figure 2-5, however, shows a different behavior from other ordering induced parameters. Ordered phase fraction reaches ~6% by 500 h of ageing, slowly decreases to ~5% from 500 h to 5000 h. Then ordered phase fraction gets stable ~5% from 5000 h to 10,000 h. The saturation of ordered phase fraction (at ~500 h) happens earlier than other parameters (at ~1000 h). By combining the result of p-size and ordered phase fraction, we can have a rough idea about the morphology change during the evolution of ordering: ordered precipitates distributed in small but high density at the early stage, then it changed to large but low-density precipitates with small precipitates interstitially at the later stage of ageing.

In the precipitation hardening mechanism of Ni-based alloys, the major factors of strengthening of due to γ' in Ni-based superalloys are coherency strain and the presence of order in the particles. Previous research has built the Orowan dislocation bypass model for γ' [Ni_3(Al, Ti)] coherent long range ordering precipitates when the particle-matrix interfacial energy is neglected [64]. The relationship gives equation (1).

$$\tau_I = \left(\frac{2r_s\gamma_0}{L_I b}\right)^{\frac{1}{3}} \qquad (1)$$

When a dislocation pass through an ordered particle, force $\tau_I b$ must be equal to antiphase boundary energy, which is $\frac{2r_s\gamma_0}{L_I}$. In equation (1), γ_0 is antiphase boundary

energy, r_s is the average radius of particle intersected by a slip band, L_I is the spacing between ordered particles. Based on the result of XRD, particle size of ordered precipitates (p-size) changed from 0 nm to ~20 nm during the whole ageing process, while TEM result shows that the spacing between ordered particles may not change significantly as the co-existance of large and small ordered precipitates. Back to equation (1), the change of r_s is significantly larger than L_I, which makes the dislocation bypassing force increase. Equation (2) give out the expression of for dislocation obstacle spacing L' as a function of applied stress τ:

$$L' = \left(\frac{2TL_s^2}{\tau b}\right)^{\frac{1}{3}} \qquad (2)$$

$$L_I' = \left(\frac{2T\pi r_s^2}{f\tau_I b}\right)^{\frac{1}{3}} \qquad (3)$$

The fraction of dislocation line cutting particle is defined to be:

$$\frac{2r_s}{L_I} = \left(\frac{4\gamma_0 f r_s}{\pi T}\right)^{\frac{1}{2}} \qquad (4)$$

L_I' is defined in equation (3), which stands for the particle with average radius r_s intersected by a slip band $\left(\frac{2}{3}\right)^{1/2} r_s$. Equation (4) is substituted into equation (1), then the stress that requires to force dislocation through ordered particle is shown in equation (5).

$$\tau_I = \frac{\gamma_0^{\frac{3}{2}}}{b}\left(\frac{4fr_s}{\pi T}\right)^{\frac{1}{2}} \qquad (5)$$

Where, T is line tension, and f is a constant. τ_I increases with particle size, which means the dislocation is more difficult to pass through larger particles in this case. The decreased mobility on dislocation causes hardening.

For Ni/Cr = 2.0 samples at 373℃ and 418℃, considering the relationship between ordering and the corresponding embrittlement effect in Ni-Cr system, change of microhardness can be trusted to indicate degree of ordering indirectly [29, 44, 55, 56, 65]. The trend of hardening (Figure 2-3) indicates that microhardness will reach nearly saturation after 1,000 h isothermal ageing at 475°C, whereas the time to reach saturation for 418 and 373°C will be longer than 10,000 h. Considering the embrittlement behavior of 418°C and 373°C have not reached equilibrium, the full behavior to saturation on microhardness cannot be concluded at those temperatures. The effect of stoichiometry on ordering is characterized by microhardness at all three temperatures (373°C, 418°C, and 475°C).

2.5.3 KJMA Analyses on microhardness as a function of stoichiometry

For the kinetics of thermal induced ordering transition, off-stoichiometry samples (Ni/Cr ≠ 2.0) are of lower maximum compared to in-stoichiometry sample (Ni/Cr = 2.0) when the kinetics is reaching saturation. In Figure 2-8, temperature shows a dominated role in the kinetics of ordering transformation. The increasing of temperature from 373°C to 475°C cause the increasing on p-size, strain and microhardness. The role of stoichiometry and temperature was quantified by equation fitting on hardness data. The microhardness data was fit by Kolomogorov-Johnson-Mehl-Avrami (KJMA) equation [66-70]. In the KJMA equation (6), *f* is the fraction of transformed structure among matrix, which is assumed to be ordered phase fraction

here, where *t* is the ageing time (h) and *n* is the Avrami exponent. The Arrhenius form of *k* shown in equation (7), where k_0 is a constant, Q is activation energy, R is the gas constant (8.314 J/mol.K), and T is the ageing temperature in Kelvin. Based on previous fitting work on microhardness and lattice parameter from Young et al. [34, 41], equation (6a) approximates the phase fraction in terms of changes in microhardness. Where H_0 is the initial microhardness, H_{Max} is the microhardness at saturation and H is the microhardness at a particular combination of ageing time and temperature.

$$f = 1 - e^{kt^n} \qquad (6)$$

$$k = k_0 e^{-Q/RT} \qquad (7)$$

$$f = \frac{H - H_0}{H_{Max} - H_0} \qquad (6a)$$

The result of KJMA fitting on microhardness shows in Figure 2-9. The fitting parameters used here are: k_0 = 3.00E+05 h^{-1}, Q = 120 kJ/mol, n = 0.75. The parameters agree with previous fitting result (k_0 = 3.50E+07 h^{-1}, Q = 147 kJ/mol, n = 0.65) on the similar samples and ageing conditions from Young et. al [41]. Even there is still some difference between the two groups parameters, the parameters from other sample preparation conditions (furnaced cooled: k_0 = 3.00E+15 h^{-1}, Q = 244 kJ/mol, n = 0.65; furnaced cooled + 10% cold work: k_0 = 2.00E+14 h^{-1}, Q = 244 kJ/mol, n = 0.65) are significantly different [41].

2.6 Summary

The role of stoichiometry on Ni-Cr ordering transformation was studied by microhardness and the extent of precipitation was confirmed by TEM and XRD. TEM

and XRD shows that the size of ordered precipitates (p-size) should be the primary factor for the evaluation of ordering transition instead of phase fraction. Ordering induced hardening effect primary comes from the growing of ordered domains and the corresponding effect such as lattice contraction and increasing internal strain.

The extent of ordering as measured by microhardness is greatest at 475°C compared to the medium (418°C) and low (373°C) temperature microhardness data. Ni/Cr=2.0 (33.24 at% Cr) alloy exhibited increased hardening due to precipitation of ordered Ni_2Cr compared to the off-stoichiometry samples at all three temperatures. A larger deviation from stoichiometry results in less hardening and ordering. Hardening behavior reaches a saturation point after 1,000 h ageing at 475°C for model alloys, which indicates a similar behavior on ordering transformation. The behavior at medium and low temperatures are more sluggish due to low diffusivities.

2.7 Acknowledgements

The authors want to acknowledge Dr. Alessandra Marucco et al. for the research on stoichiometry and Dr. Bharat Gwalani et al. for the research of XRD on identifying ordered structure. The previous research inspires author to perform the research in this paper. This research is being performed using funding received from the DOE Office of Nuclear Energy's Nuclear Energy University Program, Cooperative Agreement Number DE-NE0008423. This material is also based upon work supported by the National Science Foundation under Grant No. 1653123-DMR. This work was supported by the U.S. Department of Energy, Office of Nuclear Energy under DOE Idaho Operations Office Contract DE-AC07- 051D14517 as part of a Nuclear Science

User Facilities experiment. Use of the National Synchrotron Light Source-II, Brookhaven National Laboratory, was supported by the DOE under Contract No. DE-SC0012704.

2.8 References

[1] T. Allen, J. Busby, M. Meyer, D. Petti, Materials challenges for nuclear systems, Materials today 13(12) (2010) 14-23.
[2] T. Chester, S. Norman, C. William, Superalloys II, Eds. John Willey & Sons, Inc., New York (1976).
[3] K. Chiang, D. Dunn, G. Cragnolino, Effect of simulated groundwater chemistry on stress corrosion cracking of alloy 22, Corrosion 63(10) (2007) 940-950.
[4] E.O. Ezugwu, Z.M. Wang, A.R. Machado, The machinability of nickel-based alloys: a review, Journal of Materials Processing Technology 86(1) (1999) 1-16.
[5] F. Delabrouille, D. Renaud, F. Vaillant, J. Massoud, Long Range Ordering of Alloy 690, 14th Intl. Conference on Environmental Degradation of Materials in Nuclear Power Systems, Virginia Beach, VA, USA, 2009.
[6] W. Xiong, Thermodynamic and kinetic investigation of the Fe-Cr-Ni system driven by engineering applications, Department of Materials Science and Engineering, KTH Royal Institute of Technology, School of Industrial Engineering and Management, 2012.
[7] A. Marucco, Phase transformations during long-term ageing of Ni Fe Cr alloys in the temperature range 450–600° C, Materials Science and Engineering: A 194(2) (1995) 225-233.
[8] A. Marucco, Effects of composition on the order-disorder transformation in ni-cr based alloys, Key Engineering Materials, Trans Tech Publ, 1991, pp. 77-90.
[9] A. Marucco, B. Nath, Effects of Ordering on the Properties of Ni-Cr Alloys, Journal of Materials Science 23(6) (1988) 2107-2114.
[10] S. Lee, P. Nash, Phase diagrams of binary nickel alloys, ASM International, Materials Park (OH) (1991) 133.
[11] X. Xie, Y. Zeng, L. Kou, J. Dong, L. Pike, D. Klarstrom, THE PRECIPITATION AND STRENGTHENING BEHAVIOR OF Ni2 (Mo, Cr) IN HASTELLOY® C-22HS® ALLOY, A NEWLY DEVELOPED HIGH MOLYBDENUM NI-BASE SUPERALLOY, (2008).
[12] H.M. Tawancy, M.O. Aboelfotoh, High strength and high ductility in a nanoscale superlattice of Ni2(Cr,Mo) deformable by twinning, Scripta Materialia 59(8) (2008) 846-849.
[13] G.A. Young, D.S. Morton, N. Lewis, R. Morris, J. Pyle, L. Barnard, R. Najafabadi, Effect of long range order on the stress corrosion susceptibility of a nickel-33 at% chromium alloy, Corrosion 72(11) (2016) 1433-1437.

[14] G. Young, D. Eno, Long range ordering in model Ni-Cr-X alloys, Fontevraud 8 - Contribution of Materials Investigations and Operating Experience to LWRs' Safety,Performance and Reliability, France, Avignon, 2015.
[15] E. Metcalfe, B. Nath, A. Wickens, Some effects of the ordering transformation in Nimonic 80A on stress relaxation behaviour, Materials Science and Engineering 67(2) (1984) 157-162.
[16] K. Miyata, M. Igarashi, Effect of ordering on susceptibility to hydrogen embrittlement of a Ni-base superalloy, Metallurgical Transactions A 23(3) (1992) 953-961.
[17] F. Teng, J.D. Tucker, Role of Stoichiometry on Ordering in Ni-Cr Alloys, MRS Online Proceedings Library Archive 1809 (2015) 7-12.
[18] F. Teng, L.-J. Yu, O. Ciuca, E. Marquis, G. Burke, J.D. Tucker, The Role of Stoichiometry on Ordering Phase Transformations in Ni–Cr Alloys for Nuclear Applications, Environmental Degradation of Materials in Nuclear Power Systems, Springer, 2017, pp. 251-259.
[19] L. Barnard, G. Young, B. Swoboda, S. Choudhury, A. Van der Ven, D. Morgan, J. Tucker, Atomistic modeling of the order–disorder phase transformation in the Ni 2 Cr model alloy, Acta Materialia 81 (2014) 258-271.
[20] J.D. Tucker, R. Najafabadi, T.R. Allen, D. Morgan, Ab initio-based diffusion theory and tracer diffusion in Ni–Cr and Ni–Fe alloys, Journal of Nuclear Materials 405(3) (2010) 216-234.
[21] G.A. Young, J.D. Tucker, D.R. Eno, THE KINETICS OF LONG RANGE ORDERING IN NI-CR AND NI-CR-FE ALLOYS, (2013).
[22] J. Buršík, M. Svoboda, The existence of P phase and Ni2Cr superstructure in Ni-Al-Cr-Mo system, Scripta Materialia 39(8) (1998) 1107-1112.
[23] M. Hirabayashi, M. Koiwa, K. Tanaka, T. Tadaki, T. Saburi, S. Nenno, H. Nishiyama, An experimental study on the ordered alloy Ni2Cr, Transactions of the Japan Institute of Metals 10(5) (1969) 365-371.
[24] V. Kolotushkin, V. Kondrat'ev, A. Laushkin, V. Rechitskii, Effect of long-term aging on the structural and phase stability and properties of nickel-chromium alloys, Metal science and heat treatment 45(11) (2003) 411-414.
[25] L. Guttman, Order-Disorder Phenomena in Metals, in: S. Frederick, T. David (Eds.), Solid State Physics, Academic Press1956, pp. 145-223.
[26] A. Marucco, Atomic ordering and α′-Cr phase precipitation in long-term aged Ni3Cr and Ni2Cr alloys, Journal of materials science 30(16) (1995) 4188-4194.
[27] A. Marucco, Atomic ordering in the Ni Cr Fe system, Materials Science and Engineering: A 189(1) (1994) 267-276.
[28] L. Karmazin, Lattice parameter studies of structure changes of Ni Cr alloys in the region of Ni2Cr, Materials Science and Engineering 54(2) (1982) 247-256.
[29] E. Frely, B. Beuneu, A. Barbu, G. Jaskierowicz, Investigation of ordering kinetics in Ni-Cr-Fe alloys under electron irradiation, Annales De Physique (1997).
[30] E. Frely, B. Beuneu, A. Barbu, G. Jaskierowicz, Short and Long-Range Ordering of (Ni 0.67 Cr 0.33) 1-x Fe x Alloys Under Electron Irradiation, MRS Proceedings, Cambridge Univ Press, 1996, p. 373.

[31] A. Arya, G.K. Dey, V.K. Vasudevan, S. Banerjee, Effect of chromium addition on the ordering behaviour of Ni–Mo alloy: experimental results vs. electronic structure calculations, Acta Materialia 50(13) (2002) 3301-3315.
[32] L. Karmazin, J. Krejčí, J. Zeman, γ Phase and Ni2Cr-type long-range order in Ni-rich NiCrMo alloys, Materials Science and Engineering: A 183(1-2) (1994) 103-109.
[33] M. Song, Y. Yang, M. Wang, W. Kuang, C.R. Lear, G.S. Was, Probing long-range ordering in nickel-base alloys with proton irradiation, Acta Materialia 156 (2018) 446-462.
[34] P.S. Pao, S.J. Gill, C.R. Feng, D.J. Michel, Fatigue and fracture of a Ni2Cr ordered intermetallic alloy, Materials Science and Engineering: A 153(1) (1992) 532-537.
[35] B. Gwalani, T. Alam, C. Miller, T. Rojhirunsakool, Y.S. Kim, S.S. Kim, M.J. Kaufman, Y. Ren, R. Banerjee, Experimental investigation of the ordering pathway in a Ni-33 at.%Cr alloy, Acta Materialia 115 (2016) 372-384.
[36] A. Verma, J.B. Singh, N. Wanderka, J.K. Chakravartty, Delineating the roles of Cr and Mo during ordering transformations in stoichiometric Ni2(Cr1−x,Mox) alloys, Acta Materialia 96 (2015) 366-377.
[37] C. Pareige, F. Soisson, G. Martin, D. Blavette, Ordering and phase separation in Ni–Cr–Al: Monte Carlo simulations vs three-dimensional atom probe, Acta Materialia 47(6) (1999) 1889-1899.
[38] S. Meher, P. Nandwana, T. Rojhirunsakool, J. Tiley, R. Banerjee, Probing the crystallography of ordered Phases by coupling of orientation microscopy with atom probe tomography, Ultramicroscopy 148 (2015) 67-74.
[39] M. Sundararaman, L. Kumar, G.E. Prasad, P. Mukhopadhyay, S. Banerjee, Precipitation of an intermetallic phase with Pt 2 Mo-type structure in alloy 625, Metallurgical and Materials Transactions A 30(1) (1999) 41-52.
[40] X. Shi, S. Ghose, E. Dooryhee, Performance calculations of the X-ray powder diffraction beamline at NSLS-II, Journal of synchrotron radiation 20(2) (2013) 234-242.
[41] D.J. Sprouster, R. Weidner, S. Ghose, E. Dooryhee, T. Novakowski, T. Stan, P. Wells, N. Almirall, G. Odette, L. Ecker, Infrastructure development for radioactive materials at the NSLS-II, Nuclear Instruments and Methods in Physics Research Section A: Accelerators, Spectrometers, Detectors and Associated Equipment 880 (2018) 40-45.
[42] H.C. Pai, M. Sundararaman, B.C. Maji, A. Biswas, M. Krishnan, Influence of Mo addition on the solvus temperature of Ni2(Cr,Mo) phase in Ni2(Cr,Mo) alloys, Journal of Alloys and Compounds 491(1-2) (2010) 159-164.
[43] R. Hu, G.M. Cheng, J.Q. Zhang, J.S. Li, T.B. Zhang, H.Z. Fu, First principles investigation on the stability and elastic properties of Ni2Cr1−xMx (M = Nb, Mo, Ta, and W) superlattices, Intermetallics 33 (2013) 60-66.
[44] C.T. Sims, N.S. Stoloff, W.C. Hagel, superalloys II, Wiley New York1987.
[45] B.J. Berkowitz, C. Miller, The effect of ordering on the hydrogen embrittlement susceptibility of Ni2Cr, Metallurgical Transactions A 11(11) (1980) 1877-1881.
[46] A.N. Kolmogorov, On the statistical theory of the crystallization of metals, Bull. Acad. Sci. USSR, Math. Ser 1 (1937) 355-359.
[47] M. Avrami, Kinetics of phase change. III. Granulation, phase change, and microstructure, J. chem. Phys 9(2) (1941) 177-184.

[48] M. Avrami, Kinetics of phase change. II transformation-time relations for random distribution of nuclei, The Journal of Chemical Physics 8(2) (1940) 212-224.
[49] M. Avrami, Kinetics of phase change. I General theory, The Journal of chemical physics 7(12) (1939) 1103-1112.
[50] W.A. Johnson, R.F. Mehl, Reaction kinetics in processes of nucleation and growth, Trans. Aime 135(8) (1939) 396-415.

2.9 List of Figures

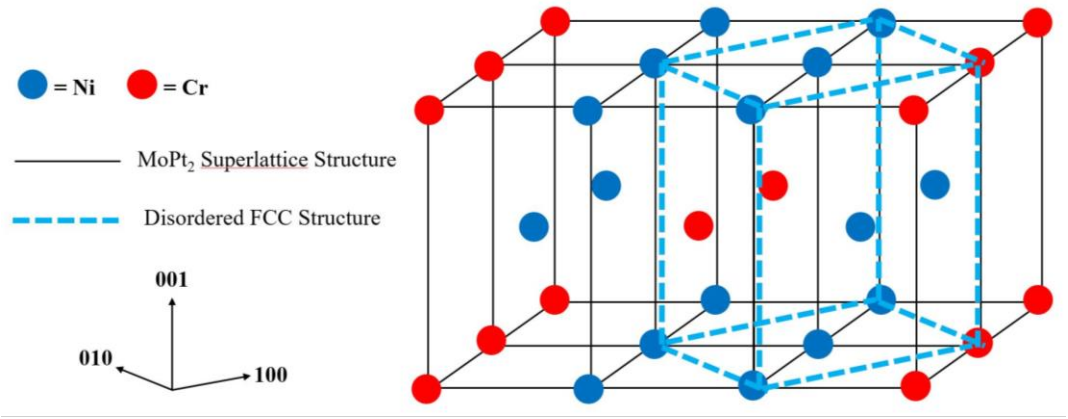

Figure 2-1. Schematic of $MoPt_2$ Superlattice Structure (Immm) in Ni-Cr (Fm-3m) System.

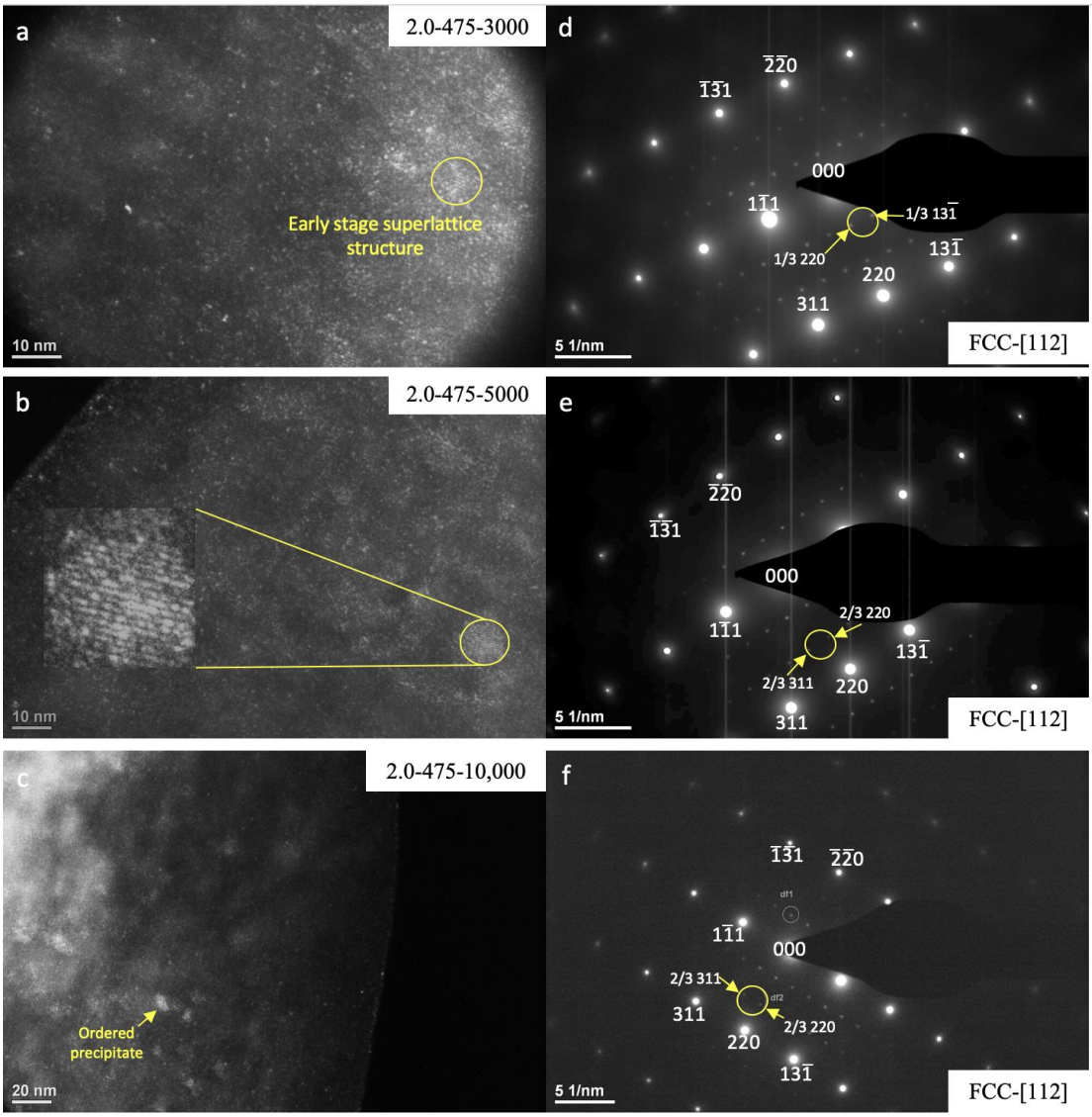

Figure 2-2. The evolution of ordering from 3000 to 10,000 h under TEM at [112] zone axis. (a) and (d) Darkfield image of Ni/Cr = 2.0 sample aged at 475°C for 3000 h and the corresponding diffraction pattern. (b) and (e) Darkfield image of Ni/Cr = 2.0 sample aged at 475°C for 5000 h and the corresponding diffraction pattern. The Ni2Cr superlattice structure is marked out and zoomed in. (c) and (f) Darkfield image of Ni/Cr = 2.0 sample aged at 475°C for 10,000 h and the corresponding diffraction pattern. Results shows that precipitation size for 3000 and 5000 h are similar, which is about 12 nm. The size of precipitation for 10,000 h aged sample is larger. Some precipitates are about 20 nm.

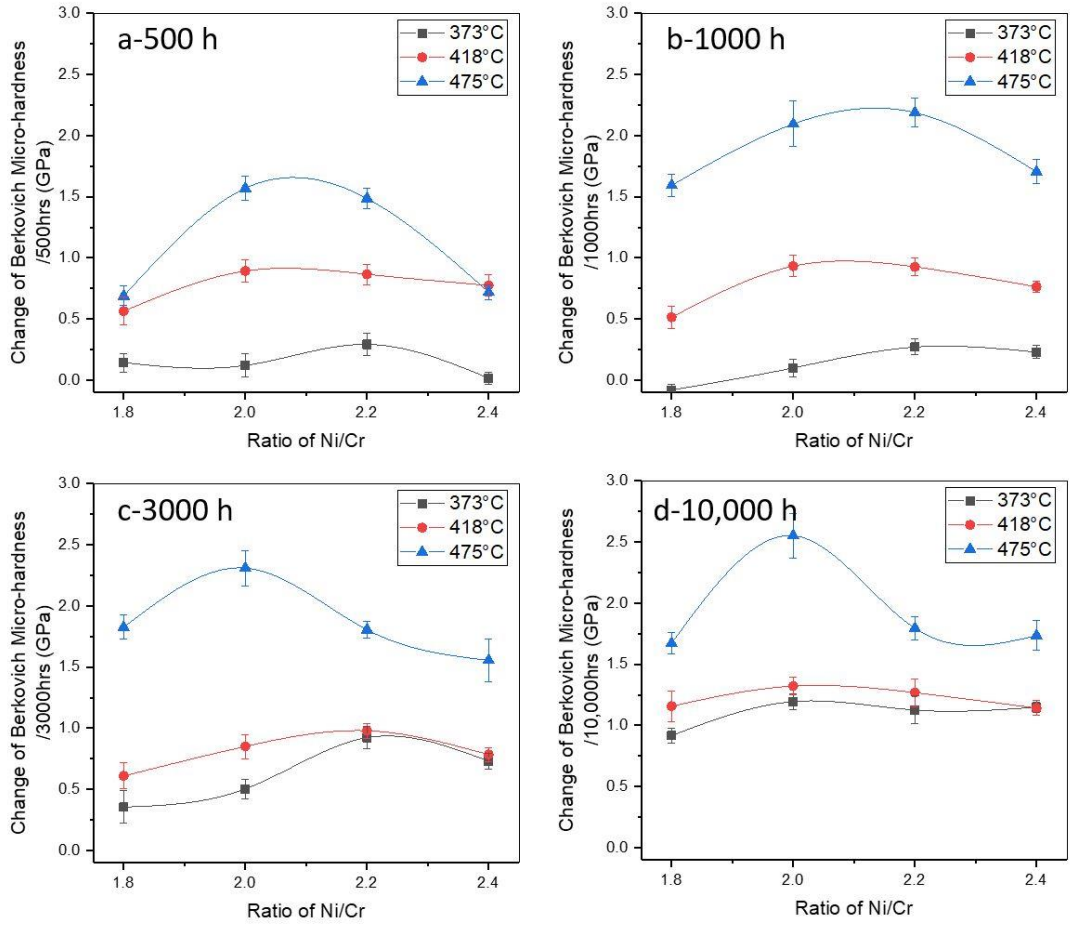

Figure 2-3. Change in microhardness as function of stoichiometry three temperatures when isothermal ageing comes to a) 500 h, b) 1,000 h, c) 3,000 h, and d) 10,000 h. The result shows that higher temperature is of earlier saturation on microhardness. 475℃ starts showing the saturation behavior. 373℃ and 418℃ have not reached saturation point, but the faster kinetic can be observed at 418℃ heat ageing. Ni/Cr = 2.0 samples are of highest value of change in hardness. Further distance from Ni/Cr =2.0 causes smaller change in hardness.

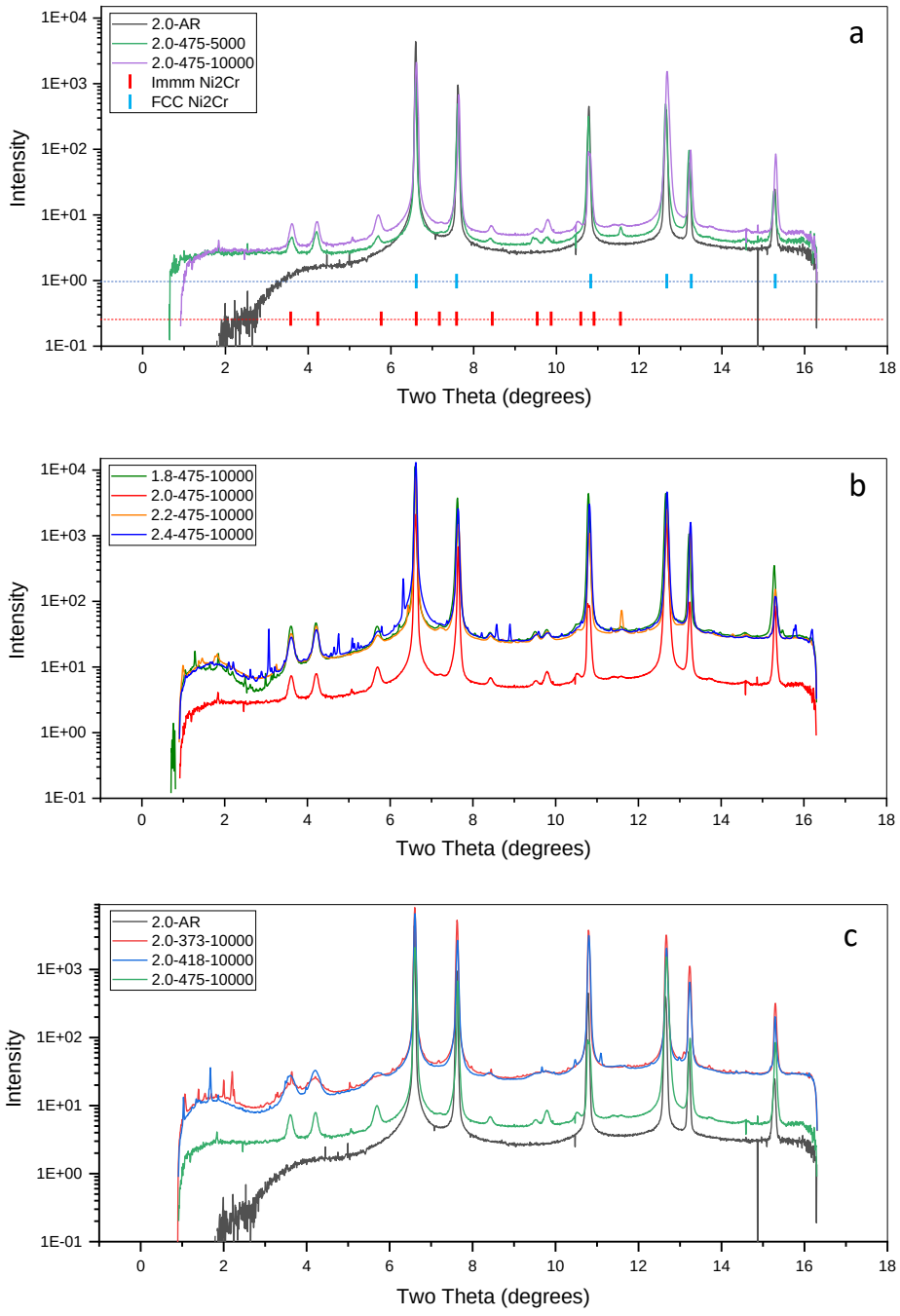

Figure 2-4. Result of synchrotron X-ray diffraction of Ni-Cr model alloys. Plot (a) indicates the evolution of ordering of Ni/Cr=2.0 alloy after aging at 475℃ for 0, 5000, and 10,000 h. Phase identification is overlaid for the FCC matrix (blue ticks) and for the orthorhombic Ni_2Cr phase (red ticks). Plot (b) indicates the evolution of ordering as a function of stoichiometry after 10,000 h ageing at 475℃. Plot (c) indicates the evolution of ordering as a function of ageing temperature on the Ni/Cr=2.0 alloy after aging 10,000 h. The peak broadening occurs as ageing temperature decreases, which indicates the changing of strain caused by ordered phase.

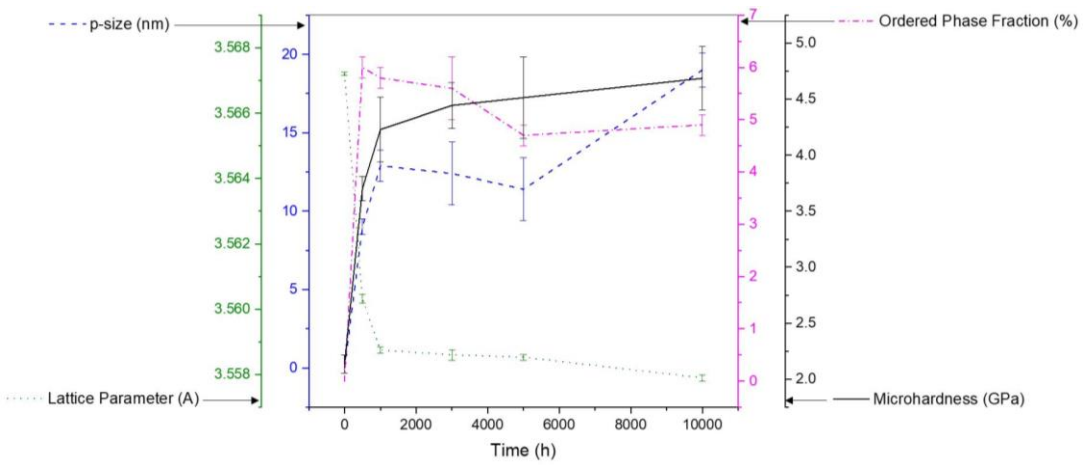

Figure 2-5. The evolution of p-size, lattice parameter, phase fraction, and microhardness as a function of ageing time. Sample and ageing condition: Ni/Cr = 2.0 samples at 475°C.

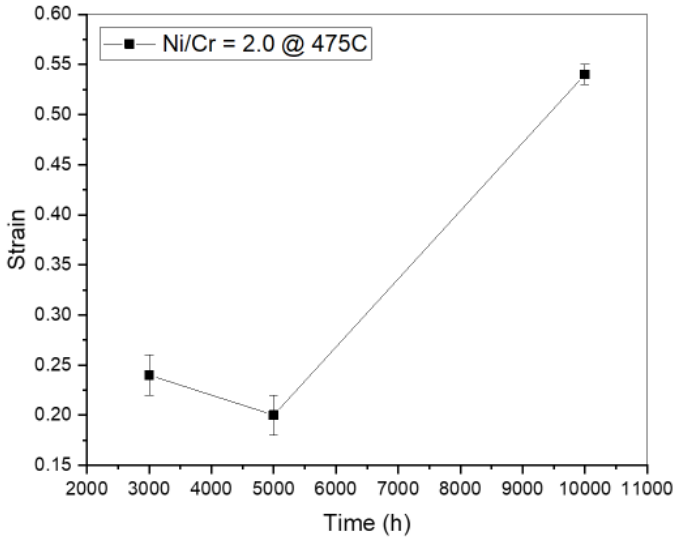

Figure 2-6. The growth of strain in sample Ni/Cr = 2.0 @ 475°C from 3000 to 5000 h. Samples were prepared by jet polishing to remove the external induced strain.

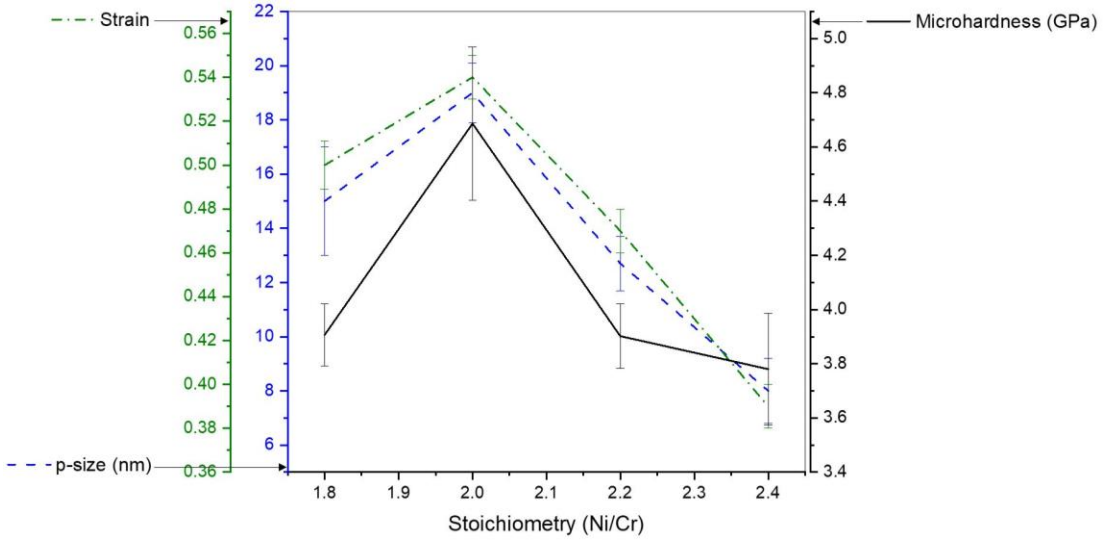

Figure 2-7. Role of stoichiometry on p-size, strain, and microhardness. Ageing condition: 10,000 h at 475°C.

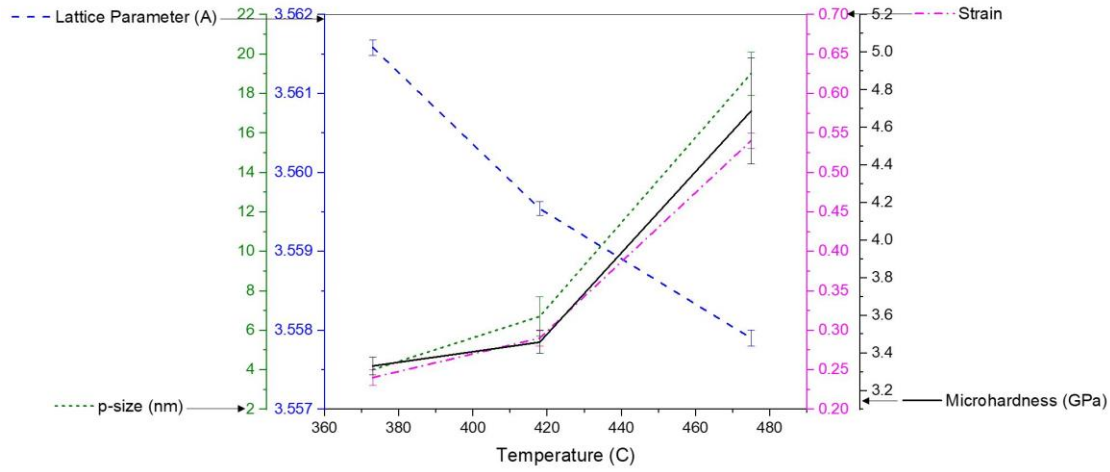

Figure 2-8. Role of temperature on lattice parameter, p-size, strain, and microhardness. Sample: Ni/Cr = 2.0. Ageing time is 10,000 h.

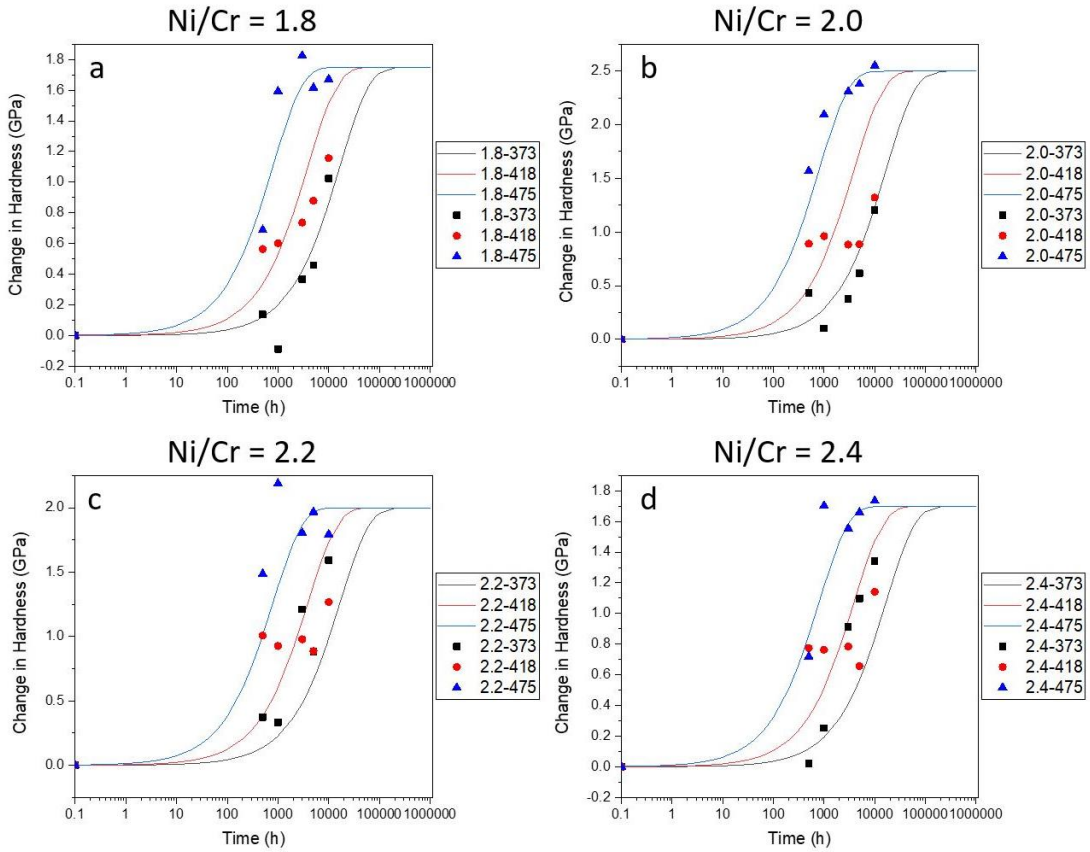

Figure 2-9. KJMA equation fitting result. (a) Ni/Cr = 1.8, (b) Ni/Cr = 2.0, (c) Ni/Cr = 2.2, (d) Ni/Cr = 2.4. Fitting parameters: k_0 = 3.00E+05 h^{-1}, Q = 120 kJ, n = 0.75.

3 Chapter 3 – Strong influence of coherent ordered precipitates relationship with fcc-matrix on deformation twinning

F. Teng [a], H. Vo [b], P. Hosemann [b, *], J. D. Tucker [a, *].

[a] Department of Mechanical Industrial Manufacturing Engineering, Oregon State University, Corvallis, OR, 97331, USA.

[b] Department of Nuclear Engineering, UC Berkeley, Berkeley, CA, USA.

3.1 Abstract

Ni_2Cr intermetallic ordered domains in Ni-based alloys lead to embrittlement through the mechanism of twinning. However, the effect of ordering domain as a function of corresponding grain orientation is still unclear. In this study, the twinning effect of the long range ordering domains has been studied by in situ micro compression testing. The results show that deformation twins only forms when the grain was compressed in [001] orientation. No twinning was observed in [111] loading orientation. The anisotropic deformation behavior is caused by the change of dislocation movement when passing from matrix face-centered cubic (fcc) structure to body-centered tetragonal (bct) precipitation. Result shows that the coincident slip systems of fcc and bct structure with the corresponding twinning system of fcc structure cause deformation twinning when the grain is loaded in [001] orientation.

3.2 Introduction

Long range ordering (LRO) transitions are observed in many types of Ni-based model and commercial alloys [53]. Considering the sluggish kinetics in commercial

alloys [25], isothermal aged Ni-Cr binary model alloys have been studied for exploring the hardening effect of LRO-Ni_2Cr structure due to the faster kinetics [33, 34, 39, 41].

The structure of LRO phase related to parent fcc matrix is shown in Figure 3-1 [55]. A previous study has shown that LRO is of $MoPt_2$ with body-centered orthorhombic (bco) unit cell ($a \neq b \neq c$) including three body-centered tetragonal (bct) cells ($a = b \neq c$) that is fully coherent with parent fcc crystal structure [55]. The twinning effect of ordered domains has been studied in previous research in Hastelloy C-22HS alloy by Lu et al. [16]. However, the role of LRO-Ni_2Cr precipitation in Ni-Cr binary system as a function of grain orientation during loading is not clear yet. In fcc structure, it is well known that $\{111\} < 11\bar{2} >$ is the twinning system (reference to fcc) [71, 72]. Figure 3-1 shows the activated twinning system (arrowed out in Figure 3-1) with corresponding slipping directions in coherent fcc/bct system. Different from fcc structure, the activated slip system of ordered bct structure is $\{01\frac{1}{\sqrt{2}}\}$ plane family (reference to bct), which is also marked out as the green plane in Figure 3-1.

It is difficult to clarify the effect on different grain orientation due to the fact that most Ni-based alloys are polycrystalline. Therefore, micro compression testing is considered to be the ideal technique to study single crystals [20]. Micro mechanical testing has been widely developed in the research of nuclear materials for understanding the mechanical behavior under irradiation, and the difference on the effects between ion-beam irradiation and neutron irradiation [15, 17, 19, 73]. Among all micro mechanical testing, micro compression testing obtains a measurement of yield strength with uniaxial loading, which makes this technique has been used on post irradiation examination [14].

In this study, the twinning effect of LRO domain on grain deforming orientation was studied by in situ micro pillar compression testing. Single crystal micro pillars were fabricated with [001] , [101] and [111] grain orientations and compressed by nanoindenter. Post compression characterization was performed by using transmission electron microscopy (TEM) to confirm the existing of twinning and slipping event.

3.3 Sample Preparation and Experimental Methods

A Ni-33at.%Cr binary model alloy was fabricated by arc-melting to mix pure Ni and Cr particles together, then the sample was hot-rolled into a plate and homogenized for 24 h at 1093°C. The sample plate was water-quenched cooling down to room temperature and sent to a third-party laboratory to perform compositional confirmation testing after homogenization. Table 6 shows the chemical composition testing result, which agrees with the designed stoichiometry. The sample plate was cut into small pieces by electrical discharge machining to minimize heat generation from cutting. One specimen was performed isothermal heat treatment at 475°C for 10,000 h. Water quenching was used to cool down the sample to room temperature. A slide of the sample with a thickness of 2 mm was cut off by low speed diamond blade from both isothermal aged specimen (2.0-475-10,000) and as-received specimen (2.0-AR). The slides were then polished on top surface and one side surface by 0.1 μm diamond suspension and 0.05 μm alumina suspension to perform a sharp edge between two perpendicular high-quality surfaces on one edge of each specimen for following EBSD characterization and pillars fabrication.

Table 6. Chemical composition (at.%) of Ni-Cr binary model alloy.

Ni	Cr	C	Fe	P	S

66.69	33.24	0.05	0.01	0.01	<0.01

For each single slide specimen, EBSD characterization was perform on the edge of the sample to find grains in [100], [101], and [111] orientation by using FEI Quanta 3D FEG duel beam SEM/FIB. Three pillars with the dimension of 2 μm × 2 μm × 4 μm were fabricated inside each grain with known grain orientation on top surface. The pillars on both 2.0-AR and 2.0-475-10,000 specimens were compressed by Hysitron PI 88 SEM Picoindenter to perform in situ micro compression testing. To confirm the LRO induced deformation behavior inside the pillar, TEM characterization was performed on compressed pillars. After the compression testing, TEM lamellas were lift out in [100] and [111] pillars on 2.0-475-10,000 aged sample in the direction that parallel to loading direction from compressed pillars by using FIB. Figure 3-2 indicates the relationship between compressing direction and TEM lamella position. Beside FIB prepared lamella, a 3 mm TEM disk was also prepared by twin jet polishing with the etchant of 90% ethanol and 10% perchloric acid at -30 °C and 20V. Both FIB prepared lamellas and jet polished disk were characterized by FEI Tecnai TF30-FEG and FEI Titan TEM.

3.4 Result

Figure 3-3 shows the SEM images of compressed pillars in all conditions. For unaged 2.0-AR pillars, all pillars in [100], [101], and [111] compressed grain orientation were failure by slipping (Figure 3-3(a) to (c)). The shear bands from one or more slip system can be observed on the surface of pillar. For the pillars on aged sample 2.0-475-10,000, change of surface contrast can be observed during compressing. The

contrast change regime can be observed in steps of initiation, growing, and merging during loading (shown in video). Twinning deformation was suspected to be observed in [100] grain orientation here. Aged [101] and [111] pillars still deformed by slipping as expected.

Figure 3-4 shows TEM characterization result for aged samples including TEM disk and FIB prepared lamellas. Figure 3-4(a) show the dark field (DF) TEM micrograph on jet polished disk of 2.0-475-10,000 specimen and corresponding selected area electron diffraction (SAED) in Figure 3-4(b). The DF image (Figure 3-4(a)) shows the distribution of LRO- Ni_2Cr precipitates in matrix. Diffraction spot for dark field imaging is circled out in yellow in SAED (Figure 3-4(b)). Figure 3-4(a) indicates that the LRO precipitates were uniformly distributed in matrix. The size of precipitation is much smaller than the dimension of micro pillar, which avoids the effect of non-uniform microstructure in the mechanical behavior of pillars. Secondary diffraction pattern in Figure 3-4(b) indicates the existing of LRO-Ni_2Cr in aged Ni-at.%33Cr binary model alloy. Figure 3-4(c) – (e) show BF and DF images of SAED Figure 3-4(f) in [011] zone axis of [100] grain orientation compressed pillar, which confirms the forming of twin during deformation in [100] compression orientation. Figure 3-4(g) is the SAED of same pillar in [001] zone axis. The result indicates the coexisting of matrix, LRO precipitates, and twin. The maximum width of twin can reach ~0.3 μm. Figure 3-4(h) – (j) shows BF and DF images of SAED in [011] zone axis of [111] grain orientation compressed pillar and Figure 3-4(k) is the corresponding SAED. The deformation behavior in 2.0-475-10,000-[111] pillar can be confirmed to be slipping only. No twinning can be observed in SAED in Figure 3-4(k). Compared

to jet polished disk, the secondary reflection of LRO in FIB prepared sample is much weaker.

3.5 Discussion

Figure 3-5 has shown the slipping system of fcc and bct system. It has been known that fcc structure is of four slip planes with three slip directions for each plane. The case for bct structure is more complicated. Systematically analysis has been performed on both [001] and [111] single crystal pillars. For performing deformation analysis of both fcc and bct structure, different referenced coordinate systems should be used when calculating the Schmid factors and the relationship of slip/twin system for fcc and bct independently, which is shown in the legend of Figure 3-5. In following text, referenced coordinate system will be mentioned as fcc- and bct- for avoiding misunderstanding when talking about slip systems.

For fcc structure deformed at [001] grain orientation, slipping and twinning system have been studied by earlier research. The fcc lattice has twelve slip systems, which all belong to the family of fcc-$\{111\} < 110 >$. The twinning system of fcc has been studied by Song et al. [72] and Kibey et al. [74], which shows that the activated twinning system is fcc-$\{111\} < 11\bar{2} >$. In bct crystal structure, the slipping systems are still unclear currently. The hypothesis used here is based on the similarity of bct structure to bcc structure. Under this hypothesis, four slip planes can be found inside each bct cubic cell and the corresponding slip systems are bct-$\{110\} < 11\sqrt{2} >$ or bct-$\{01\frac{1}{\sqrt{2}}\} < 11\sqrt{2} >$. However, the slip event may change due to the existing of ordered superlattice structure. Some slipping events will change the LRO phase, which makes them not favorable during deformation. More details will be given later.

Notice that, the slip directions of fcc-$< 110 >$ are same as that of bct-$< 11\sqrt{2} >$ at four cases shown in Figure 3-5, which are fcc-(111)/bct-$\left(01\frac{1}{\sqrt{2}}\right)$ Figure 3-5(a), fcc-$(1\bar{1}1)$ /bct- $(10\frac{1}{\sqrt{2}})$ Figure 3-5(b), fcc- $(11\bar{1})$ /bct- $(0\bar{1}\frac{1}{\sqrt{2}})$ Figure 3-5(c), and fcc-$(\bar{1}11)$/bct-$(10\frac{-1}{\sqrt{2}})$ Figure 3-5(d) when the grain is deformed at fcc-[001] orientation. However, the dislocation movement are different for the four cases. For example, in the case of fcc-(111)/bct-$(01\frac{1}{\sqrt{2}})$ (Figure 3-5(a)), slipping event occurs in fcc-$[11\bar{2}]$ orientation (solid purple arrow in Figure 3-5(a)) due to existing of anti-phase boundary of alternative layers of Ni and Cr atoms in the superlattice structure at fcc-$[\bar{1}01]$ and fcc-$[0\bar{1}1]$. Compared to the normal slipping event in fcc structure with random distribution of Ni and Cr atoms, slipping at fcc-$[\bar{1}01]$ and fcc-$[0\bar{1}1]$ orientation in bct ordered structure will brake ordered Ni_2Cr superlattice structure from ordered to disordered structure, which makes fcc-$[\bar{1}01]$ and fcc-$[0\bar{1}1]$ (which are also the bct-$[\bar{1}\bar{1}\sqrt{2}]$ and bct-$[1\bar{1}\sqrt{2}]$) slipping not favorable. Considering above reasons, slipping event fcc-$[11\bar{2}]$ (which is the bct-$[01\bar{2}]$) is preferred. To be notice that fcc-$[11\bar{2}]$ slipping event also belongs to twinning system of fcc structure. The coincident of slipping and twinning direction with the anti-phase blocking of LRO superlattice structure makes twinning occur in the case of fcc-(111)/bct-$(01\frac{1}{\sqrt{2}})$ Figure 3-5(a). Same behavior of dislocation happens in Figure 3-5(c), which is fcc-$(11\bar{1})$/bct-$(0\bar{1}\frac{1}{\sqrt{2}})$ slip plane. For the case of Figure 3-5(b) and Figure 3-5(d), which are fcc-$(1\bar{1}1)$/bct-$(10\frac{1}{\sqrt{2}})$ and fcc-$(\bar{1}11)$/bct-$(10\frac{-1}{\sqrt{2}})$ correspondingly, there is no preference between normal slipping event and fcc twinning event, because all slip directions will pass

through anti-phase boundary. For the remaining eight slip system, there is no coincident slip planes for fcc and bct structure, which means no preferences on slip direction exists during [001] grain deformation.

For fcc structure deformed at [111] grain orientation that is shown in Figure 3-6, which includes four example cases of twelve slip system. The analytical result shows that only fcc-$(1\bar{1}1)$/bct-$(10\frac{1}{\sqrt{2}})$ (Figure 3-6(d)) is of same slip plane across anti-phase boundary. The other eleven cases do not have agreement on slip planes.

3.6 Summary

The analytical result indicates that two twinning slipping systems out of twelve will be favored and activated under [001] grain deformation while no twinning slipping system will be activated under [111] grain deformation, which is supported by the observation of corresponding micro compression testing.

The deformation twinning behavior in Ni-Cr model alloy is strongly influenced by Ni_2Cr long range ordering precipitates in [001] grain orientation deformation. Due to the coincident slip system of bct structure precipitates and fcc parent matrix during [001] loading, dislocation is redirected to <112> direction family, which belongs to twinning system of fcc, due to the blocking of anti-phase barrier when the dislocation is passing through the boundary of fcc and bct.

3.7 Acknowledgements

This research is being performed using funding received from the DOE Office of Nuclear Energy's Nuclear Energy University Program, Cooperative Agreement Number DE-NE0008423. This material is also based upon work supported by the National Science Foundation under Grant No. 1653123-DMR. This work was

supported by the U.S. Department of Energy, Office of Nuclear Energy under DOE Idaho Operations Office Contract DE-AC07- 051D14517 as part of a Nuclear Science User Facilities experiment.

3.8 References

[1] M. Song, Y. Yang, M. Wang, W. Kuang, C.R. Lear, G.S. Was, Probing long-range ordering in nickel-base alloys with proton irradiation, Acta Materialia 156 (2018) 446-462.
[2] F. Delabrouille, D. Renaud, F. Vaillant, J. Massoud, Long Range Ordering of Alloy 690, 14th Intl. Conference on Environmental Degradation of Materials in Nuclear Power Systems, Virginia Beach, VA, USA, 2009.
[3] G. Young, D. Eno, Long range ordering in model Ni-Cr-X alloys, Fontevraud 8 - Contribution of Materials Investigations and Operating Experience to LWRs' Safety,Performance and Reliability, France, Avignon, 2015.
[4] L. Barnard, G. Young, B. Swoboda, S. Choudhury, A. Van der Ven, D. Morgan, J. Tucker, Atomistic modeling of the order–disorder phase transformation in the Ni 2 Cr model alloy, Acta Materialia 81 (2014) 258-271.
[5] G.A. Young, D.S. Morton, N. Lewis, R. Morris, J. Pyle, L. Barnard, R. Najafabadi, Effect of long range order on the stress corrosion susceptibility of a nickel-33 at% chromium alloy, Corrosion 72(11) (2016) 1433-1437.
[6] G.A. Young, J.D. Tucker, D.R. Eno, THE KINETICS OF LONG RANGE ORDERING IN NI-CR AND NI-CR-FE ALLOYS, (2013).
[7] B. Gwalani, T. Alam, C. Miller, T. Rojhirunsakool, Y.S. Kim, S.S. Kim, M.J. Kaufman, Y. Ren, R. Banerjee, Experimental investigation of the ordering pathway in a Ni-33 at.%Cr alloy, Acta Materialia 115 (2016) 372-384.
[8] Y. Lu, L. Pike, C. Brooks, P. Liaw, D. Klarstrom, Strengthening domains in a Ni–21Cr–17Mo alloy, Scripta materialia 56(2) (2007) 121-124.
[9] M. Jaswon, D. Dove, Twinning properties of lattice planes, Acta Crystallographica 9(8) (1956) 621-626.
[10] G.S. Song, S.H. Zhang, M. Cheng, B. Wang, Analysis on the Twinning of FCC Metals by EBSD, Advanced Materials Research, Trans Tech Publ, 2012, pp. 700-706.
[11] M.D. Uchic, D.M. Dimiduk, J.N. Florando, W.D. Nix, Sample dimensions influence strength and crystal plasticity, Science 305(5686) (2004) 986-989.
[12] G.S. Was, J.T. Busby, T. Allen, E.A. Kenik, A. Jensson, S.M. Bruemmer, J. Gan, A.D. Edwards, P.M. Scott, P.L. Andreson, Emulation of neutron irradiation effects with protons: validation of principle, Journal of Nuclear Materials 300(2) (2002) 198-216.
[13] P. Hosemann, Small-scale mechanical testing on nuclear materials: bridging the experimental length-scale gap, Scripta Materialia (2017).
[14] S. Kibey, J.B. Liu, D.D. Johnson, H. Sehitoglu, Energy pathways and directionality in deformation twinning, Applied Physics Letters 91(18) (2007) 181916.

3.9 List of Figures

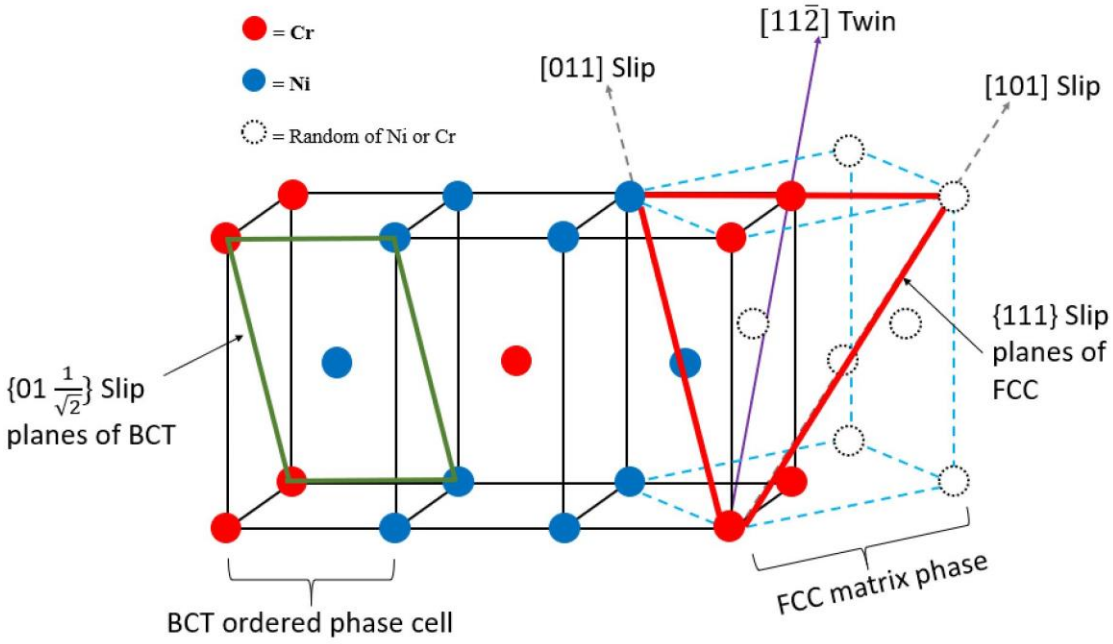

Figure 3-1. Schematics of ordered $MoPt_2$ superlattice structure (solid lines) with fcc structure (dash lines) in Ni-Cr system. Schematic of twinning direction [11$\bar{2}$] (solid line with arrow) and slipping direction [011]/[101] (dash lines with arrow) in (111) plane (triangular surface with red lines) of fcc crystal referenced to bct LRO crystal structure. Schematic of fcc/bct is after [55].

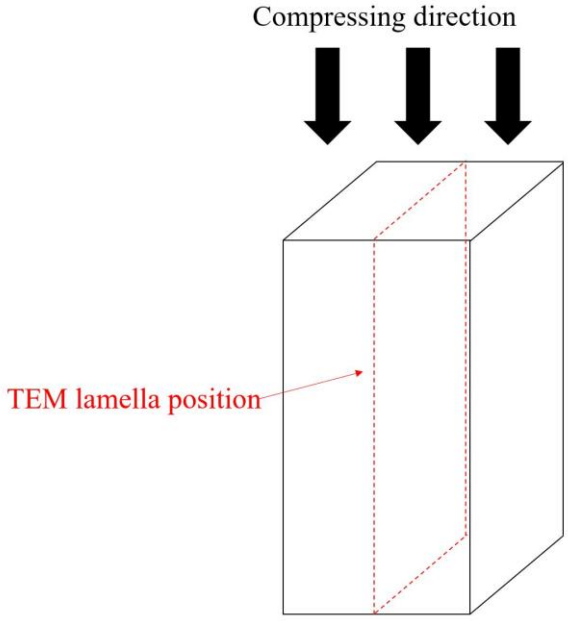

Figure 3-2. Schematics of compressing grain orientation and TEM lamella position in compressed pillar.

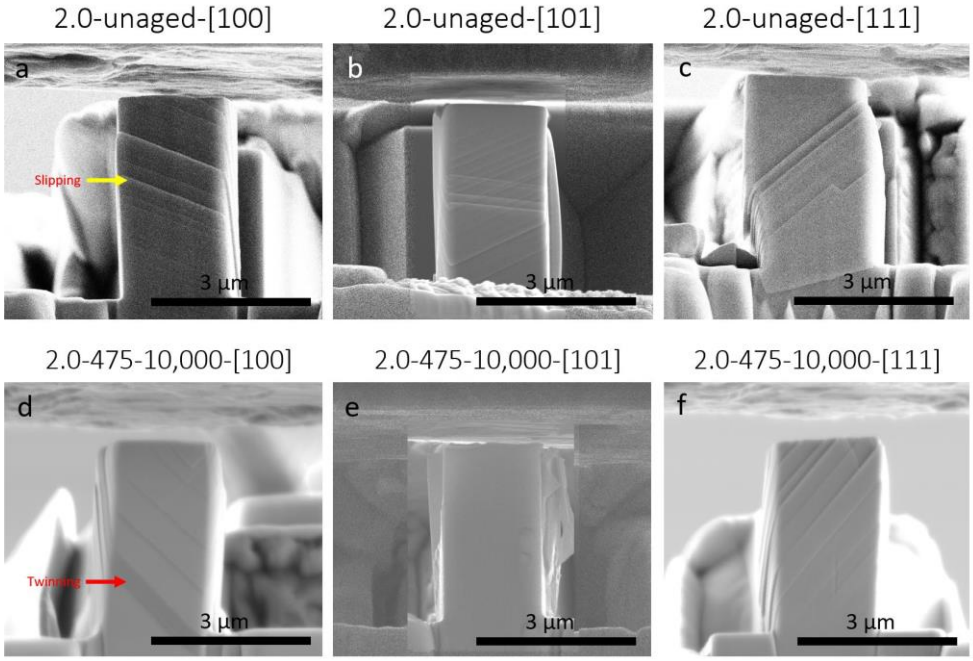

Figure 3-3. Deformation behavior of compressed pillars in all conditions: (a) 2.0-AR in [100] grain orientation. (b) 2.0-AR in [101] grain orientation. (c) 2.0-AR in [111] grain orientation. (d) 2.0-475-

10,000 aged sample in [100] grain orientation. (e) 2.0-475-10,000 aged sample in [101] grain orientation. (f) 2.0-475-10,000 aged sample in [111] grain orientation. Twinning can only be observed in 2.0-475-10,000 pillars in [100] grain orientation.

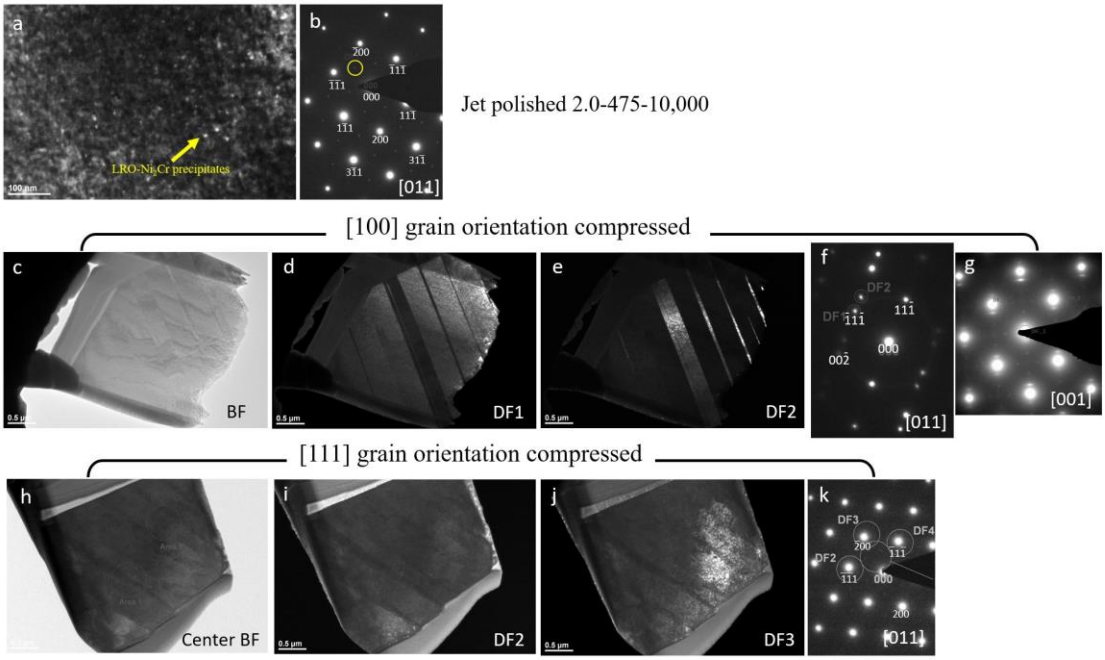

Figure 3-4. TEM characterization result: (a) DF TEM image and (b) corresponding SAED of 2.0-475-10,000 aged specimen shows the distribution of LRO- Ni_2Cr precipitates in matrix. Diffraction spot for dark field imaging is circled out in yellow in SAED. Secondary diffraction pattern indicates the existing of LRO-Ni_2Cr in aged Ni at%33Cr binary model alloy. (c) – (e) show BF and DF images of SAED (f) in [011] zone axis of [100] grain orientation compressed pillar. (g) is the SAED of same pillar in [001] zone axis. (h) – (j) shows BF and DF images of SAED in [011] zone axis of [111] grain orientation compressed pillar and (k) is the corresponding SAED. Twinning can be confirmed in 2.0-475-10,000-[100] pillar. Slipping can be confirmed in 2.0-475-10,000-[111] pillar.

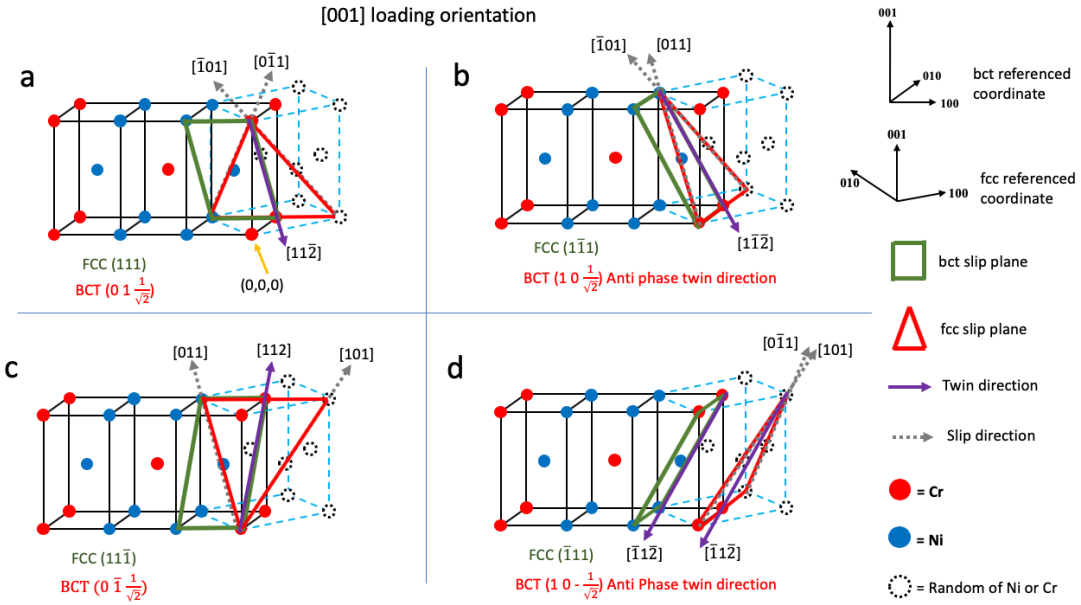

Figure 3-5. Four cases of coincident slipping systems of fcc and bct structure during [001] loading orientation. (a) fcc-(111)/bct-(01 $\frac{1}{\sqrt{2}}$), (b) fcc-(1$\bar{1}$1)/bct-(10 $\frac{1}{\sqrt{2}}$), (c) fcc-(11$\bar{1}$)/bct-(0$\bar{1}$ $\frac{1}{\sqrt{2}}$), and (d) fcc-($\bar{1}$11)/bct-(10 $\frac{-1}{\sqrt{2}}$).

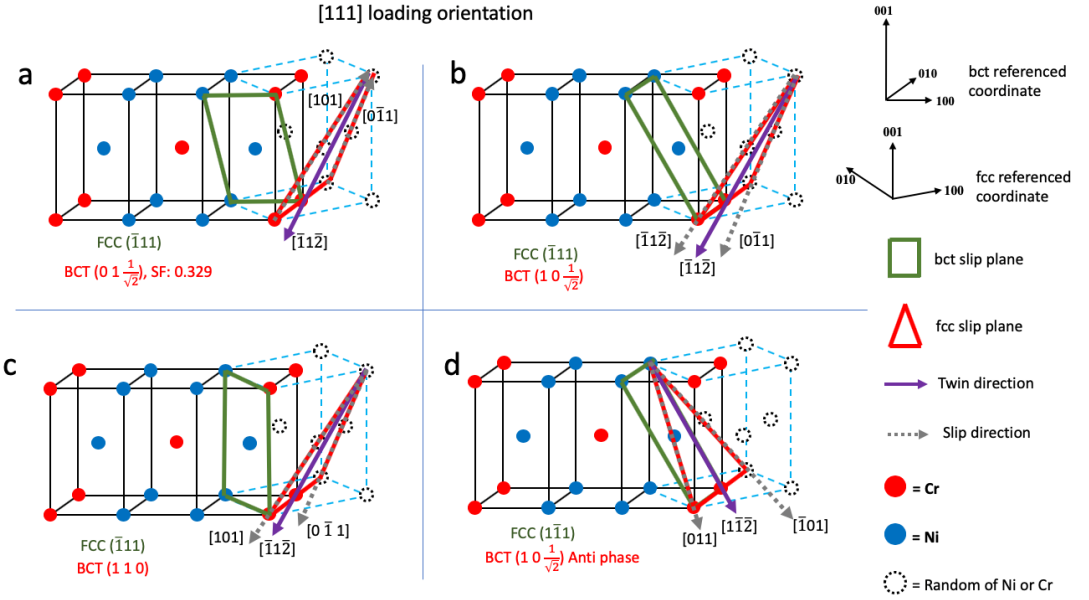

Figure 3-6. Four examples of fcc and bct slip systems of twelve during [111] loading orientation. (a) fcc-($\bar{1}$11)/bct-(01 $\frac{1}{\sqrt{2}}$), (b) fcc-($\bar{1}$11)/bct-(10 $\frac{1}{\sqrt{2}}$), (c) fcc-($\bar{1}$11)/bct-(0$\bar{1}$ $\frac{1}{\sqrt{2}}$), and (d) fcc-($\bar{1}$11)/bct-(10 $\frac{1}{\sqrt{2}}$). Only case (d) reveals same slip plane.

4 Chapter 4: Investigation of Deformation Behavior of Additive Manufactured AISI 316L Stainless Steel by In Situ Micro Compression Testing

Fei Teng [a,b], Robert C. O'Brien [a], Michael D. McMurtrey [a], Ching-Heng Shiau [a,c], Cheng Sun [a,*]

[a] Idaho National Laboratory, Idaho Falls, ID 83415, USA.

[b] Oregon State University, Corvallis, OR 97333, USA.

[c] Texas A&M University, College Station, TX 77843, USA.

* Corresponding author: Cheng.Sun@inl.gov, Phone: 208-533-7471.

4.1 Abstract

Additive manufacture techniques are being increasingly used to perform precise fabrication of engineering components with complex geometries. The heterogeneity of the additive manufactured microstructure deteriorates the mechanical integrity of the products. In this paper, we printed AISI 316L stainless steels by using additive manufacturing technique of laser metal deposition. Both single-phase and dual-phase substructures were formed in the grain interiors. The electron backscattering diffraction and energy-dispersive X-ray spectroscopy indicates that Si, Mo, S, Cr are enriched, while Fe is depleted along the substructure boundaries. In situ micro compression testing was performed at room temperature along [001] orientation. The dual-phase substructures exhibit a lower yield strength and higher Young's modulus compared to single-phase substructures. Our research provides fundamental understanding on the relationship between microstructure and mechanical properties of additive manufactured metallic materials.

Key words: Additive manufacturing, AISI 316L stainless steel, microstructure, small-scale mechanical properties

4.2 Introduction

Additive manufacturing (AM) techniques have been applied in various fields due to the low cost and near net-shape fabrication of complex components. A typical process of AM is to use laser to selectively melt the feedstock of powders and the melt powders consolidate as the geometry of the components build up layer by layer [75, 76]. Several AM methods have been developed to manufacture metallic components, such as Laser Beam Melting (LBM), Laser Metal Deposition (LMD) and Electron Beam Melting (EBM) [77]. LBM is a powder bed-based process where metal powders are spread in thin layers on the bottom of process chamber by powder recoater and laser exposes on powder bed to melt powders. This method has been used to fabricate austenitic stainless steels (SSs) [78-87], maraging SSs [88-91], precipitation hardenable SSs [92, 93], and martensitic cutlery SSs [94, 95]. LMD feeds and melts metal powders simultaneously in the deposition head, which includes laser energy inputs and coaxial/multi-jet powder feeding nozzles. AISI 316L SSs [96-98] and H13 SSs [99] have been fabricated by using this approach. Unlike LBM or EBM using laser as heating source, EBM uses electron beam to melt the metal powders with a hopper feeding the powders and a rake spreading the powders [100]. EBM has been applied to fabricated tool steels and AISI 316L SSs as well in previous research [ref].

The additive manufacturing process determines unique microstructure of AM products and thus mechanical properties. Manufacturing parameters, such as scanning method, laser power and energy distribution, play a critical role on the development of microstructure [101, 102]. AM products typically exhibit certain level of porosity due to the inherent pores trapped within powders [103]. A very low porosity of AISI 316L stainless steel, ~ 0.38%, has been reported in the literature [104]. Carlton et al. [79] studied the impact of porosity on the deformation behavior of an austenitic 316L SS and pointed out that a ductile failure mode is of a low remaining porosity (0.1%) and a brittle failure mode is usually of a high remaining porosity (2.4%). Previous study of additive manufactured 316L SS also reported the anisotropic bulk behavior related to the printing direction. Both homogenous single-phase (fcc structured austenite) and dual-phase dual-phase (fcc structured austenite and bcc structured ferrite) [105] were reported in additive manufactured AISI 316L SSs. Yadollashi et al. [96] reported that AISI 316L SS fabricated by LMD, which is Laser Engineered Net Shape (LENS), contain 9% δ-ferrite and 91% austenite, which exhibits a higher yield strength and lower elongation compared to AISI 316L SS with single austenite phase fabricated by LBM. No ferrite existing in LBM built AISI 316L SS was reported in previous research [86] while ferrite have been reported in previous study on LMD/LENS built AISI 316L SS after additive manufacture processing [96, 106]. A fundamental understanding on the formation of dual-phase microstructure and corresponding mechanical response is still unclear.

In this paper, AISI 316L SSs were fabricated through LMD approach. The printed microstructure and microchemistry were characterized and correlated to the

mechanical properties. Real-time observations of deformation failure on [001] orientation of single-phase and dual-phase structures were performed by using in-situ micro-pillar compression testing in a scanning electron microscope. Our research provides new insights on the deformation behavior of AM metallic materials and on the design of AM process for metallic materials.

4.3 Experimental Methods

AISI 316L SSs were fabricated by using Laser Engineered Net Shape (LENS) MR-7 printer, which is based on a LMD approach. The microstructure of the printed AISI 316L SS was characterized by Scanning Electron Microscopy (SEM), Electron Backscattering Diffraction (EBSD) and X-ray micro Computed Tomography (micro-CT). FEI Quanta FEG 650 SEM was used to image the grain morphology and sub-structures. The samples were polished by 1200 grit SiC paper, 1 μm diamond suspension, and 0.05 μm Alumina suspension, followed by electroetching in a solution of 15.4% nanopure water + 46.1% H_3PO_4, and 38.5% H_2SO_4 at 4V voltage at room temperature for 13s. FEI Quanta Helios Plasma Focus Ion Beam (PFIB) equipped with EBSD and X-ray Energy Dispersive Spectrum (EDS) detectors was used to map the grain orientation and chemical distribution. The samples were mechanically polished followed by plasma etching.

In-situ micro-compression tests were performed in an FEI Quanta 3D SEM. Micro-pillars with dimension of 4 μm × 4 μm × 8 μm were fabricated by using Focused Ion Beam (FIB). A flat punch tip with area of 20 μm × 20 μm was installed on a Bruker PicoIndenter-88 platform. Compression tests were performed at room temperature along [001] orientation for both single-phase and dual-phase structures. Constant

displacement rate of 40 nm/s with total displacement of 4 μm was used during the compression tests. The microstructure of compressed pillars were characterized by using JEOL 2010 transmission electron microscope.

4.4 Result

4.4.1 Microstructure and microchemistry

In the as-printed AISI 316L SS, both cellular and dendritic substructures in the interiors of grains were formed, as seen in the SEM micrographs in Figure 4-1. The average size of the cellular substructures is around 5 μm. Grain boundaries form closed to the substructure boundary (Figure 4-1(c) and Figure 4-1(d)). Orientation imaging microscopy in Figure 4-2 shows un-uniform distribution of grain size in the microstructure. Figure 4-2(a) shows the average grain size is around 100μm with single fcc structured austenite phase, while in some regions of the samples, as shown in Figure 4-2(b), the average grain size is ~ 50μm with both fcc structured austenite and bcc structured ferrite. Grain 1 and 5 in Figure 4-2(b) are homogenous fcc structured austenite, and grain 2, 3 and 4 are dual-phase duel phase structure. Pores have been observed in the as-printed AISI 316L SS by using SEM and X-ray micro-CT. In Figure 4-1(c), pores with diameter of 1-2μm are preferentially formed along the substructure boundaries. X-ray micro-CT in Figure 4-3 reveals the presence of one example of the four large pores in a pillar specimen (3.8 × 3.8 × 18.1 mm), with diameters ranging from 20 to 50 μm. Statistical study via ImageJ software shows the average pore area is 0.0543 μm^2 (average pore size is ~0.13 μm) and the porosity is less than 1%.

Chemical analysis of the as-printed AISI 316L SS has been performed by using EDS. Figure 4-4 shows the chemical distribution in a region with single-phase

structures, the same region was examined for both OIM and chemical mapping. The dash lines represent the grain boundaries. Chemical mapping shows Si, Mo, S, Cr, and Ni are enriched and Fe is depleted along the substructure boundary, no clear evidence of chemical segregation was observed along the grain boundaries. Figure 4-5 shows the chemical distribution of a region with dual-phase structures. Elements with enrichment in fcc structured austenite are Si, S, Cr, Co, Ni, and Mo. Figure 4-6 shows the co-existence of fcc structured austenite and bcc structured ferrite in dual-phase structures. Bcc structured ferritic grains in Figure 6a contains multiple sub-grains with high-angle sub-grain boundaries, as seen in Figure 6c. Chemical segregation is also related to phase separation in the as-printed AISI 316L SS. EDS chemical mapping of the same area of Figure 4-6 is shown in Figure 4-7. Result indicates that Fe is enriched in bcc structured ferrite and other elements including Cr, Ni, C, Mn, Mo, S, Si are enriched in fcc structured austenite.

4.4.2 In-situ micro-compression tests

In-situ micro-compression tests were performed in both single-phase and dual-phase structures along [001] orientation at room temperature. Figure 4-8 shows the snapshots of the micro-pillar compression tests at strain levels up to 21%. Slip band is typically identified as narrow lines without any contrast while twin exhibits contrast compared to the matrix as it propagates [107]. The snapshots suggest that deformation of single-phase structures is mainly through slip, while twinning is the dominate deformation mechanism in dual-phase structures. TEM micrographs in Figure 4-8(i)-(j) confirm that both slip bands and twins are formed in single-phase and dual-phase structure, but the twin spacing in deformed single-phase structures is ~44 nm, which is

smaller than that in the deformed dual-phase structures, ~ 395 nm. The true stress-strain curves and corresponding strain hardening rate as a function of strain are shown in Figure 4-9. The yield strength of single-phase structures is measured to be ~464 MPa, and ~384 MPa for dual-phase structures. The measured Young's modulus is ~21 GPa for single-phase structures and ~38 GPa for dual-phase structures. Two clear load drops were observed during the compression of dual-phase structures, corresponding to the formation of deformation twins. The plot of strain hardening rate vs strain indicates twinning-induced straining hardening in dual-phase structures starts when the true strain is greater than 12%.

4.5 Discussion

4.5.1 Microstructure evolution in as-printed AM316L

The thermal cycle in the local areas during EBM can generate metastable microstructure and non-uniform chemical distributions [108, 109]. The size of sub-structure (~5 μm) observed in LMD AM316L is much smaller than the grain size (~70 μm). Compared to the particle size of powder used for printing (~40 μm), the size of sub-structure is much smaller than either grain size or powder particle size. The cellular or dendritic sub-structure is usually attributed increased cooling rate and the corresponding non-equilibrium solidification in SLM method from previous research [110]. The size of sub-structure is determined by energy input effect including preheating temperature and scanning speed. Specifically, cell spacing decreases with increase of laser scanning speed and decrease of preheating temperature [111]. The formation of the cellular sub-structure requires a minimized cooling rate. The concentration of solute in the liquid usually will be minimized and combined with an

extremely high velocity of the solidification in front place [112]. However, the solidification process has been studied in Al-12Si system [113] shows that the solidifying front rejects solute back into liquid under a high cooling rate, which increase solute concertation as solidification going. At the same time, the solubility is decreasing as temperature going down, which makes elements segregate on the boundary of solidification. In the case of AM, the high cooling rate process is spread to whole structure with much higher volume resolution than casting. Due to the combination of high cooling rate and the changing solubility, cellular structure is favored in kinetics [113]. The residual solute will be segregated along boundaries of cellular sub-structure. Very similar process happens here in AM316L and that explains the enrichment of solutes elements (Si, Mo, S, Cr, Ni, C, Mn, and Co) and depletion of Fe in continuous phase.

By combining the process of solidification, the evolution of microstructure in LMD-processed AM316L can be roughly described by. i) The material cools down from liquid phase with a rapid rate with elements segregation at the boundary of cellular sub-structure. ii) Center of some cellular and dendritic structure is depleted in C during cooling, which makes the structure pass through $\alpha + \gamma$ regime and eutectic point in phase diagram. The segregation of solutes between solidification core (dendritic or cellular) and surrounding (continuous) leads to the phase separation in dual-phase microstructure. For the area that is not of phase separation, solutes segregation is not strong enough to guide the solidification process into $\alpha + \gamma$ phase region, which makes the microstructure shows segregation but not phase separation.

4.5.2 Effect of dual-phase structures on deformation behavior in additive manufactured 316L

By using the contrast change of the micro-pillars during compression tests, dislocation movement via slip is the major deformation mode of the single-phase sing-phase structure, while in the dual-phase structure, deformation twinning is the dominate deformation mechanism. The two clear load drops are attributed to the formation of twins as indicated in the TEM micrographs. The stress-strain plots of micro compression testing (Figure 4-9(a)) reveal the different deformation behavior of two pillars in detail. The behavior is analyzed in elastic and plastic regimes, which includes the 1st and 2nd load drop in plastic regimes of two pillars. In elastic regime, the hardening effect of pillar hetero-[001] is higher than that of homo-[001] due to the existing of dual-phase grain boundary barrier for dislocation movement. With the compressing going through yielding point, twinning forms in pillar hetero-[001] and the slip event from the formation of twinning induced load drop can be observed by in situ compression, which has been arrowed out in the stress-strain plot of Figure 4-9(a).

In the review article by Meyers et al. [114], twinning is of two effect on the evolution of plastic deformation: 1. Twinning contributes to plastic deformation by twinning shear, and twinning induces decreasing work hardening rate. This has been found in Cu alloys by Vo¨hringer et al. [115]. 2. The grains were subdivided by twin grain, which increases the barriers to slip and the corresponding work hardening rate. This has been demonstrated by Mulford and Kocks [116], and successfully modeled by Asgari et al. [117] and El-Danaf et al. [118]. Both effects of twinning can be observed in hetero-[001] pillar compared to homo-[001] from their strain hardening-strain plots

in Figure 4-9(b): in twinning slipping period (strain = 0.037 to 0.07), the strain hardening of pillar hetero-[001] is lower than that of pillar homo-[001] as twin grains nucleation. When twinning formation is finished, the twin hardening effect starts showing out (strain > 0.14).

It is well known that stress concentration is required to initiate the nucleation of twinning, which is considered to be the critical event in the formation of twinning. Based on previous review article about twinning from Meyers et al. [114], the local stress required to initiate twinning is significantly higher than external traction induced single-phase stress, which means the existing of "defect" in single-phase structure is required to concentrate single-phase stress into a local position. In AM316L, the dual-phase structure obtains the "defect". Twinning forms easier at the early stage of plastic regime due to the low stacking fault energy of 316L stainless steel, which is 12.9 mJ/m^2 from the previous research of Ojima et al. [119]. However, the single crystal pillar homo-[001] does not obtain enough local stress to initiate twinning. For pillar hetero-[001], dual-phase structure induced stress concentration that large enough to start twinning.

4.6 Conclusion

AISI 316L SSs have been fabricated through laser metal deposition technique. Both single-phase (fcc structured austenite) and dual-phase (bcc structured ferrite and fcc structured austenite) structures were developed due to the non-uniform cooling rate during the manufacturing process. Substructures were formed within the grain interiors with enrichment of Si, Mo, S, Cr, and Ni and depletion of Fe along the substructure

boundaries. The dual-phase structures exhibit an increased Young's modulus and decreased yield strength. Twinning is the dominant deformation mechanism of dual-phase structures at room temperature. Our study provides new insights on the relationship between microstructure and mechanical properties of additive manufactured metallic materials.

4.7 Acknowledgements

The work was supported through the INL Laboratory Directed Research& Development (LDRD) Program under DOE Idaho Operations Office Contract DE-AC07-05ID14517. We also acknowledge the U.S. Department of Energy, Office of Nuclear Energy under DOE Idaho Operation Office Contract DE-AC07-051D14517 as part of a Nuclear Science User Facility (NSUF) experiment.

4.8 References

[1] B.E. Carroll, T.A. Palmer, A.M. Beese, Anisotropic tensile behavior of Ti–6Al–4V components fabricated with directed energy deposition additive manufacturing, Acta Materialia 87 (2015) 309-320.
[2] E. Brandl, F. Palm, V. Michailov, B. Viehweger, C. Leyens, Mechanical properties of additive manufactured titanium (Ti–6Al–4V) blocks deposited by a solid-state laser and wire, Materials & Design 32(10) (2011) 4665-4675.
[3] D. Herzog, V. Seyda, E. Wycisk, C. Emmelmann, Additive manufacturing of metals, Acta Materialia 117 (2016) 371-392.
[4] M. Badrossamay, T. Childs, Further studies in selective laser melting of stainless and tool steel powders, International Journal of Machine Tools and Manufacture 47(5) (2007) 779-784.
[5] H.D. Carlton, A. Haboub, G.F. Gallegos, D.Y. Parkinson, A.A. MacDowell, Damage evolution and failure mechanisms in additively manufactured stainless steel, Materials Science and Engineering: A 651 (2016) 406-414.
[6] S. Dadbakhsh, L. Hao, N. Sewell, Effect of selective laser melting layout on the quality of stainless steel parts, Rapid Prototyping Journal 18(3) (2012) 241-249.
[7] P. Jerrard, L. Hao, K. Evans, Experimental investigation into selective laser melting of austenitic and martensitic stainless steel powder mixtures, Proceedings of the Institution of Mechanical Engineers, Part B: Journal of Engineering Manufacture 223(11) (2009) 1409-1416.

[8] R. Li, J. Liu, Y. Shi, M. Du, Z. Xie, 316L stainless steel with gradient porosity fabricated by selective laser melting, Journal of Materials Engineering and Performance 19(5) (2010) 666-671.
[9] R. Li, Y. Shi, L. Wang, J. Liu, Z. Wang, The key metallurgical features of selective laser melting of stainless steel powder for building metallic part, Powder Metallurgy and Metal Ceramics 50(3-4) (2011) 141.
[10] T. Niendorf, S. Leuders, A. Riemer, H.A. Richard, T. Tröster, D. Schwarze, Highly anisotropic steel processed by selective laser melting, Metallurgical and materials transactions B 44(4) (2013) 794-796.
[11] A. Riemer, S. Leuders, M. Thöne, H. Richard, T. Tröster, T. Niendorf, On the fatigue crack growth behavior in 316L stainless steel manufactured by selective laser melting, Engineering Fracture Mechanics 120 (2014) 15-25.
[12] B. Song, X. Zhao, S. Li, C. Han, Q. Wei, S. Wen, J. Liu, Y. Shi, Differences in microstructure and properties between selective laser melting and traditional manufacturing for fabrication of metal parts: A review, Frontiers of Mechanical Engineering 10(2) (2015) 111-125.
[13] I. Tolosa, F. Garciandía, F. Zubiri, F. Zapirain, A. Esnaola, Study of mechanical properties of AISI 316 stainless steel processed by "selective laser melting", following different manufacturing strategies, The International Journal of Advanced Manufacturing Technology 51(5-8) (2010) 639-647.
[14] K. Kempen, E. Yasa, L. Thijs, J.P. Kruth, J. Van Humbeeck, Microstructure and mechanical properties of Selective Laser Melted 18Ni-300 steel, Physics Procedia 12 (2011) 255-263.
[15] E.A. Jägle, P.-P. Choi, J. Van Humbeeck, D. Raabe, Precipitation and austenite reversion behavior of a maraging steel produced by selective laser melting, Journal of Materials Research 29(17) (2014) 2072-2079.
[16] G. Casalino, S. Campanelli, N. Contuzzi, A. Ludovico, Experimental investigation and statistical optimisation of the selective laser melting process of a maraging steel, Optics & Laser Technology 65 (2015) 151-158.
[17] T. Burkert, A. Fischer, The effects of heat balance on the void formation within marage 300 processed by selective laser melting, Proc of SFF Symposium, 2015, pp. 745-757.
[18] T.L. Starr, K. Rafi, B. Stucker, C.M. Scherzer, Controlling phase composition in selective laser melted stainless steels, Power (W) 195 (2012) 195.
[19] L.E. Murr, E. Martinez, J. Hernandez, S. Collins, K.N. Amato, S.M. Gaytan, P.W. Shindo, Microstructures and properties of 17-4 PH stainless steel fabricated by selective laser melting, Journal of Materials Research and Technology 1(3) (2012) 167-177.
[20] P. Krakhmalev, I. Yadroitsava, G. Fredriksson, I. Yadroitsev, In situ heat treatment in selective laser melted martensitic AISI 420 stainless steels, Materials & Design 87 (2015) 380-385.
[21] X. Zhao, B. Song, Y. Zhang, X. Zhu, Q. Wei, Y. Shi, Decarburization of stainless steel during selective laser melting and its influence on Young's modulus, hardness and tensile strength, Materials Science and Engineering: A 647 (2015) 58-61.
[22] A. Yadollahi, N. Shamsaei, S.M. Thompson, D.W. Seely, Effects of process time interval and heat treatment on the mechanical and microstructural properties of direct

laser deposited 316L stainless steel, Materials Science and Engineering: A 644 (2015) 171-183.
[23] J.D. Majumdar, A. Pinkerton, Z. Liu, I. Manna, L. Li, Microstructure characterisation and process optimization of laser assisted rapid fabrication of 316L stainless steel, Applied Surface Science 247(1-4) (2005) 320-327.
[24] K. Mahmood, A.J. Pinkerton, Direct laser deposition with different types of 316L steel particle: a comparative study of final part properties, Proceedings of the Institution of Mechanical Engineers, Part B: Journal of Engineering Manufacture 227(4) (2013) 520-531.
[25] J. Mazumder, J. Choi, K. Nagarathnam, J. Koch, D. Hetzner, The direct metal deposition of H13 tool steel for 3-D components, Jom 49(5) (1997) 55-60.
[26] L.E. Murr, S.M. Gaytan, A. Ceylan, E. Martinez, J.L. Martinez, D.H. Hernandez, B.I. Machado, D.A. Ramirez, F. Medina, S. Collins, R.B. Wicker, Characterization of titanium aluminide alloy components fabricated by additive manufacturing using electron beam melting, Acta Materialia 58(5) (2010) 1887-1894.
[27] J.P. Kruth, L. Froyen, J. Van Vaerenbergh, P. Mercelis, M. Rombouts, B. Lauwers, Selective laser melting of iron-based powder, Journal of Materials Processing Technology 149(1-3) (2004) 616-622.
[28] E. Liverani, S. Toschi, L. Ceschini, A. Fortunato, Effect of selective laser melting (SLM) process parameters on microstructure and mechanical properties of 316L austenitic stainless steel, Journal of Materials Processing Technology 249 (2017) 255-263.
[29] J.-P. Kruth, M. Badrossamay, E. Yasa, J. Deckers, L. Thijs, J. Van Humbeeck, Part and material properties in selective laser melting of metals, Proceedings of the 16th international symposium on electromachining, 2010.
[30] J. Cherry, H. Davies, S. Mehmood, N. Lavery, S. Brown, J. Sienz, Investigation into the effect of process parameters on microstructural and physical properties of 316L stainless steel parts by selective laser melting, The International Journal of Advanced Manufacturing Technology 76(5-8) (2015) 869-879.
[31] P. Guo, B. Zou, C. Huang, H. Gao, Study on microstructure, mechanical properties and machinability of efficiently additive manufactured AISI 316L stainless steel by high-power direct laser deposition, Journal of Materials Processing Technology 240 (2017) 12-22.
[32] M. Ziętala, T. Durejko, M. Polański, I. Kunce, T. Płociński, W. Zieliński, M. Łazińska, W. Stępniowski, T. Czujko, K.J. Kurzydłowski, Z. Bojar, The microstructure, mechanical properties and corrosion resistance of 316L stainless steel fabricated using laser engineered net shaping, Materials Science and Engineering: A 677 (2016) 1-10.
[33] J.X. Zou, K.M. Zhang, T. Grosdidier, C. Dong, Y. Qin, S.Z. Hao, D.Z. Yang, Orientation-dependent deformation on 316L stainless steel induced by high-current pulsed electron beam irradiation, Materials Science and Engineering: A 483-484 (2008) 302-305.
[34] L. Thijs, F. Verhaeghe, T. Craeghs, J.V. Humbeeck, J.-P. Kruth, A study of the microstructural evolution during selective laser melting of Ti–6Al–4V, Acta Materialia 58(9) (2010) 3303-3312.

[35] X. Tan, Y. Kok, Y.J. Tan, M. Descoins, D. Mangelinck, S.B. Tor, K.F. Leong, C.K. Chua, Graded microstructure and mechanical properties of additive manufactured Ti–6Al–4V via electron beam melting, Acta Materialia 97 (2015) 1-16.
[36] D. Wang, C. Song, Y. Yang, Y. Bai, Investigation of crystal growth mechanism during selective laser melting and mechanical property characterization of 316L stainless steel parts, Materials & Design 100 (2016) 291-299.
[37] I. Yadroitsev, P. Krakhmalev, I. Yadroitsava, S. Johansson, I. Smurov, Energy input effect on morphology and microstructure of selective laser melting single track from metallic powder, Journal of Materials Processing Technology 213(4) (2013) 606-613.
[38] S. Kou, Welding metallurgy, New Jersey, USA (2003) 431-446.
[39] K.G. Prashanth, S. Scudino, H.J. Klauss, K.B. Surreddi, L. Löber, Z. Wang, A.K. Chaubey, U. Kühn, J. Eckert, Microstructure and mechanical properties of Al–12Si produced by selective laser melting: Effect of heat treatment, Materials Science and Engineering: A 590 (2014) 153-160.
[40] M.A. Meyers, O. Vöhringer, V.A. Lubarda, The onset of twinning in metals: a constitutive description, Acta Materialia 49(19) (2001) 4025-4039.
[41] O. Vöhringer, Einsatzspannung für die Bildung von Verformungszwillingen bei vielkristallinen α-Kupferlegierungen, Zeitschrift für Naturforschung A 24(3) (1969) 478-478.
[42] R. Mulford, U. Kocks, New observations on the mechanisms of dynamic strain aging and of jerky flow, Acta Metallurgica 27(7) (1979) 1125-1134.
[43] S. Asgari, E. El-Danaf, S.R. Kalidindi, R.D. Doherty, Strain hardening regimes and microstructural evolution during large strain compression of low stacking fault energy fcc alloys that form deformation twins, Metallurgical and Materials Transactions A 28(9) (1997) 1781-1795.
[44] E. El-Danaf, S.R. Kalidindi, R.D. Doherty, Influence of grain size and stacking-fault energy on deformation twinning in fcc metals, Metallurgical and Materials Transactions A 30(5) (1999) 1223-1233.
[45] M. Ojima, Y. Adachi, Y. Tomota, Y. Katada, Y. Kaneko, K. Kuroda, H. Saka, Weak beam TEM study on stacking fault energy of high nitrogen steels, steel research international 80(7) (2009) 477-481.

4.9 List of Figures

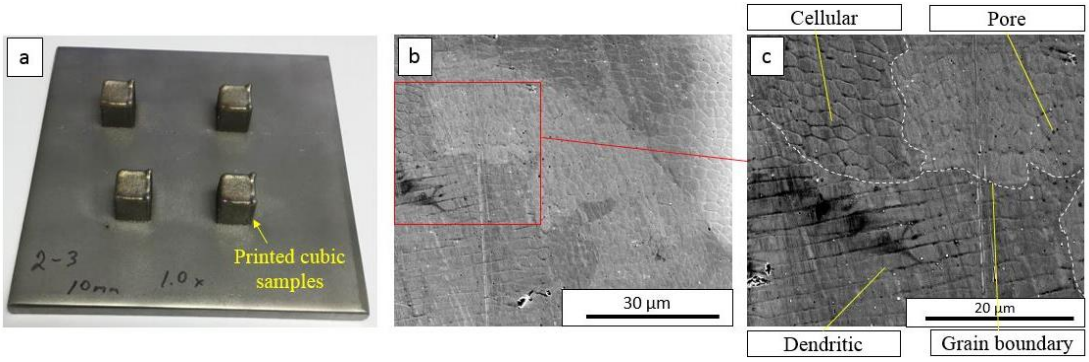

Figure 4-1. Sketch indicates the printing orientation for additive manufacture 316SS used in the study. Micro-structure of AM316L. Images show grain boundary and the existing of two types of substructure (cell and dendrite) and pores.

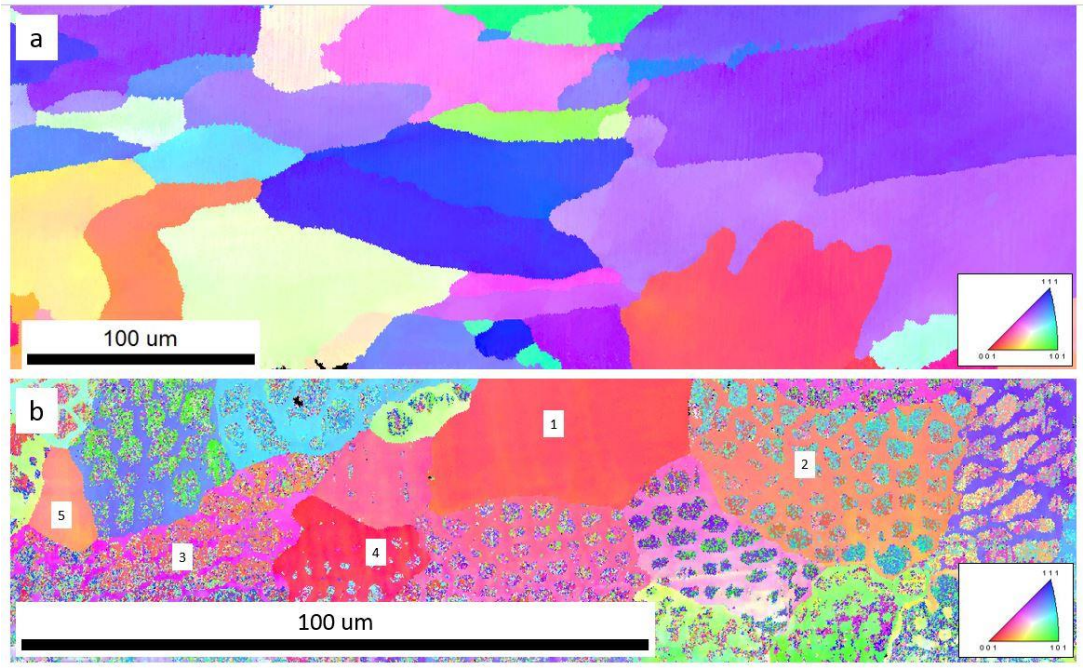

Figure 4-2. OIM of additive manufactured AISI 316L SS by EBSD.(a) fcc structured single-phase microstructure. The average grain size is ~ 100 µm. (b) dual-phase microstructure with fcc structure austenite and bcc structured ferrite. The average grain size if ~ 50µm.

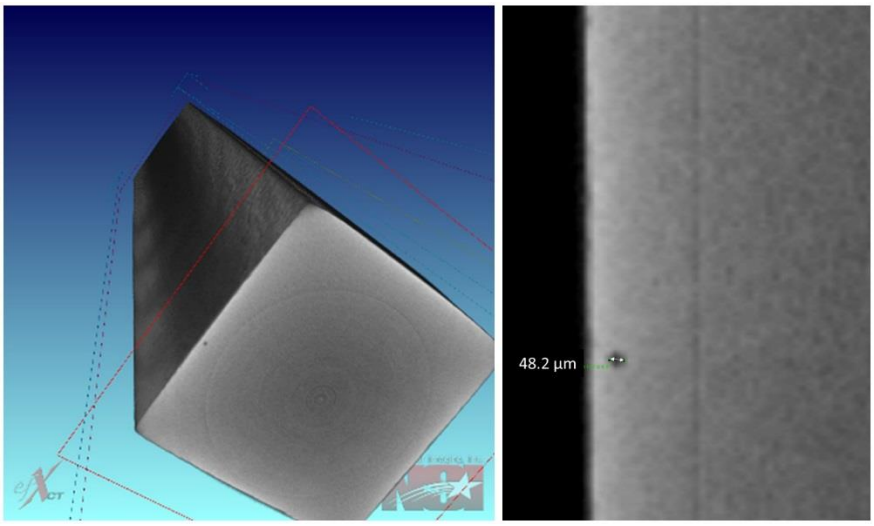

Figure 4-3. X-ray micro-CT characterization of pores in the as-printed AISI 316L SS. One large pore with diameter of ~ 48µm is shown.

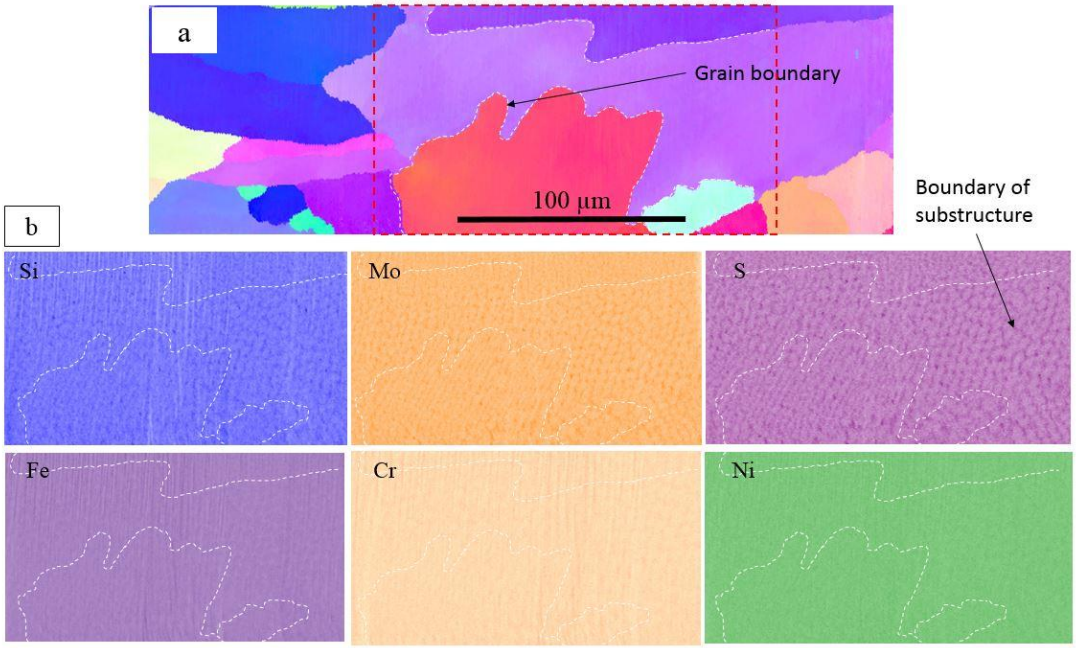

Figure 4-4. Chemical analysis of homogenous structures in the as-printed AISI 316L SS. Grain boundary and substructure boundary were labeled. Si, Mo, S, Cr and Ni are enriched, while Fe is depleted along the substructure boundary.

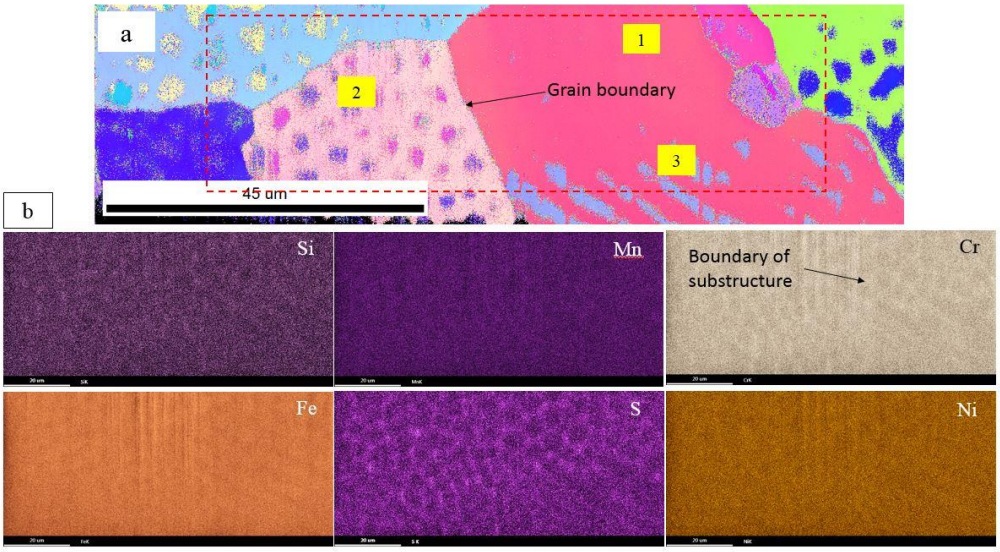

Figure 4-5. Chemical analysis of dual-phase structures in the as-printed AISI 316L SS. Grain boundary, substructure boundary and phase boundary were labeled. Si, Mn, S, Cr and Ni are enriched, while Fe is depleted along the substructure boundary.

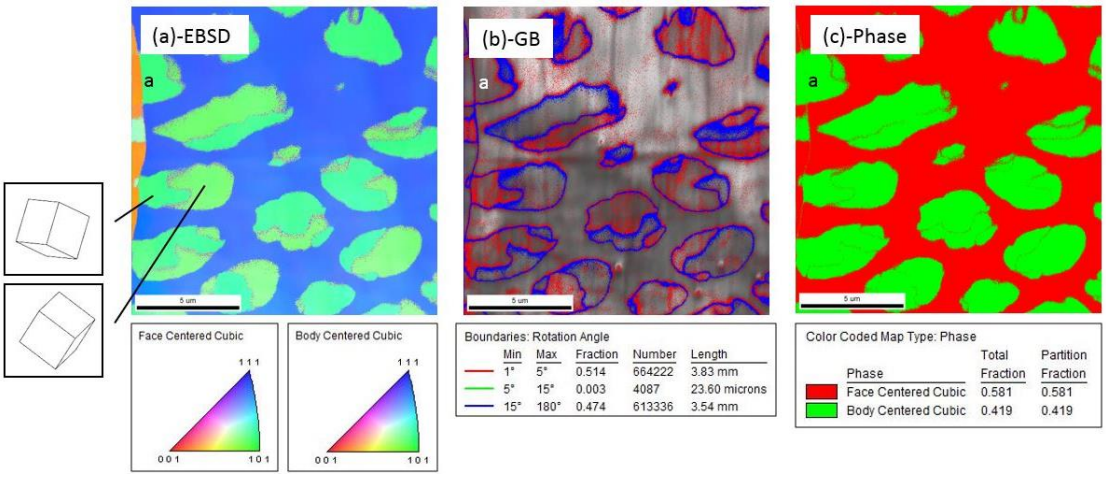

Figure 4-6. (a) Orientation imaging microscopy (OIM) of dual-phase structures. (b) Grain misorientation angle distribution. (c) Phase identification of dual-phase structures. FCC structured austenite and BCC structured ferrite were observed.

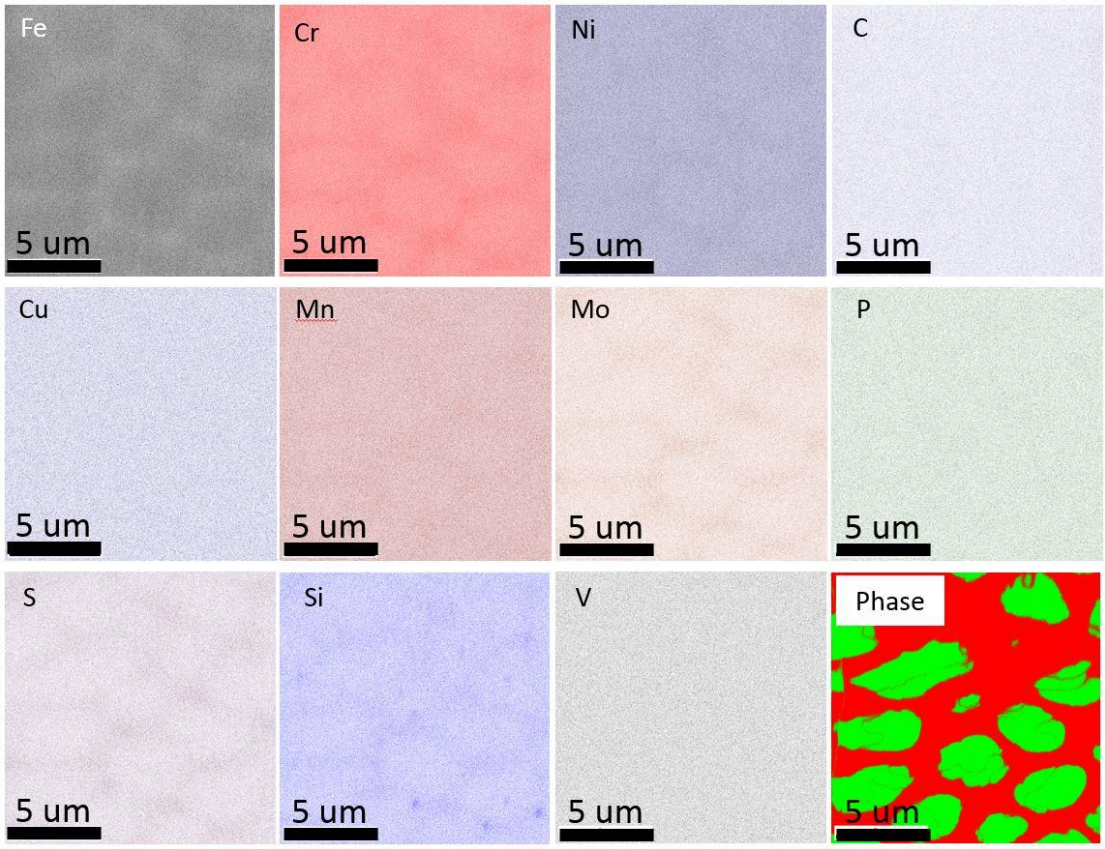

Figure 4-7. Chemical partitioning in dual-phase structures. EDS map reveals that: Si, Mo, S, Cr, and Ni are enriched and Fe is depleted in austenite phase. Si, Mo, S, Cr, and Ni are depleted and Fe is enriched in ferrite phase.

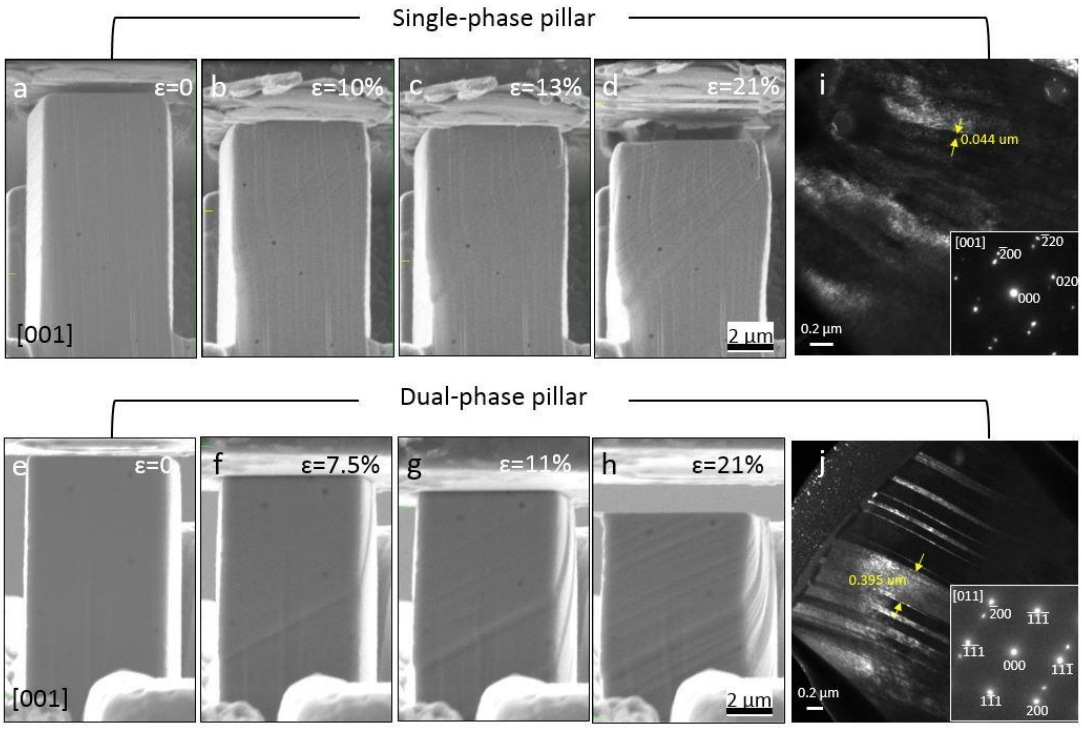

Figure 4-8. In-situ SEM micro-compression of homogenous and dual-phase structures along [001] orientation at room temperature. (a-d) snapshots of compression tests of single-phase structure at strain of 0, 10%, 13% and 21%. (e-h) snapshots of compression tests of dual-phase structure at strain of 1%, 7.5%, 11% and 21%. (i, j) TEM micrographs of compressed pillars showing the formation of deformation twins.

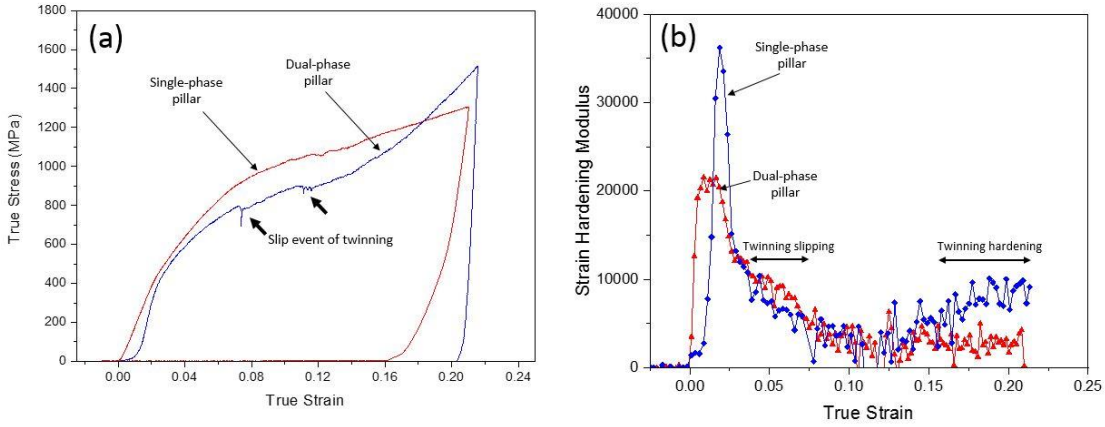

Figure 4-9. (a) True strain-stress curves of single-phase structures (red) vs dual-phase structures (blue) of additive manufactured AISI 316L SS along [001] orientation. The yield strength is ~464 MPa for single-phase structures and ~384 MPa for dual-phase structures, and the Young's modulus is ~21 GPa and ~38 GPa for single-phase structures and dual-phase structures, respectively. Two clear load drops were observed in the dual-phase structure. (b) Strain hardening rate of single-phase structures and dual-phase structures as a function of true strain. . The strain hardening induced by deformation twinning was observed in dual-phase structures when true strain is greater than 0.12.

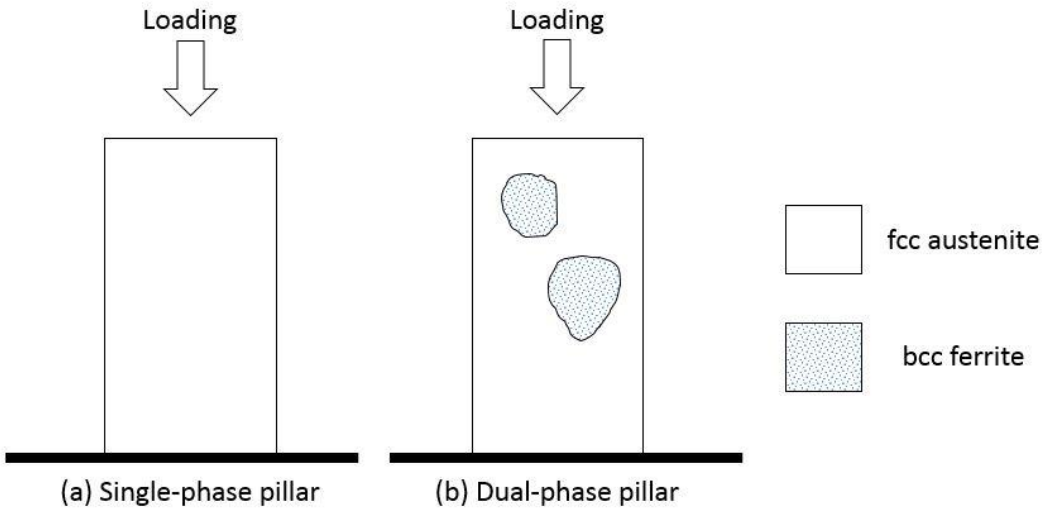

Figure 4-10. Sketch indicates the distribution of phase in micro pillars. (a) Single-phase pillars. (b) Dual-phase pillars.

5 Chapter 5 – General Conclusion

The thermal degradation of structural materials including Ni-Cr binary model alloys and additively manufactured 316L stainless steel have been studied by a variety of materials characterization techniques including microstructure characterization and micro-scale mechanical testing in this study. The objectives of this work were to 1) Discover the role of stoichiometry on the degradation of Ni-Cr model alloys. Specifically, the evolution of long range ordering (LRO) and hardening as a function of stoichiometry is addressed. 2) Discover the role of LRO domain on the deformation mode under different loading orientation in single grain in Ni-Cr binary model alloys in [001] grain orientation. 3) Characterize the microstructure and deformation behavior in new AM316L alloy. For AM316L, systematically microstructure characterization was performed as additive manufacturing is new in advanced manufacture field and the microstructure and corresponding effects on mechanical properties in conventional material are almost unknown.

For the Ni-Cr model alloys, isothermal heat treatment was performed at 373°C, 418°C, and 475°C from 500 to 10,000 h. The formation of LRO domains was observed by the isothermal ageing. The evolution of ordered domains was characterized by TEM, microhardness, and XRD. The effect of ordered domains on the deformation behavior was studied by in situ micro compression testing, followed by TEM inspection on compressed pillars.

Result suggests that LRO phase is wider than previously known on Ni-Cr phase diagram. However, more study needs to be done to confirm the result in longer heat

treatment. The rate of ordering is similar for all stoichiometry, but the maximum amount of LRO is different.

Results show that stoichiometry plays a dominated role on the formation of ordered domains: model alloys reveals a larger degree of ordering when the stoichiometry is closest to Ni/Cr = 2.0. Larger deviation from 2.0 causes lower degree of ordering. Lattice parameter, size of coherent ordered particles, and microhardness reach saturation after 1000 hours at 475°C. The ordered phase fraction reaches saturation earlier than other parameters and slowly decreases with ageing.

The deformation behavior is influenced by ordered domains in Ni-Cr alloys. In [001] grain orientation, the deformation type is changed from slipping to twinning by ordered domain. [101] and [111] grain orientations are not influenced by ordering. The grains still fail by slipping.

For additively manufactured 316L stainless steel, thermally-induced heterogeneous substructure and porosity have been studied by both microstructure characterization, which includes EBSD/EDS and X-ray computer tomography, and *in situ* micro-compression testing followed by post compression characterization by TEM. Result shows that:

Both homogeneous and heterogeneous substructure were observed in microstructure due to the rapid cooling rate during printing.

Heterogeneous substructure changes the deformation behavior from slipping to twinning when the grain is loaded at [001] grain orientation.

In summary, the thermal degradation of Ni-Cr alloys and AM316L stainless steel in nuclear applications significantly changes the mechanical properties. The study of

AM316L stainless steel points out the direction for future research on additive manufactured steel. Considering the special microstructure generated by the new manufacturing technique, new microstructure on conventional materials with different mechanical properties will be possible for the future research on materials science. Commercial Ni-based alloys, such as 690, fall within the range of the stoichiometry studied and should be evaluated for long-term thermal degradation for reactor applications.

6 Future work

Micro-mechanical testing is being utilized more and more in nuclear materials research. However, the size effect of micro-mechanical testing, which makes the difference between micro mechanical and macro mechanical properties, limits the application of the technique in research. To fill the gap between micro and macro mechanical testing, the size effect as function of material properties, dimension of specimen, and irradiation should be clarified further.

For Ni-based alloys, the embrittlement effect of long range ordering is significant on changing both mechanical properties and deformation behavior. Future research needs to focus on the role of irradiation with thermal effect on the evolution of ordering phase transformation. Also, more research needs to be done on the formation and the effect of LRO in Ni-based commercial alloys under real nuclear utilized environment. Finally, a model, based on experimental data, can be built to predict the lifetime of commercial alloys to better evaluate the degradation of the components in nuclear power plant.

For additively manufactured 316L stainless steel, more research is needed on the role of non-uniform microstructure and the corresponding irradiation effect on mechanical properties. Moreover, the manufactured technique and post processing should be improved to homogenize the microstructure.

7 Bibliography

S. Chu, A. Majumdar, Opportunities and challenges for a sustainable energy future, Nature 488 (2012) 294.

Nuclear Power in the World Today. 2018).

J. Cobb, Highlights of the World Nuclear Performance Report 2018, INFORUM VERLAGS-VERWALTUNGSGESELLSCHAFT MBH ATW-ADVERTISING-SUBSCRIPTIONS, ROBERT-KOCH-PLATZ 4, BERLIN, 10115, GERMANY, 2018.

World Energy Outlook 2017, World Energy Outlook 2017, 2017.

V.S. Arunachalam, E.L. Fleischer, The Global Energy Landscape and Materials Innovation, MRS Bulletin 33(4) (2011) 264-288.

World List of Nuclear Power Plants, Nucler News, 2012, p. 55.

P.M.S. Jones, Nuclear reactor types, John Wiley and Sons, United Kingdom, 1987.

Nuclear Reactor Types, Kirk-Othmer Encyclopedia of Chemical Technology.

L.J. Bond, T.T. Taylor, S.R. Doctor, A.B. Hull, S.N. Malik, Proactive Management of Materials Degradation for nuclear power plant systems, 2008 International Conference on Prognostics and Health Management, 2008, pp. 1-9.

S.J. Zinkle, G.S. Was, Materials challenges in nuclear energy, Acta Materialia 61(3) (2013) 735-758.

S. Zinkle, N. Ghoniem, Operating temperature windows for fusion reactor structural materials, Fusion Engineering and design 51 (2000) 55-71.

G.S.W. S. Teysseyre, 13th International conference on degradation of materials in nuclear power systems – water reactors, Canadian Nuclear Society, Whistler, British Columbia, Toronto, 2007.

S.J. Zinkle, J.T. Busby, Structural materials for fission & fusion energy, Materials Today 12(11) (2009) 12-19.

P. Hosemann, Small-scale mechanical testing on nuclear materials: bridging the experimental length-scale gap, Scripta Materialia (2017).

G.S. Was, J.T. Busby, T. Allen, E.A. Kenik, A. Jensson, S.M. Bruemmer, J. Gan, A.D. Edwards, P.M. Scott, P.L. Andreson, Emulation of neutron irradiation effects with protons: validation of principle, Journal of Nuclear Materials 300(2) (2002) 198-216.

Y. Lu, L. Pike, C. Brooks, P. Liaw, D. Klarstrom, Strengthening domains in a Ni–21Cr–17Mo alloy, Scripta materialia 56(2) (2007) 121-124.

A. Reichardt, A. Lupinacci, D. Frazer, N. Bailey, H. Vo, C. Howard, Z. Jiao, A.M. Minor, P. Chou, P. Hosemann, Nanoindentation and in situ microcompression in different dose regimes of proton beam irradiated 304 SS, Journal of Nuclear Materials 486 (2017) 323-331.

D. Kiener, P. Hosemann, S.A. Maloy, A.M. Minor, In situ nanocompression testing of irradiated copper, Nature Materials 10 (2011) 608.

C.P. Frick, B.G. Clark, S. Orso, A.S. Schneider, E. Arzt, Size effect on strength and strain hardening of small-scale [1 1 1] nickel compression pillars, Materials Science and Engineering: A 489(1–2) (2008) 319-329.
M.D. Uchic, D.M. Dimiduk, J.N. Florando, W.D. Nix, Sample dimensions influence strength and crystal plasticity, Science 305(5686) (2004) 986-989.
[21] T. Allen, J. Busby, M. Meyer, D. Petti, Materials challenges for nuclear systems, Materials today 13(12) (2010) 14-23.
[22] T. Chester, S. Norman, C. William, Superalloys II, Eds. John Willey & Sons, Inc., New York (1976).
[23] K. Chiang, D. Dunn, G. Cragnolino, Effect of simulated groundwater chemistry on stress corrosion cracking of alloy 22, Corrosion 63(10) (2007) 940-950.
[24] E.O. Ezugwu, Z.M. Wang, A.R. Machado, The machinability of nickel-based alloys: a review, Journal of Materials Processing Technology 86(1) (1999) 1-16.
[25] F. Delabrouille, D. Renaud, F. Vaillant, J. Massoud, Long Range Ordering of Alloy 690, 14th Intl. Conference on Environmental Degradation of Materials in Nuclear Power Systems, Virginia Beach, VA, USA, 2009.
[26] W. Xiong, Thermodynamic and kinetic investigation of the Fe-Cr-Ni system driven by engineering applications, Department of Materials Science and Engineering, KTH Royal Institute of Technology, School of Industrial Engineering and Management, 2012.
A. Marucco, Phase transformations during long-term ageing of Ni Fe Cr alloys in the temperature range 450–600° C, Materials Science and Engineering: A 194(2) (1995) 225-233.
A. Marucco, Effects of composition on the order-disorder transformation in ni-cr based alloys, Key Engineering Materials, Trans Tech Publ, 1991, pp. 77-90.
A. Marucco, B. Nath, Effects of Ordering on the Properties of Ni-Cr Alloys, Journal of Materials Science 23(6) (1988) 2107-2114.
S. Lee, P. Nash, Phase diagrams of binary nickel alloys, ASM International, Materials Park (OH) (1991) 133.
X. Xie, Y. Zeng, L. Kou, J. Dong, L. Pike, D. Klarstrom, THE PRECIPITATION AND STRENGTHENING BEHAVIOR OF Ni2 (Mo, Cr) IN HASTELLOY® C-22HS® ALLOY, A NEWLY DEVELOPED HIGH MOLYBDENUM NI-BASE SUPERALLOY, (2008).
H.M. Tawancy, M.O. Aboelfotoh, High strength and high ductility in a nanoscale superlattice of Ni2(Cr,Mo) deformable by twinning, Scripta Materialia 59(8) (2008) 846-849.
G.A. Young, D.S. Morton, N. Lewis, R. Morris, J. Pyle, L. Barnard, R. Najafabadi, Effect of long range order on the stress corrosion susceptibility of a nickel-33 at% chromium alloy, Corrosion 72(11) (2016) 1433-1437.
G. Young, D. Eno, Long range ordering in model Ni-Cr-X alloys, Fontevraud 8 - Contribution of Materials Investigations and Operating Experience to LWRs' Safety,Performance and Reliability, France, Avignon, 2015.
E. Metcalfe, B. Nath, A. Wickens, Some effects of the ordering transformation in Nimonic 80A on stress relaxation behaviour, Materials Science and Engineering 67(2) (1984) 157-162.

K. Miyata, M. Igarashi, Effect of ordering on susceptibility to hydrogen embrittlement of a Ni-base superalloy, Metallurgical Transactions A 23(3) (1992) 953-961.

F. Teng, J.D. Tucker, Role of Stoichiometry on Ordering in Ni-Cr Alloys, MRS Online Proceedings Library Archive 1809 (2015) 7-12.

F. Teng, L.-J. Yu, O. Ciuca, E. Marquis, G. Burke, J.D. Tucker, The Role of Stoichiometry on Ordering Phase Transformations in Ni–Cr Alloys for Nuclear Applications, Environmental Degradation of Materials in Nuclear Power Systems, Springer, 2017, pp. 251-259.

L. Barnard, G. Young, B. Swoboda, S. Choudhury, A. Van der Ven, D. Morgan, J. Tucker, Atomistic modeling of the order–disorder phase transformation in the Ni 2 Cr model alloy, Acta Materialia 81 (2014) 258-271.

J.D. Tucker, R. Najafabadi, T.R. Allen, D. Morgan, Ab initio-based diffusion theory and tracer diffusion in Ni–Cr and Ni–Fe alloys, Journal of Nuclear Materials 405(3) (2010) 216-234.

G.A. Young, J.D. Tucker, D.R. Eno, THE KINETICS OF LONG RANGE ORDERING IN NI-CR AND NI-CR-FE ALLOYS, (2013).

J. Buršík, M. Svoboda, The existence of P phase and Ni2Cr superstructure in Ni-Al-Cr-Mo system, Scripta Materialia 39(8) (1998) 1107-1112.

M. Hirabayashi, M. Koiwa, K. Tanaka, T. Tadaki, T. Saburi, S. Nenno, H. Nishiyama, An experimental study on the ordered alloy Ni2Cr, Transactions of the Japan Institute of Metals 10(5) (1969) 365-371.

V. Kolotushkin, V. Kondrat'ev, A. Laushkin, V. Rechitskii, Effect of long-term aging on the structural and phase stability and properties of nickel-chromium alloys, Metal science and heat treatment 45(11) (2003) 411-414.

L. Guttman, Order-Disorder Phenomena in Metals, in: S. Frederick, T. David (Eds.), Solid State Physics, Academic Press1956, pp. 145-223.

A. Marucco, Atomic ordering and α′-Cr phase precipitation in long-term aged Ni3Cr and Ni2Cr alloys, Journal of materials science 30(16) (1995) 4188-4194.

A. Marucco, Atomic ordering in the Ni Cr Fe system, Materials Science and Engineering: A 189(1) (1994) 267-276.

L. Karmazin, Lattice parameter studies of structure changes of Ni□ Cr alloys in the region of Ni2Cr, Materials Science and Engineering 54(2) (1982) 247-256.

E. Frely, B. Beuneu, A. Barbu, G. Jaskierowicz, Investigation of ordering kinetics in Ni-Cr-Fe alloys under electron irradiation, Annales De Physique (1997).

E. Frely, B. Beuneu, A. Barbu, G. Jaskierowicz, Short and Long-Range Ordering of (Ni 0.67 Cr 0.33) 1-x Fe x Alloys Under Electron Irradiation, MRS Proceedings, Cambridge Univ Press, 1996, p. 373.

A. Arya, G.K. Dey, V.K. Vasudevan, S. Banerjee, Effect of chromium addition on the ordering behaviour of Ni–Mo alloy: experimental results vs. electronic structure calculations, Acta Materialia 50(13) (2002) 3301-3315.

L. Karmazin, J. Krejčí, J. Zeman, γ Phase and Ni2Cr-type long-range order in Ni-rich NiCrMo alloys, Materials Science and Engineering: A 183(1-2) (1994) 103-109.

M. Song, Y. Yang, M. Wang, W. Kuang, C.R. Lear, G.S. Was, Probing long-range ordering in nickel-base alloys with proton irradiation, Acta Materialia 156 (2018) 446-462.

P.S. Pao, S.J. Gill, C.R. Feng, D.J. Michel, Fatigue and fracture of a Ni2Cr ordered intermetallic alloy, Materials Science and Engineering: A 153(1) (1992) 532-537.
B. Gwalani, T. Alam, C. Miller, T. Rojhirunsakool, Y.S. Kim, S.S. Kim, M.J. Kaufman, Y. Ren, R. Banerjee, Experimental investigation of the ordering pathway in a Ni-33 at.%Cr alloy, Acta Materialia 115 (2016) 372-384.
A. Verma, J.B. Singh, N. Wanderka, J.K. Chakravartty, Delineating the roles of Cr and Mo during ordering transformations in stoichiometric Ni2(Cr1−x,Mox) alloys, Acta Materialia 96 (2015) 366-377.
C. Pareige, F. Soisson, G. Martin, D. Blavette, Ordering and phase separation in Ni–Cr–Al: Monte Carlo simulations vs three-dimensional atom probe, Acta Materialia 47(6) (1999) 1889-1899.
S. Meher, P. Nandwana, T. Rojhirunsakool, J. Tiley, R. Banerjee, Probing the crystallography of ordered Phases by coupling of orientation microscopy with atom probe tomography, Ultramicroscopy 148 (2015) 67-74.
M. Sundararaman, L. Kumar, G.E. Prasad, P. Mukhopadhyay, S. Banerjee, Precipitation of an intermetallic phase with Pt 2 Mo-type structure in alloy 625, Metallurgical and Materials Transactions A 30(1) (1999) 41-52.
X. Shi, S. Ghose, E. Dooryhee, Performance calculations of the X-ray powder diffraction beamline at NSLS-II, Journal of synchrotron radiation 20(2) (2013) 234-242.
D.J. Sprouster, R. Weidner, S. Ghose, E. Dooryhee, T. Novakowski, T. Stan, P. Wells, N. Almirall, G. Odette, L. Ecker, Infrastructure development for radioactive materials at the NSLS-II, Nuclear Instruments and Methods in Physics Research Section A: Accelerators, Spectrometers, Detectors and Associated Equipment 880 (2018) 40-45.
H.C. Pai, M. Sundararaman, B.C. Maji, A. Biswas, M. Krishnan, Influence of Mo addition on the solvus temperature of Ni2(Cr,Mo) phase in Ni2(Cr,Mo) alloys, Journal of Alloys and Compounds 491(1-2) (2010) 159-164.
R. Hu, G.M. Cheng, J.Q. Zhang, J.S. Li, T.B. Zhang, H.Z. Fu, First principles investigation on the stability and elastic properties of Ni2Cr1−xMx (M = Nb, Mo, Ta, and W) superlattices, Intermetallics 33 (2013) 60-66.
C.T. Sims, N.S. Stoloff, W.C. Hagel, superalloys II, Wiley New York1987.
B.J. Berkowitz, C. Miller, The effect of ordering on the hydrogen embrittlement susceptibility of Ni2Cr, Metallurgical Transactions A 11(11) (1980) 1877-1881.
A.N. Kolmogorov, On the statistical theory of the crystallization of metals, Bull. Acad. Sci. USSR, Math. Ser 1 (1937) 355-359.
M. Avrami, Kinetics of phase change. III. Granulation, phase change, and microstructure, J. chem. Phys 9(2) (1941) 177-184.
M. Avrami, Kinetics of phase change. II transformation-time relations for random distribution of nuclei, The Journal of Chemical Physics 8(2) (1940) 212-224.
M. Avrami, Kinetics of phase change. I General theory, The Journal of chemical physics 7(12) (1939) 1103-1112.
W.A. Johnson, R.F. Mehl, Reaction kinetics in processes of nucleation and growth, Trans. Aime 135(8) (1939) 396-415.
M. Jaswon, D. Dove, Twinning properties of lattice planes, Acta Crystallographica 9(8) (1956) 621-626.

G.S. Song, S.H. Zhang, M. Cheng, B. Wang, Analysis on the Twinning of FCC Metals by EBSD, Advanced Materials Research, Trans Tech Publ, 2012, pp. 700-706.
H. Vo, A. Reichardt, C. Howard, M.D. Abad, D. Kaoumi, P. Chou, P. Hosemann, Small-Scale Mechanical Testing on Proton Beam-Irradiated 304 SS from Room Temperature to Reactor Operation Temperature, Jom 67(12) (2015) 2959-2964.
S. Kibey, J.B. Liu, D.D. Johnson, H. Sehitoglu, Energy pathways and directionality in deformation twinning, Applied Physics Letters 91(18) (2007) 181916.
B.E. Carroll, T.A. Palmer, A.M. Beese, Anisotropic tensile behavior of Ti–6Al–4V components fabricated with directed energy deposition additive manufacturing, Acta Materialia 87 (2015) 309-320.
E. Brandl, F. Palm, V. Michailov, B. Viehweger, C. Leyens, Mechanical properties of additive manufactured titanium (Ti–6Al–4V) blocks deposited by a solid-state laser and wire, Materials & Design 32(10) (2011) 4665-4675.
D. Herzog, V. Seyda, E. Wycisk, C. Emmelmann, Additive manufacturing of metals, Acta Materialia 117 (2016) 371-392.
M. Badrossamay, T. Childs, Further studies in selective laser melting of stainless and tool steel powders, International Journal of Machine Tools and Manufacture 47(5) (2007) 779-784.
H.D. Carlton, A. Haboub, G.F. Gallegos, D.Y. Parkinson, A.A. MacDowell, Damage evolution and failure mechanisms in additively manufactured stainless steel, Materials Science and Engineering: A 651 (2016) 406-414.
S. Dadbakhsh, L. Hao, N. Sewell, Effect of selective laser melting layout on the quality of stainless steel parts, Rapid Prototyping Journal 18(3) (2012) 241-249.
P. Jerrard, L. Hao, K. Evans, Experimental investigation into selective laser melting of austenitic and martensitic stainless steel powder mixtures, Proceedings of the Institution of Mechanical Engineers, Part B: Journal of Engineering Manufacture 223(11) (2009) 1409-1416.
R. Li, J. Liu, Y. Shi, M. Du, Z. Xie, 316L stainless steel with gradient porosity fabricated by selective laser melting, Journal of Materials Engineering and Performance 19(5) (2010) 666-671.
R. Li, Y. Shi, L. Wang, J. Liu, Z. Wang, The key metallurgical features of selective laser melting of stainless steel powder for building metallic part, Powder Metallurgy and Metal Ceramics 50(3-4) (2011) 141.
T. Niendorf, S. Leuders, A. Riemer, H.A. Richard, T. Tröster, D. Schwarze, Highly anisotropic steel processed by selective laser melting, Metallurgical and materials transactions B 44(4) (2013) 794-796.
A. Riemer, S. Leuders, M. Thöne, H. Richard, T. Tröster, T. Niendorf, On the fatigue crack growth behavior in 316L stainless steel manufactured by selective laser melting, Engineering Fracture Mechanics 120 (2014) 15-25.
B. Song, X. Zhao, S. Li, C. Han, Q. Wei, S. Wen, J. Liu, Y. Shi, Differences in microstructure and properties between selective laser melting and traditional manufacturing for fabrication of metal parts: A review, Frontiers of Mechanical Engineering 10(2) (2015) 111-125.
I. Tolosa, F. Garciandía, F. Zubiri, F. Zapirain, A. Esnaola, Study of mechanical properties of AISI 316 stainless steel processed by “selective laser melting”,

following different manufacturing strategies, The International Journal of Advanced Manufacturing Technology 51(5-8) (2010) 639-647.
K. Kempen, E. Yasa, L. Thijs, J.P. Kruth, J. Van Humbeeck, Microstructure and mechanical properties of Selective Laser Melted 18Ni-300 steel, Physics Procedia 12 (2011) 255-263.
E.A. Jägle, P.-P. Choi, J. Van Humbeeck, D. Raabe, Precipitation and austenite reversion behavior of a maraging steel produced by selective laser melting, Journal of Materials Research 29(17) (2014) 2072-2079.
G. Casalino, S. Campanelli, N. Contuzzi, A. Ludovico, Experimental investigation and statistical optimisation of the selective laser melting process of a maraging steel, Optics & Laser Technology 65 (2015) 151-158.
T. Burkert, A. Fischer, The effects of heat balance on the void formation within marage 300 processed by selective laser melting, Proc of SFF Symposium, 2015, pp. 745-757.
T.L. Starr, K. Rafi, B. Stucker, C.M. Scherzer, Controlling phase composition in selective laser melted stainless steels, Power (W) 195 (2012) 195.
L.E. Murr, E. Martinez, J. Hernandez, S. Collins, K.N. Amato, S.M. Gaytan, P.W. Shindo, Microstructures and properties of 17-4 PH stainless steel fabricated by selective laser melting, Journal of Materials Research and Technology 1(3) (2012) 167-177.
P. Krakhmalev, I. Yadroitsava, G. Fredriksson, I. Yadroitsev, In situ heat treatment in selective laser melted martensitic AISI 420 stainless steels, Materials & Design 87 (2015) 380-385.
X. Zhao, B. Song, Y. Zhang, X. Zhu, Q. Wei, Y. Shi, Decarburization of stainless steel during selective laser melting and its influence on Young's modulus, hardness and tensile strength, Materials Science and Engineering: A 647 (2015) 58-61.
A. Yadollahi, N. Shamsaei, S.M. Thompson, D.W. Seely, Effects of process time interval and heat treatment on the mechanical and microstructural properties of direct laser deposited 316L stainless steel, Materials Science and Engineering: A 644 (2015) 171-183.
J.D. Majumdar, A. Pinkerton, Z. Liu, I. Manna, L. Li, Microstructure characterisation and process optimization of laser assisted rapid fabrication of 316L stainless steel, Applied Surface Science 247(1-4) (2005) 320-327.
K. Mahmood, A.J. Pinkerton, Direct laser deposition with different types of 316L steel particle: a comparative study of final part properties, Proceedings of the Institution of Mechanical Engineers, Part B: Journal of Engineering Manufacture 227(4) (2013) 520-531.
J. Mazumder, J. Choi, K. Nagarathnam, J. Koch, D. Hetzner, The direct metal deposition of H13 tool steel for 3-D components, Jom 49(5) (1997) 55-60.
L.E. Murr, S.M. Gaytan, A. Ceylan, E. Martinez, J.L. Martinez, D.H. Hernandez, B.I. Machado, D.A. Ramirez, F. Medina, S. Collins, R.B. Wicker, Characterization of titanium aluminide alloy components fabricated by additive manufacturing using electron beam melting, Acta Materialia 58(5) (2010) 1887-1894.
J.P. Kruth, L. Froyen, J. Van Vaerenbergh, P. Mercelis, M. Rombouts, B. Lauwers, Selective laser melting of iron-based powder, Journal of Materials Processing Technology 149(1-3) (2004) 616-622.

E. Liverani, S. Toschi, L. Ceschini, A. Fortunato, Effect of selective laser melting (SLM) process parameters on microstructure and mechanical properties of 316L austenitic stainless steel, Journal of Materials Processing Technology 249 (2017) 255-263.

J.-P. Kruth, M. Badrossamay, E. Yasa, J. Deckers, L. Thijs, J. Van Humbeeck, Part and material properties in selective laser melting of metals, Proceedings of the 16th international symposium on electromachining, 2010.

J. Cherry, H. Davies, S. Mehmood, N. Lavery, S. Brown, J. Sienz, Investigation into the effect of process parameters on microstructural and physical properties of 316L stainless steel parts by selective laser melting, The International Journal of Advanced Manufacturing Technology 76(5-8) (2015) 869-879.

P. Guo, B. Zou, C. Huang, H. Gao, Study on microstructure, mechanical properties and machinability of efficiently additive manufactured AISI 316L stainless steel by high-power direct laser deposition, Journal of Materials Processing Technology 240 (2017) 12-22.

M. Ziętala, T. Durejko, M. Polański, I. Kunce, T. Płociński, W. Zieliński, M. Łazińska, W. Stępniowski, T. Czujko, K.J. Kurzydłowski, Z. Bojar, The microstructure, mechanical properties and corrosion resistance of 316L stainless steel fabricated using laser engineered net shaping, Materials Science and Engineering: A 677 (2016) 1-10.

J.X. Zou, K.M. Zhang, T. Grosdidier, C. Dong, Y. Qin, S.Z. Hao, D.Z. Yang, Orientation-dependent deformation on 316L stainless steel induced by high-current pulsed electron beam irradiation, Materials Science and Engineering: A 483-484 (2008) 302-305.

L. Thijs, F. Verhaeghe, T. Craeghs, J.V. Humbeeck, J.-P. Kruth, A study of the microstructural evolution during selective laser melting of Ti–6Al–4V, Acta Materialia 58(9) (2010) 3303-3312.

X. Tan, Y. Kok, Y.J. Tan, M. Descoins, D. Mangelinck, S.B. Tor, K.F. Leong, C.K. Chua, Graded microstructure and mechanical properties of additive manufactured Ti–6Al–4V via electron beam melting, Acta Materialia 97 (2015) 1-16.

D. Wang, C. Song, Y. Yang, Y. Bai, Investigation of crystal growth mechanism during selective laser melting and mechanical property characterization of 316L stainless steel parts, Materials & Design 100 (2016) 291-299.

I. Yadroitsev, P. Krakhmalev, I. Yadroitsava, S. Johansson, I. Smurov, Energy input effect on morphology and microstructure of selective laser melting single track from metallic powder, Journal of Materials Processing Technology 213(4) (2013) 606-613.

S. Kou, Welding metallurgy, New Jersey, USA (2003) 431-446.

K.G. Prashanth, S. Scudino, H.J. Klauss, K.B. Surreddi, L. Löber, Z. Wang, A.K. Chaubey, U. Kühn, J. Eckert, Microstructure and mechanical properties of Al–12Si produced by selective laser melting: Effect of heat treatment, Materials Science and Engineering: A 590 (2014) 153-160.

M.A. Meyers, O. Vöhringer, V.A. Lubarda, The onset of twinning in metals: a constitutive description, Acta Materialia 49(19) (2001) 4025-4039.

O. Vöhringer, Einsatzspannung für die Bildung von Verformungszwillingen bei vielkristallinen α-Kupferlegierungen, Zeitschrift für Naturforschung A 24(3) (1969) 478-478.

R. Mulford, U. Kocks, New observations on the mechanisms of dynamic strain aging and of jerky flow, Acta Metallurgica 27(7) (1979) 1125-1134.
S. Asgari, E. El-Danaf, S.R. Kalidindi, R.D. Doherty, Strain hardening regimes and microstructural evolution during large strain compression of low stacking fault energy fcc alloys that form deformation twins, Metallurgical and Materials Transactions A 28(9) (1997) 1781-1795.
E. El-Danaf, S.R. Kalidindi, R.D. Doherty, Influence of grain size and stacking-fault energy on deformation twinning in fcc metals, Metallurgical and Materials Transactions A 30(5) (1999) 1223-1233.
M. Ojima, Y. Adachi, Y. Tomota, Y. Katada, Y. Kaneko, K. Kuroda, H. Saka, Weak beam TEM study on stacking fault energy of high nitrogen steels, steel research international 80(7) (2009) 477-481.

8 Appendices

8.1 Supplemental Materials of Chapter 3

001 load orientation

Schmid factors for 12 slip systems for FCC

Slip plane, p			Slip direction, d			Schmid factor
1	1	1	-1	1	0	0.000
1	1	1	-1	0	1	0.408
1	1	1	0	-1	1	0.408
1	1	-1	-1	1	0	0.000
1	1	-1	1	0	1	-0.408
1	1	-1	0	1	1	-0.408
1	-1	1	1	1	0	0.000
1	-1	1	-1	0	1	0.408
1	-1	1	0	1	1	0.408
-1	1	1	1	1	0	0.000
-1	1	1	1	0	1	0.408
-1	1	1	0	-1	1	0.408

Schmid factors for 12 slip systems for BCT (001 loading direction)

Slip plane, p			Slip direction, d			Schmid factor
0	1	0.707	1	-1	1.414	0.408
0	1	0.707	1	1	-1.414	-0.408
1	0	0.707	-1	1	1.414	0.408
1	0	0.707	1	1	-1.414	-0.408
1	1	0	-1	1	1.414	0.000
1	1	0	1	-1	1.414	0.000
0	-1	0.707	1	1	1.414	0.408
0	-1	0.707	-1	1	1.414	0.408
1	0	-0.707	1	1	1.414	-0.408
1	0	-0.707	1	-1	1.414	-0.408
-1	1	0	1	1	1.414	0.000
-1	1	0	1	1	-1.414	0.000

Schmid factors for twining systems in FCC (001 loading direction)

Slip plane, p			Slip direction, d			Schmid factor
1	1	1	1	1	-2	-0.471
1	1	-1	1	1	2	-0.471
1	-1	1	1	-1	-2	-0.471
-1	1	1	-1	1	2	0.471

Figure 8-1. Schmid factors of the slipping systems and twinning systems under [001] orientation loading.

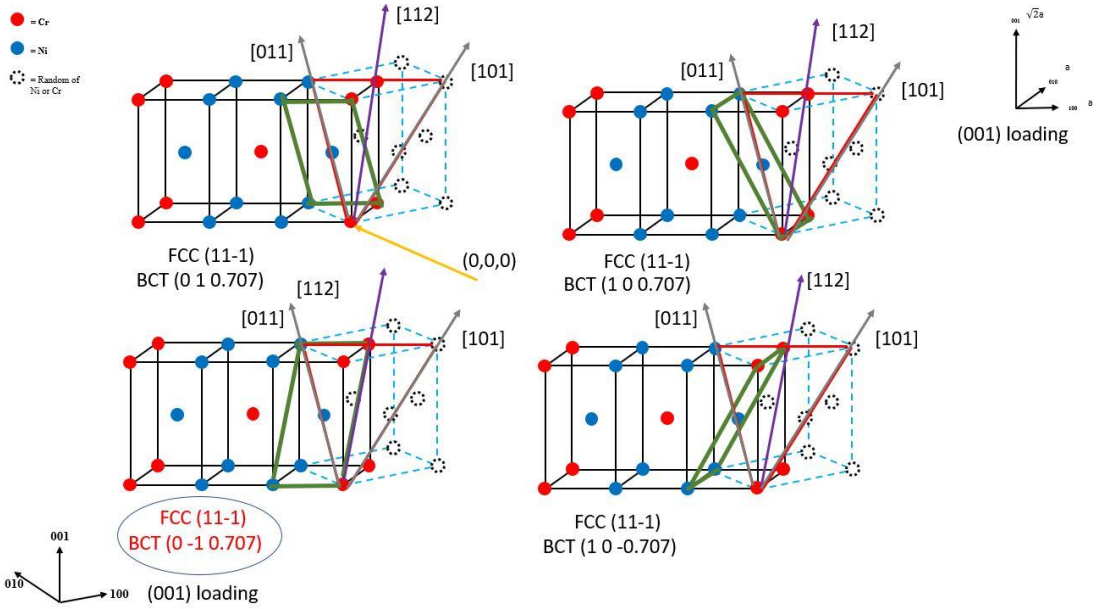
= Cr
= Ni
= Random of Ni or Cr
[112]
[011]
[101]
FCC (11-1)
BCT (0 1 0.707)
(0,0,0)
FCC (11-1)
BCT (1 0 0.707)
FCC (11-1)
BCT (0 -1 0.707)
FCC (11-1)
BCT (1 0 -0.707)
001
010
100
(001) loading

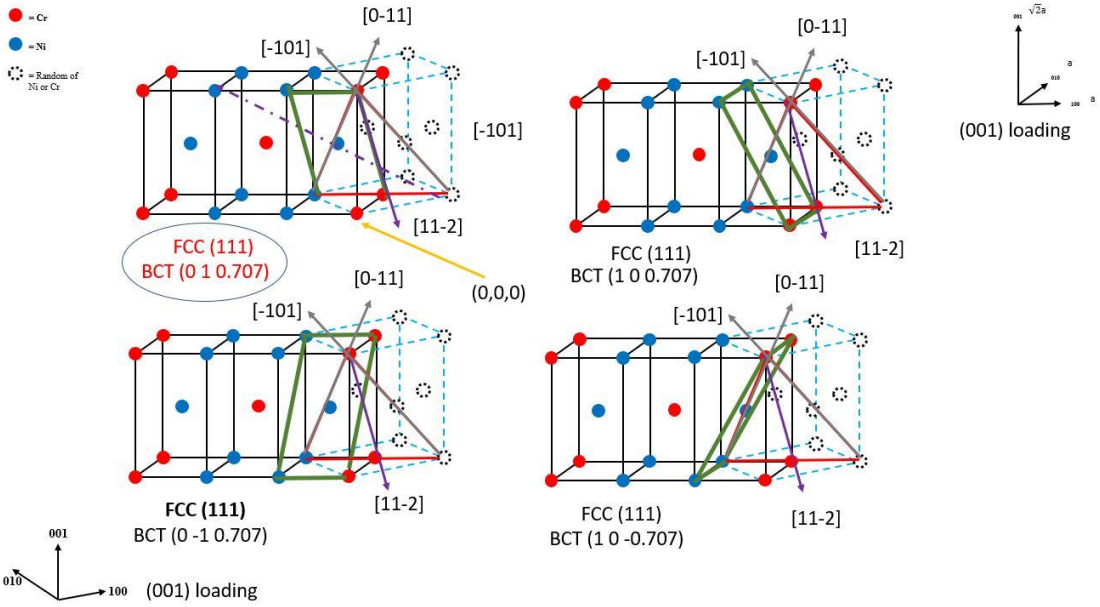
= Cr
= Ni
= Random of Ni or Cr
[0-11]
[-101]
[11-2]
FCC (111)
BCT (0 1 0.707)
(0,0,0)
FCC (111)
BCT (1 0 0.707)
FCC (111)
BCT (0 -1 0.707)
FCC (111)
BCT (1 0 -0.707)
001
010
100
(001) loading

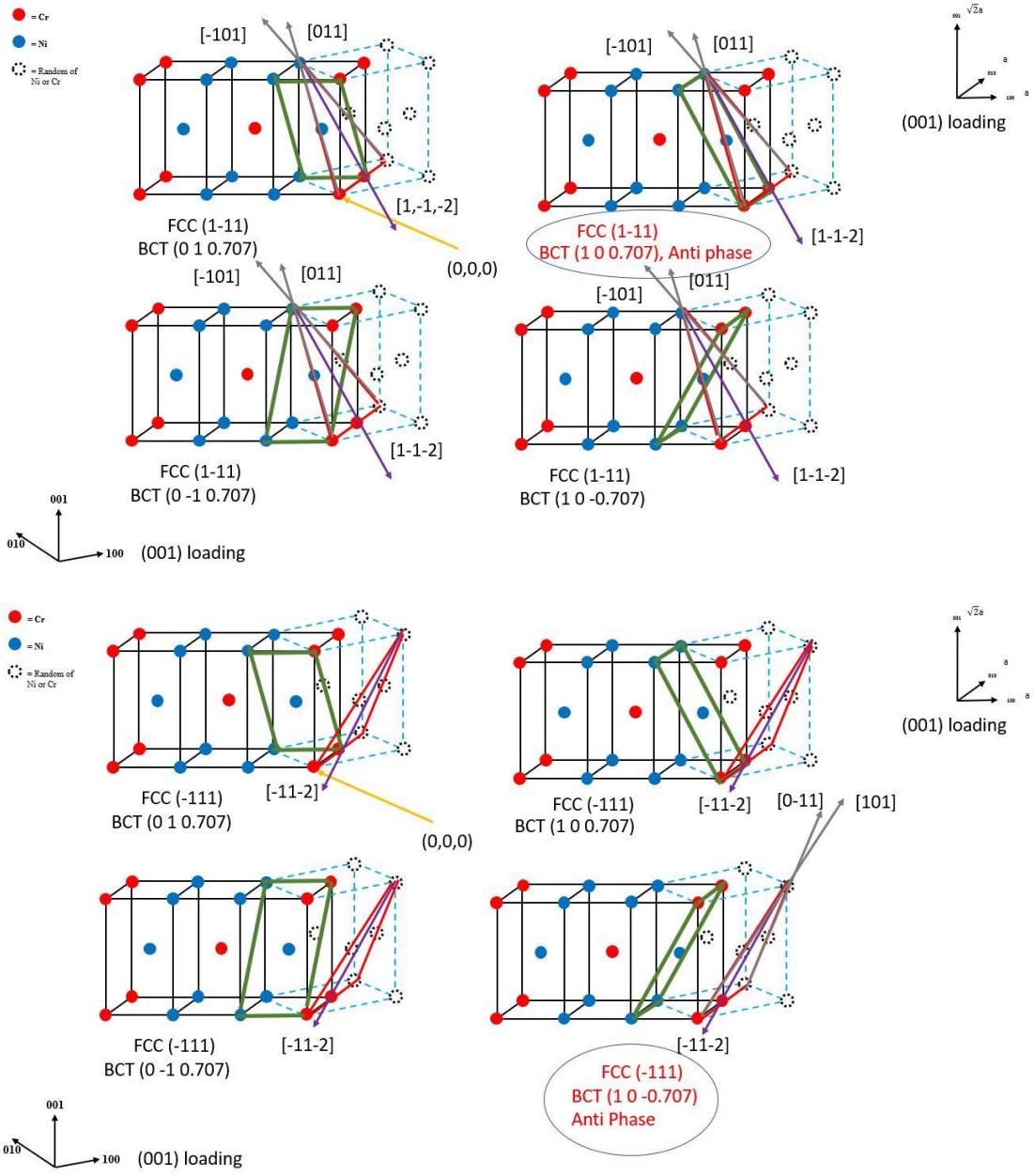

Figure 8-2. Sixteen combinations of fcc and bct slip systems and the corresponding twinning slipping direction of fcc under [001] loading orientation.

111 load orientation

Schmid factors for 12 slip systems for FCC (111 loading direction)

Slip plane, p			Slip direction, d			Schmid factor
1	1	1	-1	1	0	0.000
1	1	1	-1	0	1	0.000
1	1	1	0	-1	1	0.000
1	1	-1	-1	1	0	0.000
1	1	-1	1	0	1	0.272
1	1	-1	0	1	1	0.272
1	-1	1	1	1	0	0.272
1	-1	1	-1	0	1	0.000
1	-1	1	0	1	1	0.272
-1	1	1	1	1	0	0.272
-1	1	1	1	0	1	0.272
-1	1	1	0	-1	1	0.000

Schmid factors for 12 slip systems for BCT (111 loading direction)

Slip plane, p			Slip direction, d			Schmid factor
0	1	0.707	1	-1	1.414	0.329
0	1	0.707	1	1	-1.414	0.136
1	0	0.707	-1	1	1.414	0.329
1	0	0.707	1	1	-1.414	0.136
1	1	0	-1	1	1.414	0.333
1	1	0	1	-1	1.414	0.333
0	-1	0.707	1	1	1.414	-0.136
0	-1	0.707	-1	1	1.414	-0.056
1	0	-0.707	1	1	1.414	0.136
1	0	-0.707	1	-1	1.414	0.056
-1	1	0	1	1	1.414	0.000
-1	1	0	1	1	-1.414	0.000

Schmid factors for twining systems in FCC (111 loading direction)

Slip plane, p			Slip direction, d			Schmid factor
1	1	1	1	1	-2	0.000
1	1	-1	1	1	2	0.314
1	-1	1	1	-1	-2	-0.157
-1	1	1	-1	1	2	0.157

Figure 8-3. Schmid factors of the slipping systems and twinning systems under [111] orientation loading.

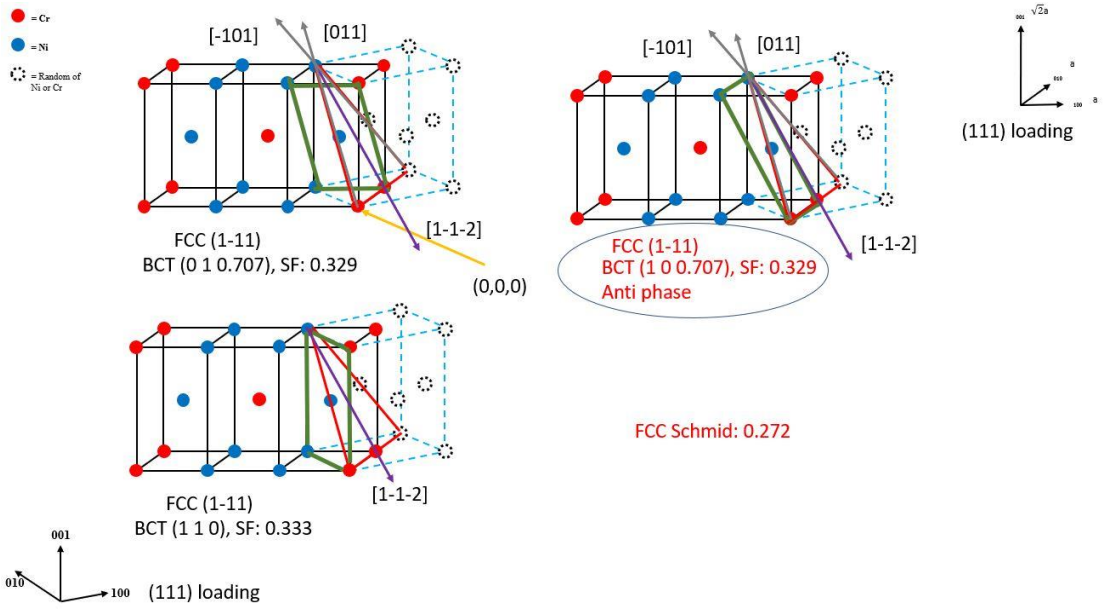
= Cr
= Ni
= Random of Ni or Cr
[-101]
[011]
[1-1-2]
FCC (1-11)
BCT (0 1 0.707), SF: 0.329
(0,0,0)
[-101]
[011]
[1-1-2]
FCC (1-11)
BCT (1 0 0.707), SF: 0.329
Anti phase
(111) loading
FCC Schmid: 0.272
[1-1-2]
FCC (1-11)
BCT (1 1 0), SF: 0.333
001
010
100
(111) loading

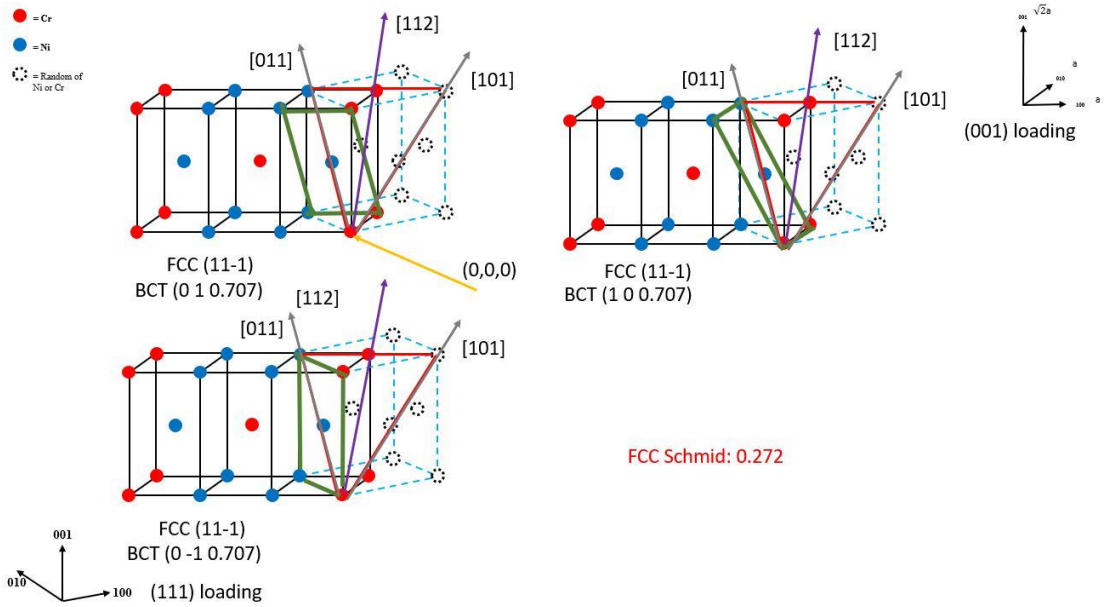
= Cr
= Ni
= Random of Ni or Cr
[112]
[011]
[101]
FCC (11-1)
BCT (0 1 0.707)
(0,0,0)
[112]
[011]
[101]
FCC (11-1)
BCT (1 0 0.707)
(001) loading
FCC Schmid: 0.272
[112]
[011]
[101]
FCC (11-1)
BCT (0 -1 0.707)
001
010
100
(111) loading

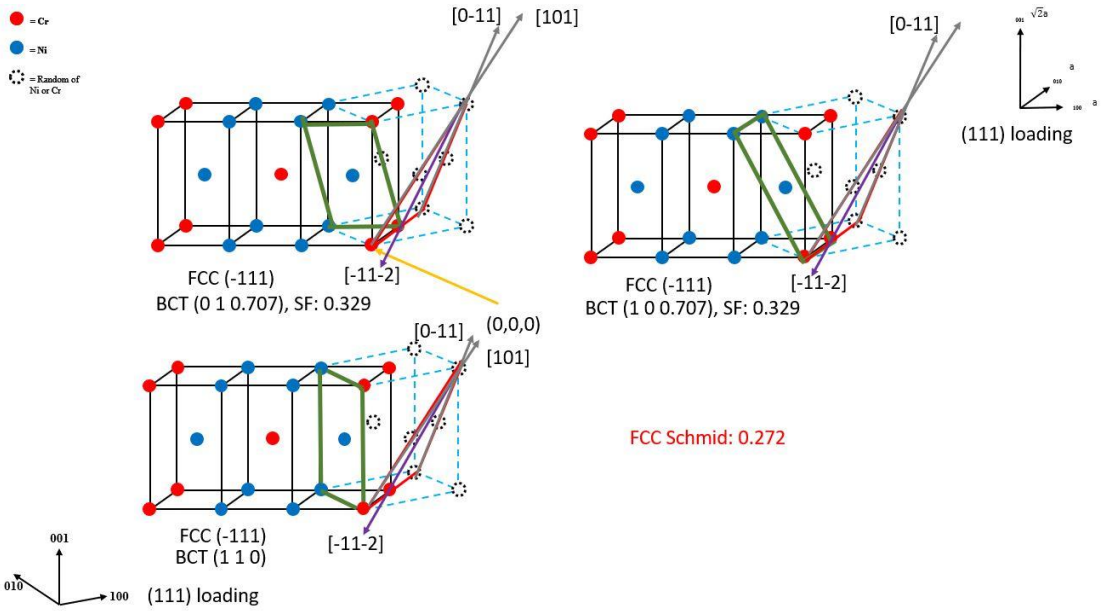

Figure 8-4. Nine combinations of fcc and bct slip systems and the corresponding twinning slipping direction of fcc under [111] loading orientation.

8.2 Supplemental Materials of Chapter 4

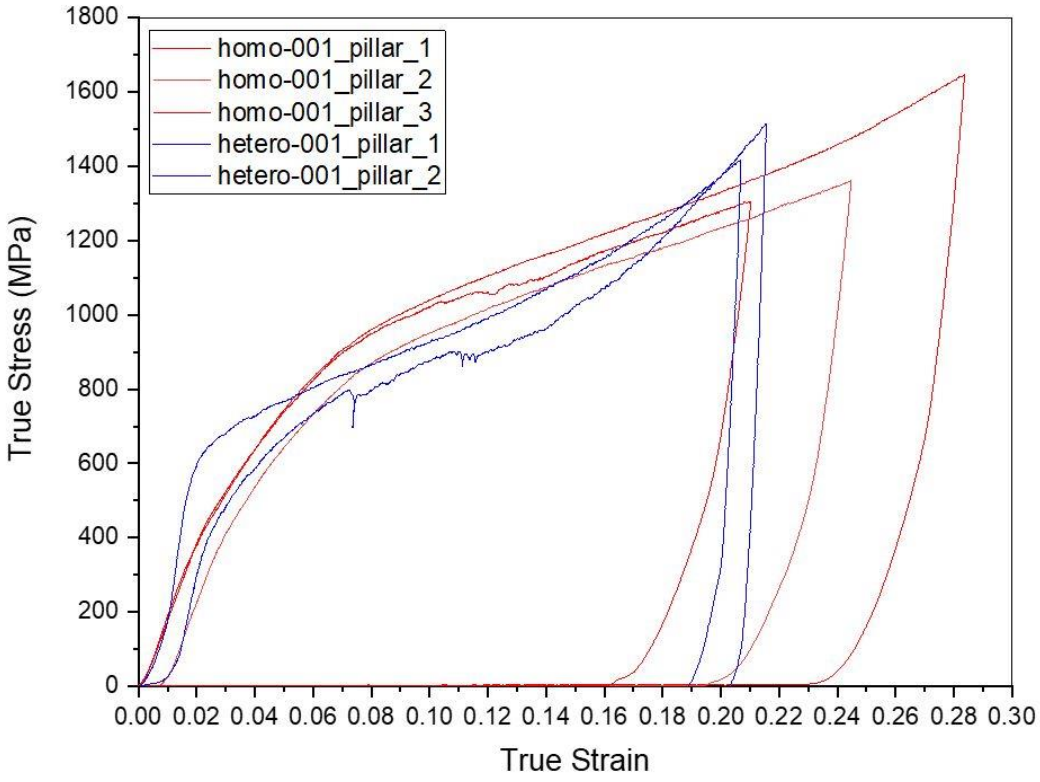

Figure 8-5. Stress-strain plots for all single-phase and dual-phase pillars.

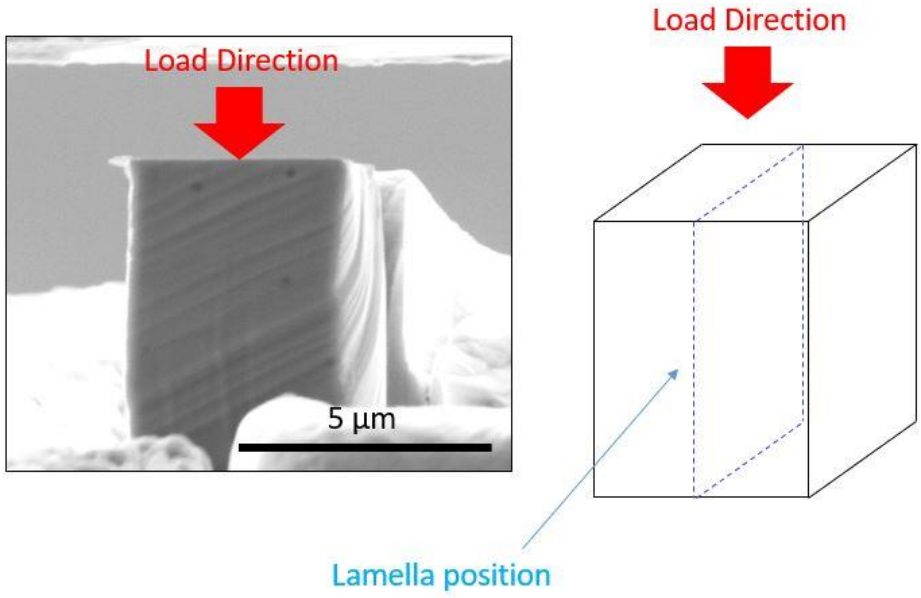

Figure 8-6. Pillar compression position and TEM lamella position.

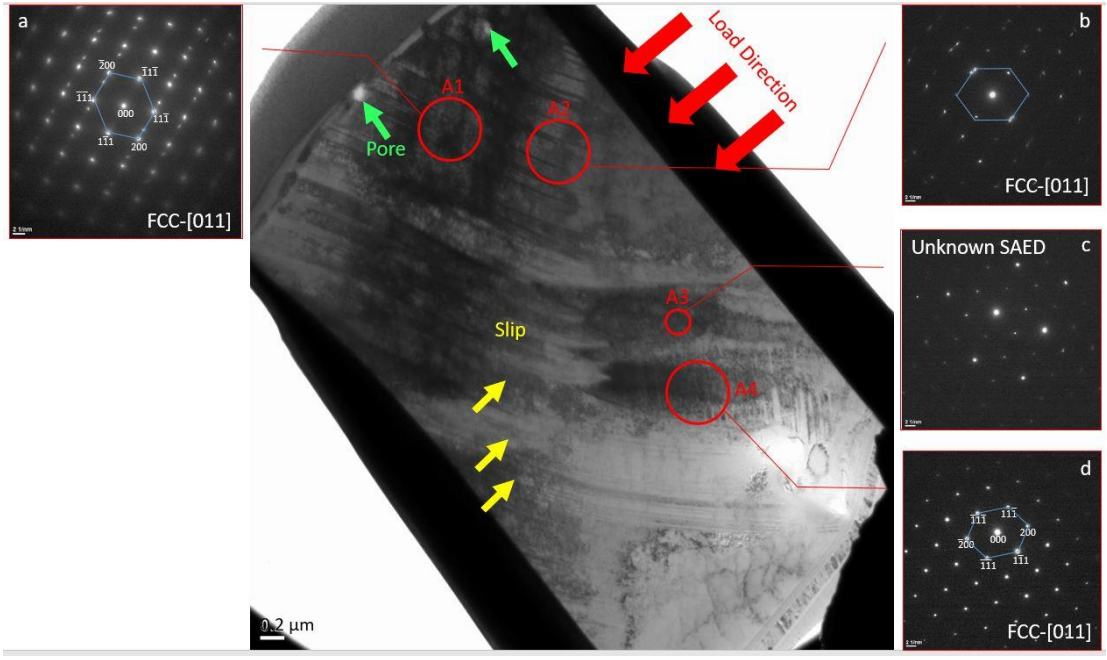

Figure 8-7. TEM characterization on compressed dual-phase pillar.

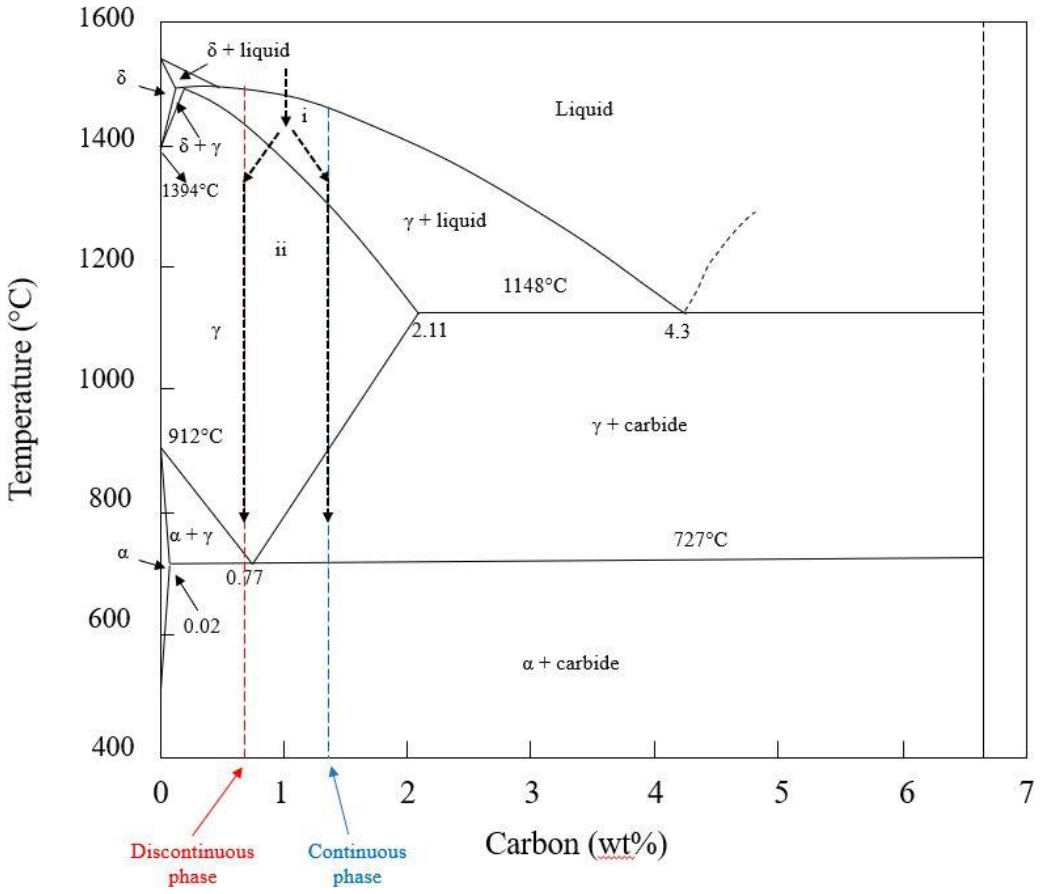

Figure 8-8. Fe-C phase diagram.

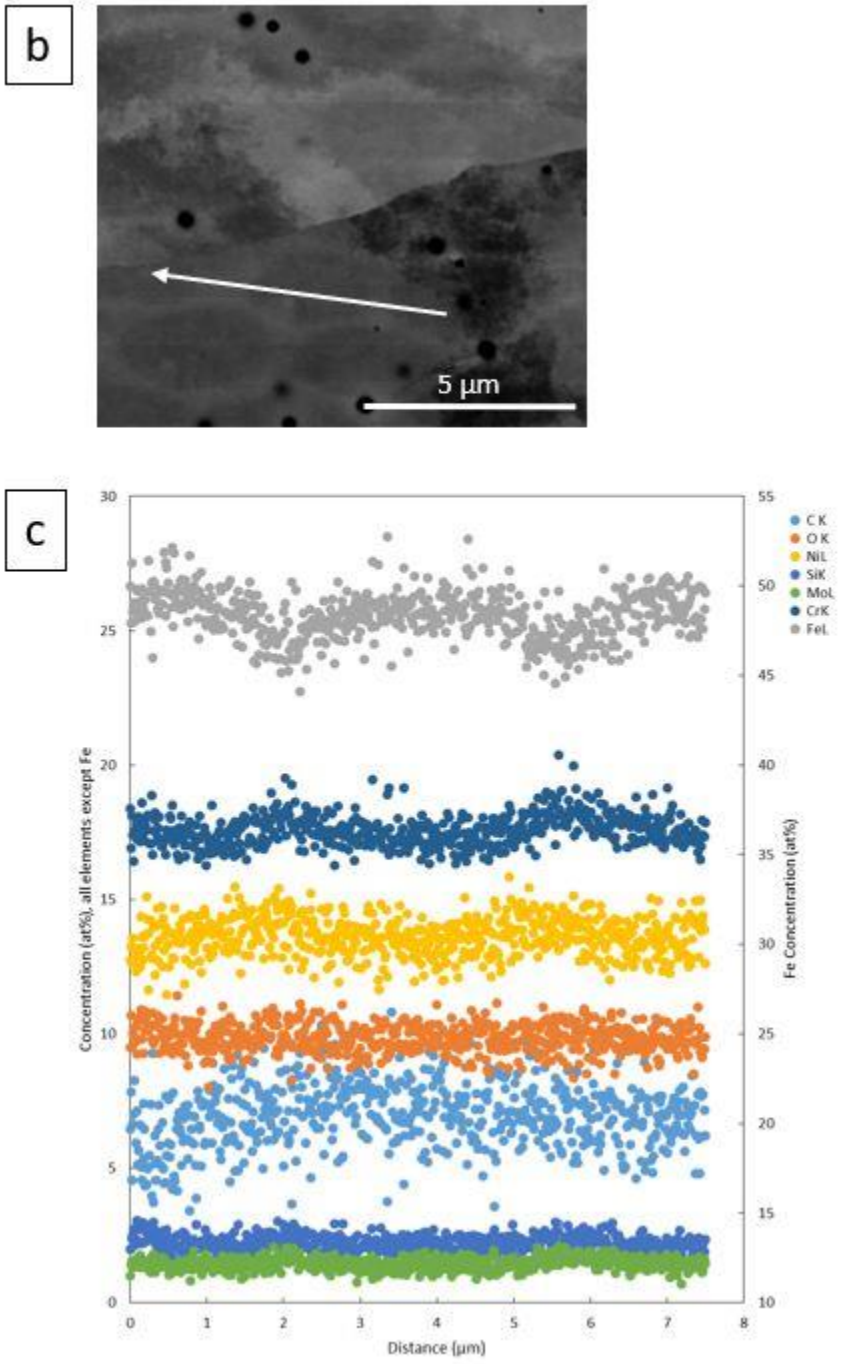

Figure 8-9. EDS line scanning across two boundaries of cellular sub-structure.

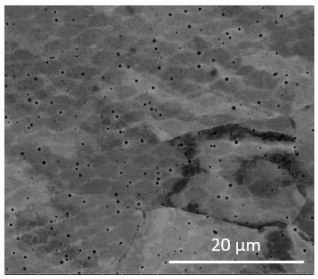

Area ID	Count	Average Size (µm²)	Porosity (%)
A1	315	0.012	0.418
A2	81	0.053	0.989
A3	46	0.083	1.257
A4	71	0.069	1.170
Average	128.25	0.0543	0.9585

Figure 8-10. Porosity calculation at four areas around sample surface.